Cellular reorganization in auxin-dependent pattern formation during early embryogenesis in *Arabidopsis thaliana*

Che-Yang
LIAO

Cellular reorganization in auxin-dependent pattern formation during early embryogenesis in *Arabidopsis thaliana*

Che-Yang Liao

Cellular reorganization in auxin-dependent pattern formation during early embryogenesis in *Arabidopsis thaliana*

Che-Yang Liao

Table of Contents

Chapter 1

INTRODUCTION
AND
SCOPE OF THE THESIS

Plant embryogenesis

Embryogenesis is the process among all land plants (the Embryophytes) in which a single celled zygote develops into a multicellular individual. In early diverging land plants, the end product of embryogenesis is the mature sporophyte that undergoes meiosis to form haploid spores, and as such there is limited diversity in embryo cell types[1]. In contrast, in vascular plants, which include the seed plants and flowering plants, the embryo undergoes a distinct pattern formation process, where, from a single cell, the precursors of the major tissues of the sporophyte are generated. In these embryos, the different cell types, tissues, and organs are all specified as embryogenesis progresses, and are all arranged in a distinct pattern[2].

Thus, embryogenesis in vascular plants is the window of plant life during which cell type specification, cell communication and morphogenesis generate the formation of new individuals in a limited time span. The ingredients of embryo morphogenesis include the establishment of different cell types with unique identities, reflected in gene expression patterns, and resulting differences in cell growth, shape, division and differentiation. Given that terminal differentiation does not occur during early flowering plant embryogenesis, this window of development offers a very good opportunity to dissect the control of cell type specification, growth and division.

The trajectory of embryogenesis, particularly the order of divisions and timing of pattern formation, differs among different species. Some species have intrinsically chaotic cell divisions[3], others first generate many cells and later establish an organ pattern[4, 5]. In contrast, embryogenesis in the dicotyledonous plant *Arabidopsis thaliana* is extremely regular[6]. In this model species within the crucifer family, cell divisions hardly differ between individuals, suggesting tight control of cell division rate and planes directly after fertilization. While this regularity in division is by no means common to land plants, and may in fact be a consequence of the speed and limited number of cells used during embryogenesis, the near-invariance offers tremendous potential for studying the regulation of cell division pattern and orientation in a multicellular context.

Arabidopsis embryogenesis has been studied for several decades, and anatomic and genetic studies have helped derive the key steps in early embryogenesis (Fig. 1). Following zygote elongation, the cell divides asymmetrically. This asymmetric cell division results in a smaller apical cell and a larger basal cell. The apical cell is the precursor of all cells in the embryo proper, and it first undergoes three rounds of symmetric divisions. The first two rounds are radial anticlinal, and are followed by a transverse anticlinal cell division. This series of symmetric cell division gives rise to an isodiametric 8-celled embryo proper consisting of four cells in the upper tier and another four in the lower tier. Since the cells in each tier express different genes[7], this stage also marks the establishment of an apical-basal axis in the embryo proper[8]. The upper tier
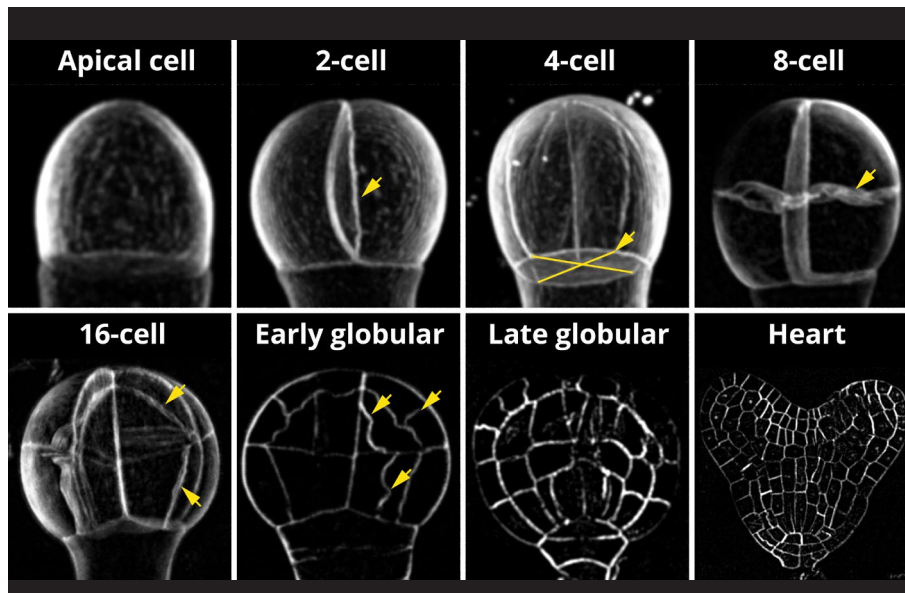
Figure 1. Cellular pattern of *Arabidopsis* early embryo.
Cellular profile and cell division pattern of *Arabidopsis* embryo from the formation of the apical cell to the heart stage. Arrows indicate the new cell walls formed from the previous cell division resulting to the corresponding developmental stages.

cells will later develop into the cotyledons and shoot apical meristem[6]. The lower tiers cells generate the hypocotyl and the root[6]. At the 8-cell stage, cells in both tiers divide asymmetric and periclinally to generate two cell layers. The inner layer represents the vascular-ground-tissue precursor, while the outer layer forms the protoderm, the precursor of the epidermis. This separation of inner and outer cell layers also visually marks the establishment of the radial axis in the embryo proper[9, 10]. The embryo proper enters the early globular stage after the vascular-ground-tissue ancestor cells divide periclinally. This periclinal cell division separates precursors of vascular and ground tissue and completes the establishment of all three fundamental tissue layers of flowering plants. This pattern of concentric tissue layers, laid down after only 6 rounds of cell division in the embryo proper, is then maintained throughout plant development in all post-embryonic organs[6, 9-11]. Unlike the apical zygote daughter cell, the basal daughter cell and its descendants divide only transversely and develop into the suspensor. The suspensor serves as the sole physical connection between the embryo and the maternal tissue in the seed. Only the top-most suspensor cell, the hypophysis, is incor-

porated into the embryo at early globular stage. At the end of the early globular stage, the hypophysis cell undergoes an asymmetric cell division forming a small lens-shaped cell and a larger lower cell that will develop into the quiescent center and the root cap in the root, respectively[9, 10]. This dynamic but strictly regulated series of cell division makes embryogenesis an ideal model system to address the fundamental question in developmental biology of how ordered cellular patterns are established from a single cell. In particular, open questions are what cellular events are required to execute oriented division, and what regulatory mechanisms control these events.

Regulation of embryo pattern formation

As described above, patterning of the *Arabidopsis* embryo in tissue layers and functional units (root, shoot) occurs within a few rounds of cell division. These divisions seem tightly controlled, which suggests robust regulatory mechanisms. Importantly, because there is little variation among individuals, there is likely a genetic basis for the regulation of pattern formation, and an important goal is to identify regulators and understand the mechanisms through which these direct cell identity and division orientation. Conceptually, identity and morphogenesis of individual cells could be cell-autonomously defined (e.g. by distinct levels of regulatory factors), or may be instructed non-cell-autonomously (e.g. by mobile signals) [12]. From genetic analysis in *Arabidopsis* early embryogenesis, two main pathways have emerged, and were linked to the establishment of the body axes. The first pathway defines the apical-basal axis from the earliest stages onwards, and even appears to act in the zygote. This pathway involves a subgroup of WUSCHEL-related homeobox transcription factors (WOXs), namely WOX2, WOX8, and WOX9, and the WRKY DNA-binding protein 2 (WRKY2)[8, 13]. Mutations in any of the components of this pathway, as well as the genetically interacting YODA/MAPK/SSP pathway[14-16], interfere with zygote elongation, suspensor development, and with normal divisions in the embryo proper at pre-globular stages[8, 13-16]. While cellular targets are unknown, this signaling system appears to be critical for early apical-basal axis formation, another pathway to establish body axes involves directional auxin transport, and the subsequent transcriptional response to this hormone through the nuclear auxin-signaling pathway[9, 17, 18]. Auxin is crucial for early embryogenesis as the mutations with impairments in auxin transport or signaling result in altered cell division orientation in the apical cell[9, 17-19], failure in root establishment[9, 17, 18, 20-22], and cotyledon specification and development[9, 17, 18, 22-25].

Auxin in the form of indole-3-acetic acid (IAA) is only synthesized by specific cells, and is unable to exit the cell via passive diffusion. Thus, to reach target cells, it requires auxin efflux carriers to be exported from the cell for its local transport (reviewed by [26]). Directional transport of IAA has long been known to occur (reviewed by [27]), and in-

deed, the efflux facilitators of the PIN-FORMED (PIN) family are polar localized in plant cells, allowing for polar auxin transport[19, 28-33]. In the mildly acidic apoplast environment, only a minor portion of the auxin is protonated and can easily enter cells[34]. Hence, auxin influx carriers facilitate the major auxin influx into cells[35-37]. In contrast to the PIN proteins, the AUX1/LAX influx carriers are evenly distributed over the membrane, and likely facilitate uniform influx of polar transported auxin. Given the prominent role of biosynthesis, efflux and influx in auxin accumulation, the local auxin distribution and auxin maxima can be deduced via the expression domain of auxin biosynthesis genes and the polar localization of auxin efflux carriers and validated via auxin immunolocalization[19, 29, 30, 33]. Based on these observations, it has been deduced that auxin is transported from the maternal tissue through the suspensor to embryo proper where no auxin biosynthesis occurs until the globular stage[19, 29, 33]. The auxin maxima remain in the embryo proper until early globular stage when the localization of auxin efflux carriers in the vasculature and ground tissue precursors shifts and reverses the direction of auxin transport followed by changing the auxin maxima from the embryo proper to the hypophysis cell[19, 29]. From the globular stage onward, auxin biosynthesis is initiated at the upper epidermal cells, which will develop into the cotyledon primordia, and transport auxin toward the hypophysis via the vascular cells[19, 21, 22, 29]. These predicted auxin accumulation sites match the developmental processes well that are disrupted when auxin biosynthesis[21-23, 38], transport[19, 20, 29, 39] or response (see below) are impaired.

Transcriptional auxin signaling occurs in the nucleus and encompasses two steps (Fig. 2). The first entails auxin perception via auxin-induced degradation of Aux/IAA proteins, a family of transcriptional inhibitors[40-42]. The second step involves the modulation of auxin-responsive genes by DNA-bound ARF transcription factors[43]. Auxin perception is mediated by binding to a pocket in the auxin receptors: TIR1/AFB F-box proteins that are part of SKP1–CUL1–F-BOX (SCF) ubiquitin ligase complexes[44, 45]. In turn, auxin facilitates the binding between SCF (TIR1/AFBs) and their substrates, the Aux/IAA inhibitor proteins[46, 47]. This leads to the ubiquitination and degradation of Aux/IAAs. Aux/IAAs bind with and inhibit the DNA-bound ARFs[44, 45, 48], and Aux/IAA degradation relieves the inhibition of these transcription factors. ARFs recognize auxin response elements (*AuxREs*) in their target genes, and activate or suppress these target genes, thus leading to auxin responses[43, 49-51].

Among the genes activated by the ARFs are those that are required for the local developmental outcome of auxin response. There are specific Aux/IAA and ARF proteins that mediate the activity of auxin in regulating embryo development. Loss of function mutations in the ARF5/MONOPTEROS (MP) gene, or mutations in IAA12/BODENLOS that prevent auxin-dependent degradation[52] both cause the lack of a root[9, 17], a phe-

notype shared with mutants in auxin biosynthesis[21, 22] , transport[19, 20] or perception[24]. Targets of MP have been identified, and these include genes such as TMO5 and TMO7 that control aspects of embryonic root and tissue formation[53]. Although the identification of mechanisms for auxin synthesis, transport and response in the embryo, as well as some of its transcriptional targets, has been very helpful, a key open question is how auxin acts. How does accumulation qualitatively and quantitatively relate to response? Is action always cell-autonomous? Visualization of the hormone and its response is critical to address these questions.

While distribution of the small auxin molecule cannot (yet) directly be visualized, auxin response maxima can be visualized via reporter genes. When driven by promoters of endogenous auxin response genes, or by synthetic auxin response reporters consisting tandem arranged *AuxREs*, reporter genes mark sites that are consistent with prediction based on the expression domain of auxin biosynthesis genes and polar localization of auxin efflux carriers[49, 54-60]. Such reporters have been very useful in determining where and when auxin accumulates, but it has so far been very difficult to visualize auxin responses in the early embryo at high resolution, owing to the design of available auxin response reporters. Therefore, re-design and optimization of these tools are likely required to determine sites of embryonic auxin response, as an important step in understanding the mechanisms underlying auxin-dependent pattern formation.

Cellular basis of morphogenesis
Morphogenesis in plants – where cells are immobile - is based on controlled cell expansion and oriented cell division, and embryogenesis is a good model system to understand its regulation. Defects in auxin response lead to alterations in cell division planes (Fig 3). Thus, auxin response is correlated with cell division planes, and it is possible that auxin controls division orientation. An important question therefore is whether division plane orientation in the embryo involves anisotropic cell expansion or is determined without cell growth. Detailed 3D analysis of embryo development, followed by cell segmentation and quantitative analysis showed that the volume of the embryo proper only increase slightly during the first rounds of division[61]. As a consequence, 8-and 16-cell embryos are only two and four times the size of the apical cell[61]. Besides the minor increased embryo volume at the early developmental stages, the shape of the embryo proper remains isodiametric from the apical cell until the late globular stage. This suggests that the embryo proper undergoes only isotropic cell expansion, and thus oriented cell division appears to be the sole input of morphogenesis at this stage.

Most analysis of cell division orientation control in plants has been done in the context of symmetric divisions, and until recently, only in 2D. During symmetric cell divi-
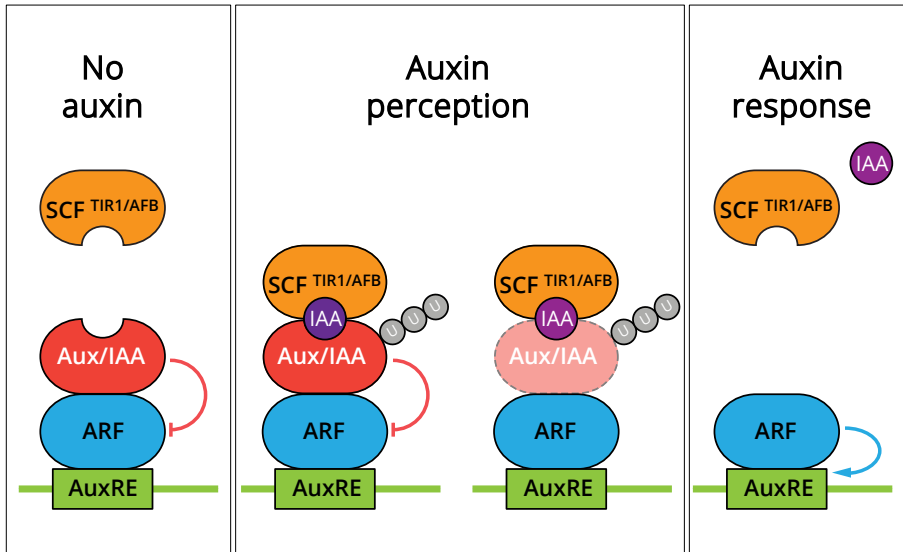
Figure 2. Transcriptional auxin signaling pathway.

With no auxin (IAA), ARF activity is suppressed by AUX/IAA to regulate the auxin responsive genes whose regulatory elements contain AuxRE. Auxin is perceived by SCF (TIR1/AFB) protein complex through affiliating the binding between SCF (TIR1/AFB) protein complex and Aux/IAA followed by the ubiquitination and degradation of Aux/IAA. With the degradation of Aux/IAA and the removal of its inhibition, ARF then regulates the transcriptional activity of the auxin responsive genes leading to auxin response.

sion, the determination of division plane orientation follows a rule based on the geometric property of the mother cell. Within this geometry, several possible cell division planes that represent global or local minimal cell wall area compete, each giving rise to equal volumes of the daughter cells[62]. The likely components used by the cell to perceive its own geometric properties are the nucleus and the cytoplasmic microtubules radiating form the surface of the nucleus to the plasma membrane[63]. Prior to mitosis, the nucleus is positioned in the center of the cell and serves as the reference for the cytoplasmic microtubules, whose tension upon the formation of the preprophase band determines the position of the preprophase band[63]. The preprophase band will then be positioned that it bisects the nucleus with the most stable cytoplasmic microtubule and minimal surface area of the new cell wall[64]. Displacement of the nucleus away from the geometric center of the cell, or alteration of microtubule stability that prohibit the formation of the preprophase band, leads to altered division plane orientation[65-70]. Once
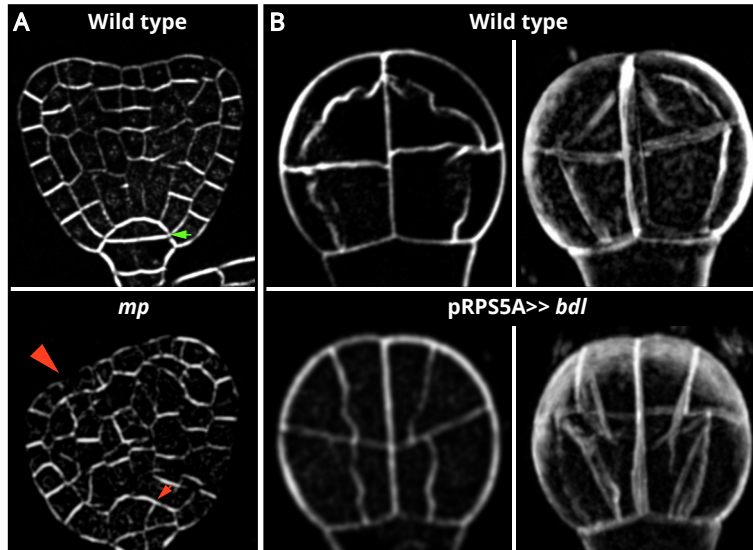
Figure 3. Altered cellular pattern in auxin response mutants.
(a) Altered cell division orientation in wild type (WT) and *arf5/mp* (mp) loss of function mutant embryo with defect in hypophysis division (arrow) and cotyledon development (arrowhead). (b) Cell division orientations in wild type embryo (WT) and embryo with induced auxin response suppression via ectopically expressing auxin-insensitive *iaa12/bdl* driven by RPS5A promoter (pRPS5A>> bdl).

the division plane is determined, the orientation and position of mitosis only follows the preprophase band. Displacement of the spindle has no effect on the position of the cortical division site and following formation of cell plates in the cytokinesis[71]. Thus, division orientation is determined pre-mitotically, and involves cell geometry, microtubules, and nucleus position.

In asymmetric cell divisions, where the mother cell is not divided in two equal cells, the position and orientation of the cell division plane is tightly controlled to deviate from symmetric division[72]. An axis of polarity must be established within the mother cell as the reference of the mitotic and cytokinetic machineries, guiding the division plane[73, 74]. In developing stomata of *Arabidopsis*, receptor-like proteins for directing the polarity and a plant specific protein, BASL, are key regulators for the asymmetric division of the meristemoid mother cell and meristemoid[75]. BASL is localized in the nucleus

and the plasma membrane at the opposite side to where the asymmetric cell division occurs in the meristemoid mother cell[75]. Unlike symmetric cell division, the position of the cell division plane is neither determined by the position of the centrally localized nucleus nor the geometric property of the cell[76]. Instead, actin controls the migration of the nucleus to the future cell division plane and the subsequent positioning of the preprophase band[77-79]. Beyond this relatively well-established example in the stomatal lineage, little is known about the regulators and triggers of polarity and oriented cell division. Given that BASL is not expressed in the embryo[75], a different mechanism must account for the auxin-dependent control on division orientation in the embryo.

Oriented cell division during embryogenesis

Defects in cell division orientation and position during early embryogenesis, for example, the anticlinal division of the apical cell, the periclinal division in vasculature precursor cell and asymmetric hypophysis division, had been widely reported among mutants with mutation in key regulatory components in auxin responses[9, 17]. While there was no context for understanding how and why these divisions were altered, three-dimensional analysis of division planes has helped to develop a framework. Computational analysis of 3D cell volumes revealed that the principles for geometric determination of division plane could account for the divisions from 1-cell to 8-cell stage[61]. These divisions therefore do not seem to require regulation. In contrast, the asymmetric divisions at the 8-cell stage, giving rise to outer and inner cell layers, are far from consistent with a rule that dictates the minimal surface area going through the cell center. Thus, these divisions appear to deviate from the default. Previously, it had been found that ubiquitous expression of mutant bdl protein – globally inhibiting ARF activity and auxin response – caused abnormal divisions at the 8-cell to 16-cell transition[61]. Analysis of cell divisions in 3D and computational analysis revealed that in these embryos, all cells divided according to the default dictated by cell geometry. Thus, auxin response allows cells to deviate from the default division plane given by cell geometry[61]. The same was found to be true for the auxin-dependent hypophysis division, suggesting that this mode of action may represent a more general auxin output in embryo cells. While this discovery pinpointed a role for auxin response in controlling oriented cell division through inhibiting default division, the cellular machinery and mechanism of auxin-response-dependent pattern formation remain to be determined.

Scope of this thesis

Following from the finding that auxin controls embryo development and regulates cell division orientation in the embryo, the research described in this thesis asks the question where and how the hormone acts to bring about these responses.

A major limitation in understanding auxin action at cellular level in the embryo was the lack of appropriate tools to visualize hormone accumulation and response. In Chapter 2, two novel fluorescent protein-based reporters for auxin perception and responses were established. These offer superb sensitivity and responsiveness *in vivo* with cellular resolution and help revealing maxima of auxin perception and response that were previously undetectable. Not only do these tools help to detect sites of auxin action in the embryo, the design also allows deployment in other stages of plant development. Thus, I describe a generic set of tools for auxin biology. Following the development of new tools for auxin perception *or* response, in Chapter 3, I describe and characterize the first comprehensive auxin reporter that allows visualization of both auxin perception *and* response simultaneously in the same cells. Using this powerful tool, I demonstrate differential auxin signaling capacity in different cell types and developmental stages. In addition, I use a novel auxin response reporter to visualize auxin output in mutant embryos with defected local auxin response.

The control of cell division orientation during embryo development must involve reorganization of cytoskeleton, membranes or organelles. However, it was impossible to visualize these structures in *Arabidopsis* embryos. In Chapter 4, a toolkit is developed and characterized that allows the specific visualization of a range of subcellular structures using fluorescent markers. By optimizing markers and imaging approaches, we achieved 3-dimentional imaging of cellular structures during early embryogenesis. Using these tools, we mapped topologies of organelles and cytoskeleton, revealing interesting structures and organization. Furthermore, using these tools, we reveal an unexpectedly early establishment of inner/outer cell polarity in the early embryo. In Chapter 5, we applied part of the toolkit developed in the previous chapter to embryos with controlled inhibition of auxin responses to determine the effect of auxin response on actin and microtubule cytoskeleton organization at early embryogenesis. We find that there are distinct effects of auxin response on both cytoskeletons, thus paving the way for future studies focused on the biochemical mechanisms of regulation.

Finally, in Chapter 6, I place the findings of this thesis in a broader context, discuss the emerging insights and plot ways forward.

References

1. Niklas, K.J. & Kutschera, U. *New Phytol.* **185**, 27-41 (2010).
2. Johri, B.M., Ambegaokar, K.B. & Srivastava, P.S. Comparative embryology of angiosperms. (Springer-Verlag, 1992).
3. Pollock, E.G. & Jensen, W.A. *Am. J. Bot.* **51**, 915-& (1964).
4. Poethig, R.S., Coe, E.H. & Johri, M.M. *Dev. Biol.* **117**, 392-404 (1986).
5. Itoh, J. et al. *Plant Cell Physiol.* **46**, 23-47 (2005).
6. Mansfield, S.G. & Briarty, L.G. *Canadian Journal of Botany* **69**, 461-476 (1991).
7. Lau, S., Slane, D., Herud, O., Kong, J. & Jurgens, G. *Annu. Rev. Plant Biol.* **63**, 483-506 (2012).
8. Breuninger, H., Rikirsch, E., Hermann, M., Ueda, M. & Laux, T. *Dev. Cell* **14**, 867-876 (2008).
9. Hamann, T., Mayer, U. & Jurgens, G. *Development* **126**, 1387-1395 (1999).
10. Scheres, B. et al. *Development* **120**, 2475-2487 (1994).
11. Barton, M.K. & Poethig, R.S. *Development* **119**, 823-831 (1993).
12. Palovaara, J., De Zeeuw, T. & Weijers, D. in Annual Review of Cell and Developmental Biology, Vol. 32 47-75 (2016).
13. Haecker, A. et al. *Development* **131**, 657-668 (2004).
14. Bayer, M. et al. *Science* **323**, 1485-1488 (2009).
15. Lukowitz, W., Roeder, A., Parmenter, D. & Somerville, C. *Cell* **116**, 109-119 (2004).
16. Wang, H., Ngwenyama, N., Liu, Y., Walker, J.C. & Zhang, S. *Plant Cell* **19**, 63-73 (2007).
17. Berleth, T. & Jurgens, G. *Development* **118**, 575-587 (1993).
18. Hamann, T., Benkova, E., Baurle, I., Kientz, M. & Jurgens, G. *Genes Dev.* **16**, 1610-1615 (2002).
19. Friml, J. et al. *Nature* **426**, 147-153 (2003).
20. Robert, H.S. et al. *Development* **142**, 702-711 (2015).
21. Robert, H.S. et al. *Curr. Biol.* **23**, 2506-2512 (2013).
22. Cheng, Y., Dai, X. & Zhao, Y. *Plant Cell* **19**, 2430-2439 (2007).
23. Stepanova, A.N. et al. *Cell* **133**, 177-191 (2008).
24. Dharmasiri, N. et al. *Dev. Cell* **9**, 109-119 (2005).
25. Ploense, S.E., Wu, M.F., Nagpal, P. & Reed, J.W. *Development* **136**, 1509-1517 (2009).
26. van Berkel, K., de Boer, R.J., Scheres, B. & ten Tusscher, K. *Development* **140**, 2253-2268 (2013).
27. Goldsmith, M.H.M. *Annual Review of Plant Physiology* **28**, 439-478 (1977).
28. Galweiler, L. et al. *Science* **282**, 2226-2230 (1998).
29. Friml, J. et al. *Cell* **108**, 661-673 (2002).
30. Friml, J., Wisniewska, J., Benkova, E., Mendgen, K. & Palme, K. *Nature* **415**, 806-809 (2002).
31. Petrasek, J. et al. *Science* **312**, 914-918 (2006).
32. Muller, A. et al. *EMBO J.* **17**, 6903-6911 (1998).
33. Benkova, E. et al. *Cell* **115**, 591-602 (2003).
34. Raven, J.A. *New Phytol.* **74**, 163-172 (1975).
35. Bennett, M.J. et al. *Science* **273**, 948-950 (1996).

36. Swarup, K. et al. *Nat. Cell Biol.* **10**, 946-954 (2008).
37. Swarup, R. et al. *Genes Dev.* **15**, 2648-2653 (2001).
38. Robert, H.S., Crhak Khaitova, L., Mroue, S. & Benkova, E. *J. Exp. Bot.* **66**, 5029-5042 (2015).
39. Weijers, D. et al. *Plant Cell* **17**, 2517-2526 (2005).
40. Gray, W.M., Kepinski, S., Rouse, D., Leyser, O. & Estelle, M. *Nature* **414**, 271-276 (2001).
41. Zenser, N., Ellsmore, A., Leasure, C. & Callis, J. *Proc Natl Acad Sci U S A* **98**, 11795-11800 (2001).
42. Tiwari, S.B., Hagen, G. & Guilfoyle, T.J. *Plant Cell* **16**, 533-543 (2004).
43. Ulmasov, T., Hagen, G. & Guilfoyle, T.J. *Science* **276**, 1865-1868 (1997).
44. Dharmasiri, N., Dharmasiri, S. & Estelle, M. *Nature* **435**, 441-445 (2005).
45. Kepinski, S. & Leyser, O. *Nature* **435**, 446-451 (2005).
46. Kepinski, S. & Leyser, O. *Proc Natl Acad Sci U S A* **101**, 12381-12386 (2004).
47. Yang, X. et al. *Plant J.* **40**, 772-782 (2004).
48. Tan, X. et al. *Nature* **446**, 640-645 (2007).
49. Ulmasov, T., Liu, Z.-B., Hagen, G. & Guilfoyle, T.J. *Plant Cell* **7**, 1611-1623 (1995).
50. Ulmasov, T., Hagen, G. & Guilfoyle, T.J. *Proc Natl Acad Sci U S A* **96**, 5844-5849 (1999).
51. Tiwari, S.B., Hagen, G. & Guilfoyle, T. *Plant Cell* **15**, 533-543 (2003).
52. Weijers, D. et al. *Dev. Cell* **10**, 265-270 (2006).
53. Schlereth, A. et al. *Nature* **464**, 913-916 (2010).
54. Ulmasov, T., Murfett, J., Hagen, G. & Guilfoyle, T.J. *Plant Cell* **9**, 1963-1971 (1997).
55. Sabatini, S. et al. *Cell* **99**, 463-472 (1999).
56. Yi, L., Wu, Y.H., Hagen, G. & Guilfoyle, T. *Plant and Cell Physiology* **40**, 675-682 (1999).
57. Bierfreund, N.M., Reski, R. & Decker, E.L. *Plant Cell Rep.* **21**, 1143-1152 (2003).
58. Mattsson, J., Ckurshumova, W. & Berleth, T. *Plant Physiol.* **131**, 1327-1339 (2003).
59. Pacios-Bras, C. et al. *Plant Mol. Biol.* **52**, 1169-1180 (2003).
60. Sakakibara, K. et al. *Development* **130**, 4835-4846 (2003).
61. Yoshida, S. et al. *Dev. Cell* **29**, 75-87 (2014).
62. Besson, S. & Dumais, J. *Proc Natl Acad Sci U S A* **108**, 6294-6299 (2011).
63. Lloyd, C.W. *Development* **113**, 55-65 (1991).
64. Wright, A.J. & Smith, L.G. in Plant Cell Monographs, Vol. 9 33-57 (2007).
65. Murata, T. & Wada, M. *Planta* **183**, 391-398 (1991).
66. Azimzadeh, J. et al. *Plant Cell* **20**, 2146-2159 (2008).
67. Camilleri, C. et al. *Plant Cell* **14**, 833-845 (2002).
68. Kawamura, E. et al. *Plant Physiol.* **140**, 102-114 (2006).
69. Spinner, L. et al. *Nature Communications* **4** (2013).
70. Vanstraelen, M. et al. *Curr. Biol.* **16**, 308-314 (2006).
71. Gunning, B.E. & Wick, S.M. *Journal of cell science. Supplement* **2**, 157-179 (1985).
72. De Smet, I. & Beeckman, T. *Nature Reviews Molecular Cell Biology* **12**, 177-188 (2011).
73. Shao, W. & Dong, J. *Dev. Biol.* **419**, 121-131 (2016).

74. Yang, Z. & Lavagi, I. *Curr. Opin. Plant Biol.* **15**, 601-607 (2012).
75. Dong, J., MacAlister, C.A. & Bergmann, D.C. *Cell* **137**, 1320-1330 (2009).
76. Galatis, B., Apostolakos, P. & Katsaros, C. *Protoplasma* **122**, 11-26 (1984).
77. Kennard, J.L. & Cleary, A.L. *Cell Motil. Cytoskeleton* **36**, 55-67 (1997).
78. Panteris, E., Apostolakos, P. & Galatis, B. *Cell Motility* **63**, 696-709 (2006).
79. MINEYUKI, Y. & PALEVITZ, B.A. *Fluorescence and morphometric studies on cytochalasin-treated cells* **97**, 283-295 (1990).

Chapter 2

REPORTERS FOR SENSITIVE AND QUANTITATIVE MEASUREMENT OF AUXIN RESPONSE

Che-Yang Liao[1], Wouter Smet[1], Geraldine Brunoud[2],
Saiko Yoshida[1], Teva Vernoux[2] and Dolf Weijers[1],*

1. Laboratory of Biochemistry, Wageningen University, Wageningen, the Netherlands
2. Laboratoire de Reproduction et Développement des Plantes, CNRS, Institut national de la recherche agronomique, Ecole Normale Superieure Lyon, Lyon, France

Abstract

The visualization of hormonal signaling input and output is key to understanding how multicellular development is regulated. The plant signaling molecule auxin triggers many growth and developmental responses, but current tools lack sensitivity or precision to visualize these. We developed a set of fluorescent reporters that allow sensitive and semi-quantitative readout of auxin responses at cellular resolution in Arabidopsis. These generic tools are suitable for any transformable plant species.

The signaling molecule auxin plays a fundamental role in plant development. Gene expression responses to auxin mediate most patterning processes[1], but also underlie differential growth in response to light or gravity[2]. The ability to visualize sites of auxin response in a dynamic and quantitative manner is therefore of great importance for understanding mechanisms and dynamics of auxin-controlled plant development.

Auxin initiates signaling by binding to the nuclear auxin receptor TRANSPORT INHIBITOR RESISTANT1/AUXIN F-BOX(TIR1/AFB) in SKP1-CULLIN1-F-BOX (SCF) ubiquitin ligase complexes[3, 4]. This binding increases the affinity between SCF(TIR1/AFB) ubiquitin ligase complexes and their substrates, AUXIN/INDOLE-3-ACETIC ACIDs (Aux/IAAs)[5], which act as inhibitors of AUXIN RESPONSE FACTORs (ARFs)[6]. ARFs are transcription factors that recognize auxin response elements (*AuxRE*s)[7] in promoter regions and regulate gene expression[8]. Degradation of ubiquitin-modified Aux/IAA proteins releases ARFs from inhibition, allowing activation or repression of auxin responding genes (reviewed in ref. 9).

A widespread reporter of auxin response, the synthetic *DR5* promoter, consists of 7-9 *AuxRE* repeats and marks sites of transcriptional auxin response by activating reporter genes such as β-glucuronidase[10], fluorescent proteins[11], or luciferase[12]. While *DR5* marks many auxin-dependent processes[10], several other processes are not accompanied by its activity[13, 14]. Notably, computational modeling of auxin accumulation patterns based on the topology and dynamics of the auxin transport network predicted auxin gradients in the root tip, but these cannot be directly visualized[15]. Sites of *DR5* expression are thus often referred to as auxin "maxima".

The *AuxRE* in the *DR5* promoter was first identified through deletion analysis of a single auxin-responsive promoter in soybean[10]. We recently solved crystal structures of two functionally divergent ARFs and systematically determined binding sites through Protein Binding Microarrays[16]. This analysis revealed that the *AuxRE* in *DR5* is not a high-affinity binding site and identified another site (*TGTCGG*) with higher affinity[16]. It is thus conceivable that the limited sensitivity of *DR5* reporters is due to the use of a medium-affinity ARF binding element.

To address the question of sensitivity, we replaced the 9 original *AuxRE*s in the *DR5-rev* promoter[10] with this novel binding site and named the new reporter *DR5v2*. To directly compare the reporters without the confounding effects of transgene integration site and expression level, we fused each to a different nuclear localized fluorescent protein and expressed both from a single transgene in *Arabidopsis thaliana* (Fig. 1a). *DR5v2* lines exhibited broader expression compared to *DR5*. During embryogenesis, *DR5v2* expression is comparable to *DR5* until the early globular stage (Fig. 1b). From transition stage onward, additional expression domains in *DR5v2* appear and then become more

distinct in the incipient cotyledon and vasculature (Fig. 1c) where auxin response is required for normal development[17].

In the post-embryonic root, both reporters mark quiescent center, columella root cap and protoxylem (Fig. 1d,e) but *DR5v2* is also expressed in metaxylem, pericycle (Fig. 1e), lateral root cap (Fig. 1f) and epidermal cells (Fig. 1g). Strikingly, the epidermal cells expressing *DR5v2* were trichoblasts (Fig. 1g), which require auxin response for normal root hair development[13]. In the (first rosette) leaf primordia, both *DR5v2* and *DR5* report auxin maxima in the most distal domain and incipient leaf vein; however, *DR5v2* also shows expression in surrounding cells and the L1 layer (Fig. 1h,i).

These additional *DR5v2* expression domains match predicted auxin accumulation sites based on polar auxin transporter localization[14]. Comparing separate *DR5v2* and *DR5* reporter lines driving the same fluorescent protein confirmed that extended expression of *DR5v2* was not due to using different fluorophores (Supplementary Fig. 1). Importantly, *DR5v2* reported low-level activity in most cells within dividing regions of the embryo, leaf and shoot meristem, consistent with the known involvement of auxin in cell division and elongation[18]. This suggests that the *DR5v2* reporter is sufficiently sensitive to detect these more generic auxin responses. Interestingly, while all sites of *DR5* activity are also marked by *DR5v2*, the relative intensity across cell types is not identical. For example, in roots *DR5* has the highest expression in the QC, while *DR5v2* has increased response in subtending columella cells (Fig. 1d). This presumably reflects a difference in binding affinity towards *TGTCTC* (*DR5*) and *TGTCGG* (*DR5v2*) by the ARFs that are differentially expressed or active in each cell type.

We next tested if the extended domain of *DR5v2* expression correlates with increased sensitivity to auxin. We treated *DR5*-n3EGFP/*DR5v2*-ntdTomato double reporter seedlings with a range of exogenous auxin concentrations and monitored gene activation using qRT-PCR (Fig. 1j,k; Supplementary Fig 2) and microscopy (Fig. 1l; Supplementary Fig. 3). While both *DR5* and *DR5v2* responded to concentrations as low as 3 nM (Supplementary Fig. 3), the amplitude of response was much higher for *DR5v2* at all concentrations tested. qRT-PCR of GFP and tdTomato transcripts excluded any contribution of fluorescent protein folding and/or stability to differential signal intensity (Fig. 1j). Likewise, the larger amplitude of *DR5v2* response is distinctly visible after prolonged treatment with the same auxin concentration (Fig. 1k,l). Thus, while both reporters respond to the same range of auxin concentrations (Supplementary Fig. 3), the increased amplitude of *DR5v2* response allows *in vivo* detection of 10-fold lower auxin concentrations (Fig. 1l). It is important to note that neither reporter shows a linear response to auxin concentrations (Fig. 1j) or treatment duration (Fig. 1k), and hence cannot be used to infer actual auxin levels. However, the highly sensitive *DR5v2* reporter does enable the visualization of previously unobserved weak auxin responses.
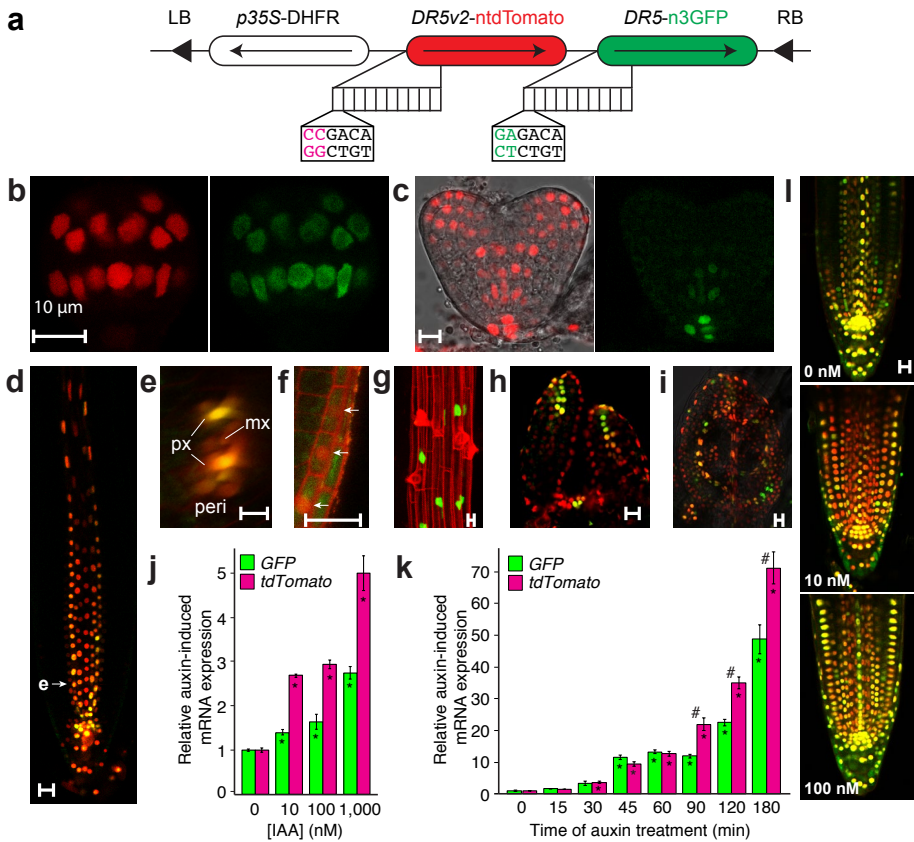
Figure 1. DR5v2 sensitively reports auxin response

(a) Schematic of DR5v2-ntdTomato/DR5-n3GFP double reporter. Ten repeats of either *TGTCTC* (*DR5*) or *TGTCGG* (*DR5v2*) are positioned in reverse orientation upstream of a minimal promoter and either nuclear 3xeGFP (n3GFP) or nuclear tandem Tomato (ntdTomato). *LB/RB*, Left/Right Border; DHFR, Methotrexate resistance gene. (b-j) *DR5v2* (red) and *DR5* (green) activity in early globular (b) and heart stage (c) embryos, root tip (d, longitudinal section; e, transverse section along plane at arrow in d; px, protoxylem; mx, metaxylem; peri, pericycle), lateral root cap (f), root epidermis (g, shown as a projection in a *DR5v2::n3eGFP* root), SAM (h) and young leaf (i). (j,k) Relative GFP and tdTomato transcript level in *DR5v2-ntdTomato/DR5-n3GFP* seedlings (j) after 12 h pre-treatment with 10 µM NPA followed by 2 h treatment with different auxin (IAA) concentrations, or (k) for different times on 1 µM IAA without NPA pre-treatment. Expression in mock treatments is set to 1. Bars indicate s.e.m. (n = 3). *, significant difference in expression compared to untreated control,#, significant difference between DR5 and *DR5v2* (Two-tailed t-test; p<0.05). (l) Visualization of *DR5v2-DR5* double reporter activity in root tips after 12-h co-treatment of 10 µM NPA with indicated IAA concentrations. All scale bars are 10 µm.

Any novel auxin response site would benefit from confirmation by an independent reporter. The recently developed DII-Venus reporter is a fusion of the auxin-dependent degradation domain II of an Aux/IAA protein to Venus fluorescent protein, such that the absence of fluorescence marks auxin accumulation[19]. Comparison with control lines that lack auxin-dependent degradation (mDII-Venus) allows for semi-quantitative measurement of 'auxin input'—sites where auxin accumulation promotes degradation—independent of downstream gene regulation. However, the *35S* promoter used in DII-Venus is not ideal for several developmental processes such as embryogenesis[20].

We therefore generated lines that express DII-Venus and mDII-Venus from the *RPS5A* promoter, which is active in most dividing cells[21] and thus encompasses most sites of auxin response in growth and development. These lines allow auxin activity to be observed in embryos and meristems (Supplementary Fig. 4), but quantification requires a comparison of signal in different lines, which is challenging and not ideal. To overcome this, we designed a single reporter named R2D2 (ratiometric version of 2 DIIs) that combines *RPS5A*-driven DII fused to n3xVenus and *RPS5A*-driven mDII fused to ntdTomato on a single transgene, and measures auxin accumulation as a reduction of yellow relative to red signal (Fig. 2a). The utility of such a ratiometric approach has recently been demonstrated[22, 23]. Indeed, untreated root tips gave qualitatively similar results to separate DII and mDII lines (Supplementary Fig. 4), but allowed a comparison of signal at cellular resolution (Fig. 2b-k). We implemented a simple image analysis algorithm (Online Methods) to infer relative auxin distribution. Following background subtraction, the yellow/red ratio of each pixel was calculated and visualized in false-color scale in real time. We plot the inverse of the ratio such that an increased signal corresponds to higher auxin (Fig. 2f).

During early embryogenesis, auxin input detected by R2D2 is consistent with auxin response detected by *DR5* and *DR5v2*; both are high in the embryo proper until globular stage[11] (Fig. 2b), and then confined to incipient cotyledons, vasculature, and hypophysis and its daughter cells in heart stage (Fig. 2c). From heart stage, however, an additional domain of auxin input in the shoot apical meristem (SAM) is only detected by R2D2 (Fig. 2c; Supplementary Fig. 5). The finding that auxin is present without eliciting a response in these cells is consistent with the fact that they express several key auxin biosynthetic enzymes[24] and was also predicted and demonstrated for the post-embryonic shoot meristem[25]. In post-embryonic root (Fig. 2d-g), young leaves and leaf primordia (Fig. 2h,i), and shoot apical meristem (Fig. 2i), in addition to confirming auxin response shown by *DR5v2* (Fig. 1), R2D2 revealed quantitative properties of early auxin signaling.
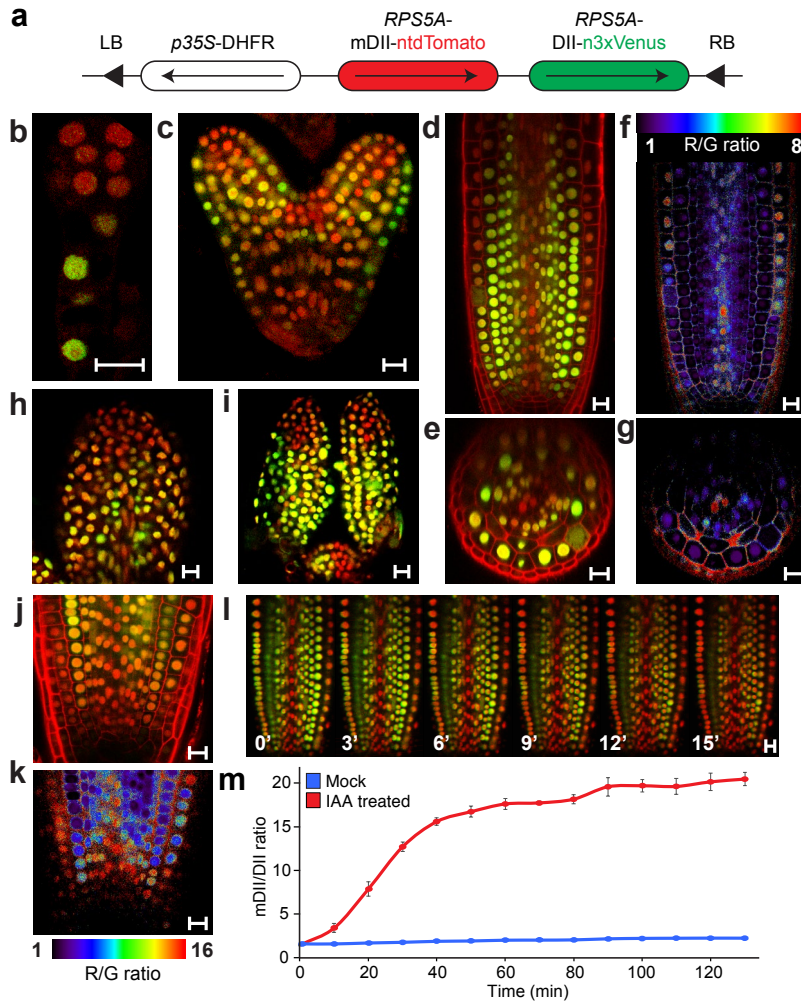
Figure 2. R2D2, a semi-quantitative and rapid auxin input reporter

(a) Schematic of R2D2. LB/RB, Left/Right Border; DHFR, Methothrexate resistance gene. (b-k) ntdTomato (red) and n3xVenus (green) fluorescence signal overlays (b-e, h-j) and inverse n3x-Venus/ntdTomato signal ratio (f,g,k) in pre-globular (b) and heart stage (c) embryos, root tip (longitudinal section in d,e; radial section in e,g; detail in j,k), young leaf (h) and SAM (i). Note the descending gradient of auxin input in the root apical meristem in (j,k). (l) Successive images of R2D2 root tips treated with 1 µM IAA for the indicated time. (m) Whole-frame quantification of inverse n3xVenus/ ntdTomato signal ratio after treatment with 1 µM IAA and untreated mock control. Bars indicate s.e.m. (n=3). Scale bar in panels (b-l) is 10 µm.

We used R2D2 to address whether auxin gradients, as predicted by simulations based on the transport network[15] and inferred from comparison of DII-Venus and mDII-Venus roots[19], could be visualized directly. We noticed that a steep gradient could be observed in the cells closest to the quiescent center in the root tip. In all cell files except epidermis and xylem cells, auxin input levels decreased from maximum to background over a range of 6-7 nuclei (Fig. 2j,k; Supplementary Fig. 6). We interpret this gradient as entirely consistent with computational predictions of auxin localization[15]. Importantly, while average gradients could be inferred from comparison of DII-Venus and mDII-Venus lines[19], their accurate quantitative analysis requires a dedicated ratiometric tool such as R2D2.

In addition to being semi-quantitative, R2D2 also allows real-time observation of rapid changes in auxin accumulation at cellular resolution, due to the lack of need for transcription, translation and fluorophore maturation[19]. Indeed, treatment of R2D2 seedlings with exogenous auxin led to a rapid and uniform loss of yellow signal without an appreciable effect on red signal (Fig. 2l,m; Supplementary Movies 1 and 2).

The ability to visualize small molecules at high resolution is critical to unraveling their dynamic roles in regulating development. Here, we have developed a set of tools that allow sensitive and semi-quantitative detection of auxin signaling and response in plants. As the *AuxRE* is a generic ARF binding site[16], *DR5v2* is likely to be functional in any genetically transformable plant species, and dual-color imaging of high and medium-affinity ARF binding sites simultaneously would allow an extended range of auxin responses to be visualized at the same time as maxima. Likewise, R2D2 has the potential for reporting in any transformable plant species, although the choice of the promoter has to be adapted for specific tissues and cell types. Finally, combining *DR5v2* and R2D2 in a single-transgene, triple-color marker will enable auxin input and output to be correlated at high resolution, to pinpoint sites where auxin accumulation does not elicit a response. We expect that these tools will be crucial to defining and quantifying responses to auxin.

Accession codes

Plasmids and seeds described in this study have been deposited in Addgene (www.addgene.org; Deposit 71550) and the Nottingham *Arabidopsis* Stock Center (www.*Arabidopsis*.info), respectively.

Acknowledgements

Author contributions

C.L. generated all transgenic lines with the exception of RPS5A-DII-Venus lines, which were generated by G.B.. All imaging was performed by C.L. and W.S.. S.Y. contributed to analysis of DII-Venus lines. D.W. and T.V. supervised the project. C.L. and D.W. conceived the study and wrote the paper with input from all authors.

References

1. Lokerse, A.S. & Weijers, D. *Curr. Opin. Plant Biol.* **12**, 520-526 (2009).
2. Muday, G.K. *J. Plant Growth Regul.* **20**, 226-243 (2001).
3. Dharmasiri, N., Dharmasiri, S. & Estelle, M. *Nature* **435**, 441-445 (2005).
4. Kepinski, S. & Leyser, O. *Nature* **435**, 446-451 (2005).
5. Gray, W.M., Kepinski, S., Rouse, D., Leyser, O. & Estelle, M. *Nature* **414**, 271-276 (2001).
6. Tan, X. et al. *Nature* **446**, 640-645 (2007).
7. Ulmasov, T., Hagen, G. & Guilfoyle, T.J. *Science* **276**, 1865-1868 (1997).
8. Ulmasov, T., Hagen, G. & Guilfoyle, T.J. *Proc Natl Acad Sci U S A* **96**, 5844-5849 (1999).
9. Wang, R. & Estelle, M. *Curr. Opin. Plant Biol.* **21**, 51-58 (2014).
10. Ulmasov, T., Murfett, J., Hagen, G. & Guilfoyle, T.J. *Plant Cell* **9**, 1963-1971 (1997).
11. Friml, J. et al. *Nature* **426**, 147-153 (2003).
12. Moreno-Risueno, M.A. et al. *Science* **329**, 1306-1311 (2010).
13. Jones, A.R. et al. *Nat. Cell Biol.* **11**, 78-84 (2009).
14. Scarpella, E., Marcos, D., Friml, J. & Berleth, T. *Genes Dev.* **20**, 1015-1027 (2006).
15. Grieneisen, V.A., Xu, J., Maree, A.F.M., Hogeweg, P. & Scheres, B. *Nature* **449**, 1008-1013 (2007).
16. Boer, D.R. et al. *Cell* **156**, 577-589 (2014).
17. Hardtke, C.S. et al. *Development* **131**, 1089-1100 (2004).
18. Perrot-Rechenmann, C. *Cold Spring Harb Perspect Biol* **2**, a001446 (2010).
19. Brunoud, G. et al. *Nature* **482**, 103-U132 (2012).
20. Völker, A., Stierhof, Y.D. & Jürgens, G. *J. Cell Sci.* **114**, 3001-3012 (2001).
21. Weijers, D. et al. *Development* **128**, 4289-4299 (2001).
22. Federici, F., Dupuy, L., Laplaze, L., Heisler, M. & Haseloff, J. *Nat. Methods* **9**, 483-485 (2012).
23. Wend, S. et al. *Sci Rep* **3**, 2052 (2013).
24. Robert, H.S. et al. *Curr. Biol.* **23**, 2506-2512 (2013).
25. Vernoux, T. et al. *Mol. Syst. Biol.* **7** (2011).
26. De Rybel, B. et al. *Plant Physiol.* **156**, 1292-1299 (2011).
27. Llavata-Peris, C., Lokerse, A., Möller, B., De Rybel, B. & Weijers, D. in Methods in Molecular Biology, Vol. 959 137-148 (2013).
28. Daghma, D.S., Kumlehn, J., Hensel, G., Rutten, T. & Melzer, M. *J. Exp. Bot.* **63**, 6017-6021 (2012).

Materials and Methods

Plant material

DR5v2 was designed by replacing the 9 *AuxRE*'s in *DR5* (*TGTCTC*), with *TGTCGG*, and synthesized to generate cloning vector pUC57/*DR5v2* (GenScript). Double reporter *pGIIM/DR5v2::ntdTomato-DR5::n3eGFP* was created in two steps. *DR5* reporter cassette from *pGIIK/DR5::n3eGFP* was first excised by BamHI and EcoRI digestion and cloned into BamHI and EcoRI digested *pGIIM/LIC_SwaI-ntdTomato- LIC_HpaI-n3EGFP* (a kind gift from Thomas Laux, Freiburg) to create *pGIIM/LIC_SwaI-ntdTomato- DR5::n3eGFP*. *DR5v2* reporter cassette amplified from *pUC57/DR5v2* using primer set "*DR5v2*" was then cloned into SwaI-digested *pGIIM/LIC_SwaI-ntdTomato- DR5::n3eGFP* via Ligation Independent Cloning[26].

pGIIM/LIC_SwaI-ntdTomato-   DR5v2::n3eGFP   and   *pGIIM/LIC_SwaI-ntdTomato-DR5v2::n3VENUS* were created by excising *DR5v2* reporter cassette from *pUC57/DR5v2* via BamHI and EcoRI digestion followed by cloning into BamHI and EcoRI digested *pGIIM/LIC_SwaI-ntdTomato- LIC_HpaI-n3eGFP* or *pGIIM/LIC_SwaI-ntdTomato- LIC_HpaI-n3Venus*.

The *pRPS5A::DII-Venus* and *pRPS5A::mDII-Venus* binary vectors were constructed using the multisite Gateway technology (Invitrogen) and following the provider instructions. To do so, the *RPS5A* promoter was cloned in pDONR P4-P1R using primers listed in Supplementary Table 1. This vector was used together with the previously described DII/mDII cloned in pDONR221 and Venus fused to the N7 nuclear localization signal cloned in pDONR P2R-P3[19] for recombination in the binary gateway vector pH7m34GW (http://gateway.psb.ugent.be/).

R2D2 in *pGIIM/ RPS5A:: mDII: ntdTomato- RPS5A:: DII: n3Venus* was created through two subsequent Ligation Independent Cloning events. First, *RPS5A*:: DII reporter cassette amplified from genomic DNA of *pRPS5a:: DII: Venus* using primer set "pRPS5a:: DII" was cloned into HpaI digested *pGIIM/LIC_SwaI-ntdTomato- LIC_HpaI-n3Venus* (a kind gift from Thomas Laux, Freiburg) to create *pGIIM/LIC_SwaI-ntdTomato- RPS5A:: DII:n3Venus*. *RPS5A:: mDII* control cassette amplified from genomic DNA of *pRPS5a:: mDII: Venus* control line using primer set "pRPS5a:: mDII" was then cloned into SwaI digested *pGIIM/LIC_SwaI-ntdTomato- RPS5A:: DII:n3Venus* to create R2D2. Sequences of primers used for cloning aforementioned constructs are listed in Supplementary Table 1. All transgenic lines were first created in *Arabidopsis* Col-Utrecht ecotype.

Plant Growth condition

Arabidopsis plants were grown at 22°C in 16 hours light/ 8 hours dark cycle for every experiments. All seeds were surface sterilized, sown on half-strength Murashige and Skoog medium with 0.8% Daichin agar (Duchefa) (1/2 MS plate) if not mentioned otherwise, and vernalized at 4°C for 2 days. For microscopic analysis of root, seedlings were grown vertically for five days after transfer to growth chamber, while this period was decreased to three or four days for microscopic analysis in shoot.

Methotrexate (MTX) selection was conducted by growing sterilized seeds on 1/2 MS plates containing 0.1 mg/L MTX (Sigma; A6770).

For DR5/*DR5v2* auxin sensitivity analysis via qRT-PCR, surface sterilized seeds were sown on sterilized nylon mesh placed on 1/2 MS plates after stratification and grown in growth chamber for four days then transferred to 1/2 MS plates with 0.11% DMSO and 10 μM N-1-Naphthylphthalamidic acid (NPA; Chem Service) to inhibit auxin transport. After incubation for 12 hours, seedlings were transferred to plates containing 0.11% DMSO and 10 μM NPA with 0.01, 0.1, or 1.0 μM Indole 3-Acetic Acid (IAA; Duchefa) for treatments, 0.11% DMSO and 10 μM NPA for control for two hours before collection for RNA isolation.

For DR5/*DR5v2* auxin sensitivity analysis via confocal microscopy, surface sterilized seeds were sown on sterilized nylon mesh placed on 1/2 MS plates after stratification and grown in growth chamber for four days then transferred to 1/2 MS plates with 0.11% DMSO and 10 μM NPA with 0.0001, 0.000316, 0.001, 0.00316, 0.01, 0.0316, 0.1, 0.316, or 1.0 μM IAA for treatments, 0.11% DMSO and 10 μM NPA for control for 12 hours before collection for imaging.

For temporal DR5/*DR5v2* auxin response analysis, surface sterilized seeds were sown on sterilized nylon mesh placed on 1/2 MS plates after stratification and grown in growth chamber for five days then transferred to 1/2 MS plates with 0.01% DMSO and 1.0 μM IAA as treatment or 1/2 MS plates with 0.01% DMSO as control for given time before collection for RNA isolation.

Microscopic analysis

Images were acquired as 8-bit format using a Leica TCS SP5II confocal laser scanning microscope with 20× NA=0.75 and 63x NA=1.20 water-immersion objective and pinhole equivalent to 1.0× the Airy disk diameter. EGFP and VENUS were excited by argon ion laser while tdTomato and propidium iodide were excited using diode laser, and their emissions were detected sequentially with Leica HyD in standard mode to prevent cross-talks between fluorophores. Excitation and detection of fluorophores were configured as below, eGFP was excited at 488 nm and detected 498-530 nm; Venus was excited at 514 nm and detected 524-540 nm; tdTomato was excited at 561 nm and detected 571-630 nm; propidium iodide was excited at excited at 561 nm and detected 571-700 nm.

In comparisons of eGFP and tdTomato fluorescence in the same line, the highest fluorescence signal in reference cells listed below in each channel was used to set the upper limit of pixel intensity. Reference cells used to setup the upper limit of pixel intensity are lens shape cell of early heart stage when imagining embryos, quiescent center cells when imaging roots, and distal domain of leaf primordia when imaging shoot meristem and leaf primordial.

In comparisons of VENUS and tdTomato fluorescence in R2D2 line, the highest fluorescence signal in reference cells listed below in each channel was used to set the upper limit of pixel intensity. Reference cells used to setup the upper limit of pixel intensity are suspensor cells of early globular stage when imagining embryos, cortex cells when imaging roots, and trichome cells when imaging shoot meristem and leaf primordial.

Embryos were mounted in 1x phosphate solution saline (PBS) containing 4% paraformaldehyde and 5% glycerol as described[27], and seedlings were mounted in demineralized water unless mentioned otherwise with 10 µg/mL propidium iodide[4] for roots and without propidium iodide for shoot meristem, leaf primordial, *DR5v2* auxin sensitivity analysis, and R2D2 auxin treatment live imaging.

Seedlings for live imaging were mounted in modified devices described[28]. The original plastic mask was replaced by a 15.5 mm x 21.0 mmx 0.5 mm frame made of Bioplastic with 10.0 mm x 15.0 mm opening in the center at where was covered with 0.4 µm PTFE mesh. Only one plastic frame was used, but agarose and culture medium were also omitted. Five five-day-after-germination seedlings were placed in a two chamber coverglass containing 100 µL demineralized water then covert by PTFE frame with 0.4 µm PTFE mesh facing to seedlings followed by adding 900µL of demineralized water to

cover the roots. This device allows imaging multiple roots at identical condition at once via confocal microscope. Time interval and coordinates of regions of interest were first defined, and images referred as "0 sec" were taken before adding 111 µL of 0.1% DMSO or 10 µM IAA in 0.1% DMSO.

Virtual ratio images of R2D2 were generated by "Calcium Imaging Calculator" built in Leica LAS AF lite v2.6.3 or v 3.7.x (http://www.leica-microsystems.com/products/microscope-software/life-sciences/las-af-advanced-fluorescence/) through calculating ratios between signal intensities of each pixel from two channels after subtracting noise, which was defined as the average signal intensity of six 2.5-3.5 µm^2 area in the cytoplasm of six epidermal cells from a single image and used for the rest of images taken with the same laser/detection configuration. (See Supplementary Note 1)

To monitor auxin gradient in the root apical meristem by R2D2, images from three z-stacks with 2.0 µm interval were acquired. The maximum projection of three images was examined to assure the section of region of interest contains only single cell layer. Approximate 10 µm^2 area in nucleus of cell of interest was selected via the ROI tool, and the ratio of red/yellow signal ratio was calculated by "Calcium Imaging Calculator" built in Leica LAS AF lite v2.6.3 or v 3.7.x after noise subtraction. Red/yellow ratio of the first 7-10 continuous cells (depending on number of cells in each frame of images due to the different cell size of each tissue) from the quiescent center was acquired form 32 roots of R2D2 line. Cells from both sides of roots were used if possible to generate 32 to 47 data sets of each tissue.

Quantitative RT-PCR Analysis

Over 100 roots from treatments were collected and RNA was extracted with Plant RNeasy kit (QIAGEN). Poly(dT) cDNA was prepared from 600 ng total RNA with an iScript cDNA Synthesis Kit (Biorad). Primer pairs were designed with Beacon Designer 8.0 (Premier Biosoft International). Although the fluorescent proteins are tandem repeats (tandem dimer Tomato and 3xeGFP), we designed primers that generate a single amplicon per transcript. Primers were tested in qRT-PCR using serial diluted *pGIIM/DR5v2::ntdTomato-DR5::n3eGFP* plasmid as template to validate the correspondence between amount of amplicons and actual templates (See Supplementary Fig.2). qRT-PCR was conducted with iQ SYBR Green Supermix (BioRad) on CFX384 Real-Time PCR detection system (BioRad) according to the manufacturer's instructions. Efficiency of primers for subjected cDNA, ntdTomato and n3eGFP, and concentrations of subjected cDNA in all samples have been tested in advance to ensure expressions of *n3eGFP* and *ntdTomato* are comparable. All individual reactions were done in triplicate with two biological replicates. Data were analyzed with qBase[5]. Expression levels were

normalized to those of *EEF1α4*, *GAPC*, and *iEF4A*. Sequences of primers used for qRT-PCR were listed in Supplementary Table 1.

To compare qRT-PCR results, normalized data sets acquired form qBase were subjected to two-tailed Student's t-test with threshold (alpha level) of 0.05 to determine if significance of the difference between each treatment.

Methods-only references

26.   de Rybel, B.D. et al. *Plant Physiol.* **156**, 1292-1299 (2011).
27.   Llavata-Peris, C., Lokerse, A., Möller, B., De Rybel, B. & Weijers, D. in Methods in Molecular Biology, Vol. 959 (ed. Clifton, N.J.)137-148 (Humana Press, 2013).
28.   Daghma, D.S., Kumlehn, J., Hensel, G., Rutten, T. & Melzer, M. *J. Exp. Bot.* **63**, 6017-6021 (2012).
29.   Van Den Berg, C., Willemsen, V., Hage, W., Weisbeek, P. & Scheres, B. *Nature* **378**, 62-65 (1995).
30.   Hellemans, J., Mortier, G., De Paepe, A., Speleman, F. & Vandesompele, J. *Genome biology* **8**, R19 (2007)

Supplementary information

DR5-n3GFP   DR5v2-n3GFP

DR5-n3GFP/DR5v2-ntdTomato plasmid (fg)
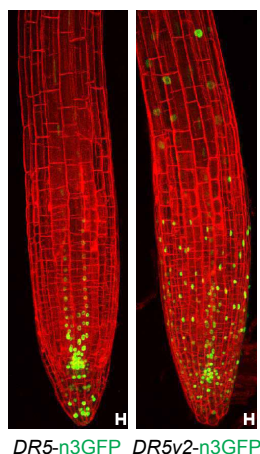
Supplementary Figure 1 Overview comparison of *DR5* and *DR5v2* activity in root tip.
Maximal projection of propidium iodine stained root of (a) DR5:: n3eGFP and (b) DR5v2:: n3eGFP reporter lines. Scale bars are 10 μm.
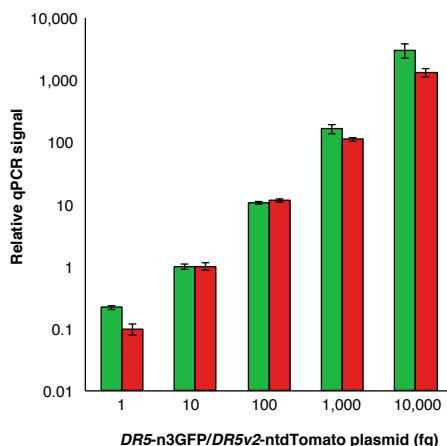
Supplementary Figure 2 Performance of primers against tandem repeated reporter genes.
qRT-PCR of serial diluted serial diluted pGIIM/DR5v2::ntdTomato-DR5::n3eGFP plasmid with primers used in this study. Bars indicate standard error from the mean (n=3).
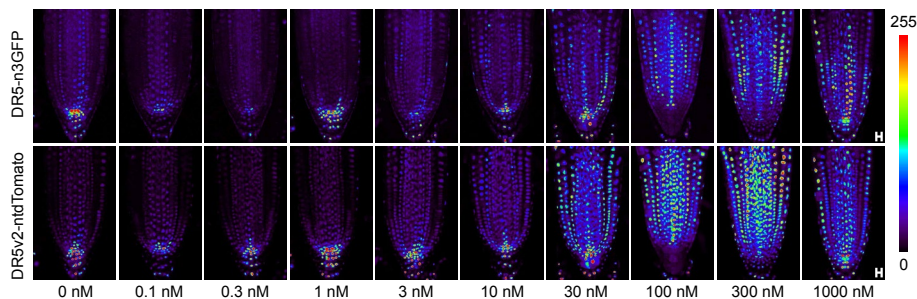
Supplementary Figure 3 Response of *DR5* and *DR5v2* to external auxin.
Fluorescent signal intensity of n3xGFP (top row) and ntdTomato (bottom row) in DR5v2::ntdTomato-DR5::n3eGFP root tips following a 12-hour co-treatment of 10 μM NPA and the indicated concentrations of IAA. Detector gain was saturated for each channel separately at the highest signal intensity of the 1000 nM IAA treated root, and all other images were acquired using these same settings. Signal intensity is displayed as a false color scale. Scale bars are 10 μm.

RPS5A - DII-Venus   *RPS5A -* mDII-Venus

DR5v2 - n3GFP

R2D2
(RPS5A -mDII-ntdTomato/
RPS5A -DII-n3xVenus)
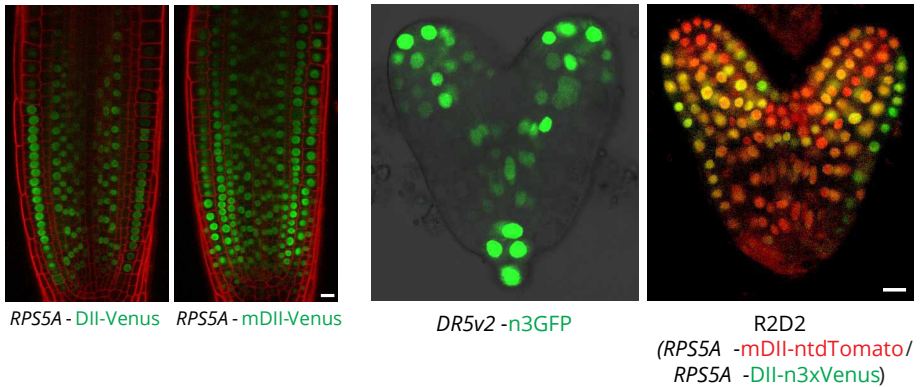
Supplementary Figure 4 pRPS5a::DII:Venus and pRPS5a::mDII:Venus root tips.

(a) pRPS5a:: DII: Venus and (b) pRPS5a:: mDII: Venus. Scale bars are 10 µm.

Supplementary Figure 5 DR5v2-n3GFP and R2D2 heart-stage embryos.

Scale bars are 10 µm
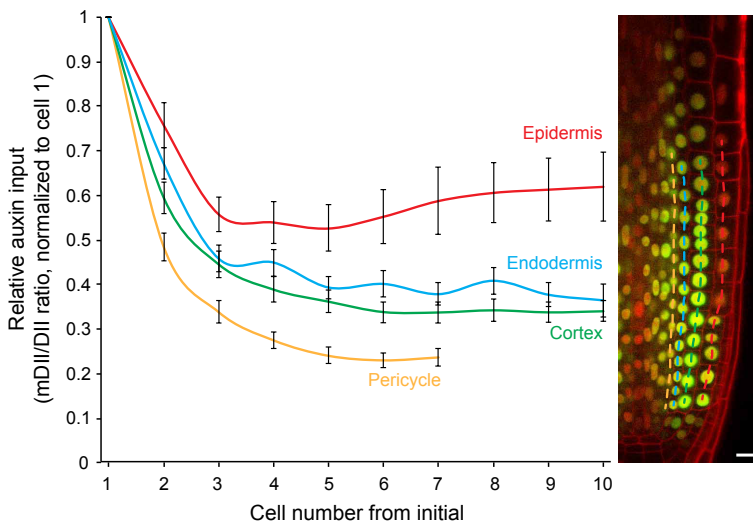
Supplementary Figure 6 Quantification of R2D2 gradients.

Normalized ntdTomato/n3xVenus signal ratio in nuclei at increasing distance from the QC (see dashed lines in image on the right). Cell 1 corresponds to the first daughter of the initial for each cell file. Red/yellow ratio was set to "1" in cell 1 for each cell file. Bars indicate standard error from the mean (n>30 cell files per tissue). Scale bars are 10 µm.

Supplementary Table 1. Primers used in this study

Primer set	Forward primer	Reverse primer
DR5v2	TAGTTGGAATAGGATTTCGA	AGTATGGAGTTGGATTTCGG
pRPS5A	GGGGACAACTTTGTATAGAAAAGT TGCTGGTACCGGGCCATAATCGTG	GGGGACTGCTTTTTTGTACAAACT TGCGGTACCCGCCTGTGGTGAG
pRPS5A:: DII (for R2D2)	TAGTTGGAATAGGATTTCCC GGGCCATAATCGTGAGTAGA	AGTATGGAGTTGGATTTCCC TCTCCGGGATGATCTCACCG
pRPS5A::mDII (for R2D2)	TAGTTGGAATAGGGTTCGG GCCATAATCGTGAGTAGA	AGTATGGAGTTGGGTTCTC TCCGGGATGATCTCACCG
qPCR_EGFP	ACGTAAACGGCCACAAGTTC	AAGTCGTGCTGCTTCATGTG
qPCR_tdTomato	ACCACCTGTTCCTGGGGCAT	GGCCATGTTGTTGTCCTCGG
qPCR_EEF1	CTGGAGGTTTTGAGGCTGGTAT	CCAAGGGTGAAAGCAAGAAGA
qPCR_GAPC	GAAGGGTGGTGCCAAGAAGGTT	AGGGGAGCAAGGCAGTTAGTGG
qPCR_eIF4a	CTCATCACCACTGACCTCTTAGC	AACCTTCCACTTCTTCCGATACG

Supplementary Note

1. Open LAS AF lite and select specimen to be analyzed. In the following example figures, Channel.001 represent the signal form 571-700 nm (mDII-ntdTomato and propidium iodide), and Channel.002 represent the signal form 524-540 nm (DII-n3VENUS).

2. In "Quantify" (1), select "Stack profile" (2) and set dimension to "Frame"(3)
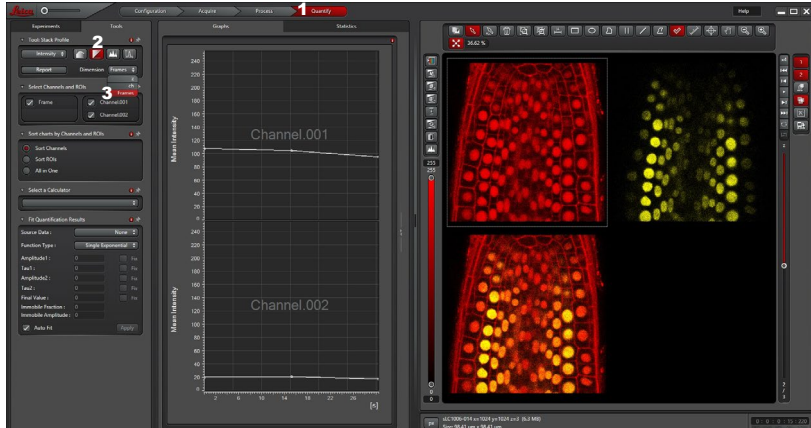
3. In "Select a calculator,"(1) select "Calcium imagining"(2)
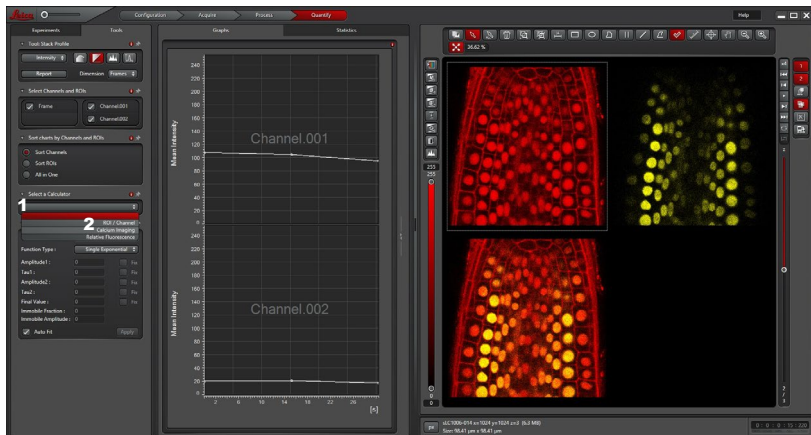
4. Define more than five Region of interest (RIOs) that will be use to determine background signal in the cells. After selecting "Statistics" (1), the signal values can be found in the rows of "Mean value" (2). The data can be retrieved in to an Excel file using "Export" (3) to calculate the average "Background" in both channels. These values will be used as "Background" that will be subtracted in all images taken in this particular experiment.
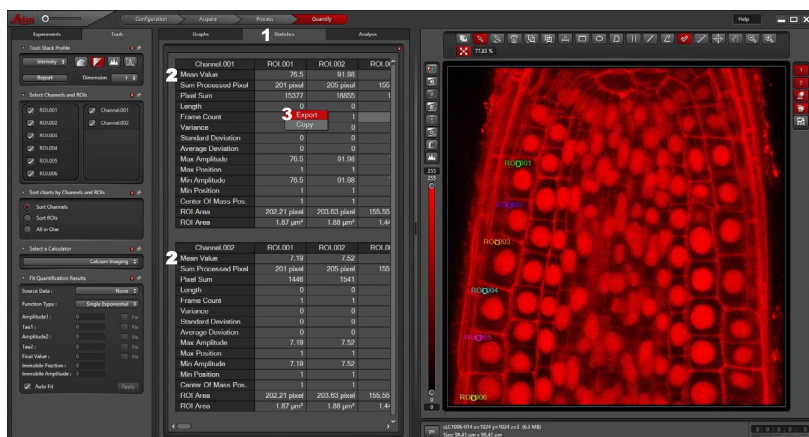
5. In "Analysis" (1), setup the formula as below and enter the "Background" from Step 4. Minus 2 to 5 in "Background" of Channel.002 (DII-n3VENUS), for example, enter 6 instead of 8, which is the "Background" calculated form Step 4, is suggested (2). This prevents the complete subtraction of background signal in the auxin maxima, where all DII-n3VENUS could be completely depleted, that will lead to "0" in the denominator of the formula and subsequent "0" in the ratio. Minus more than 5 is not suggested since this may lead to a significant underestimation of auxin input.
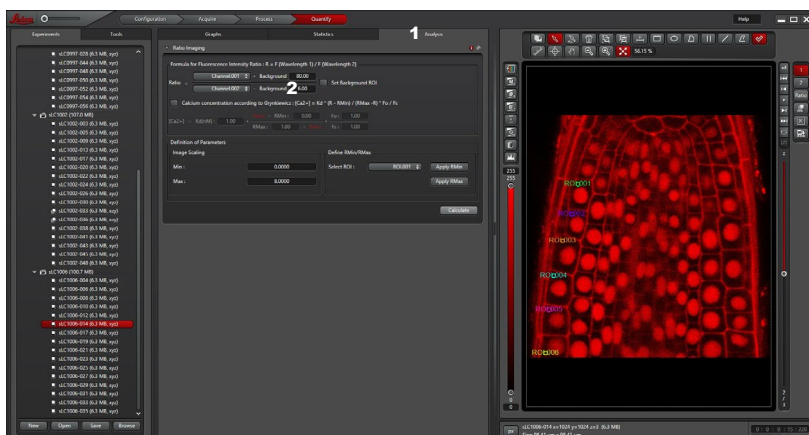
6. Define the ratio parameter in "Definition of parameter" (1). The entered value only affects the visual representation of the ratio image generated after selecting "Calculate" (2) and "Ratio" (3). The ratio image can be exported by right-clicked the specimen (4) and select "Export (image name)" and "Export view", subsequently. Ratio images of other specimens in the same experiment can now be generated by selecting specimen of interested without reset the formula.
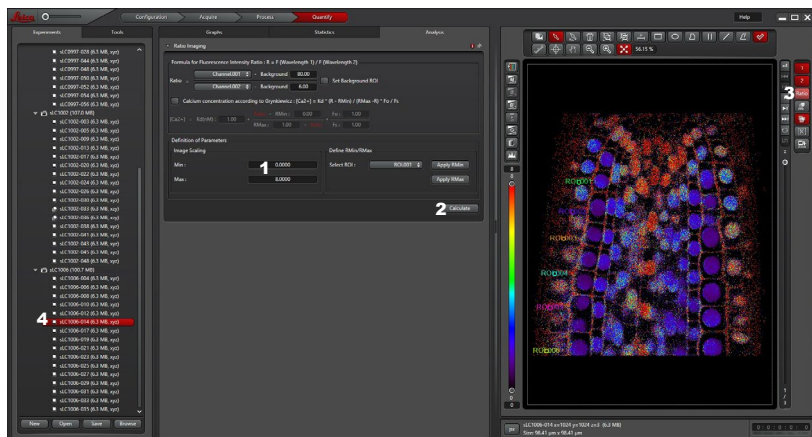
7. Define ROIs to quantify auxin input. A z-stack of single cell layer is suggested to acquire nuclei of all cell types of interest in one image.
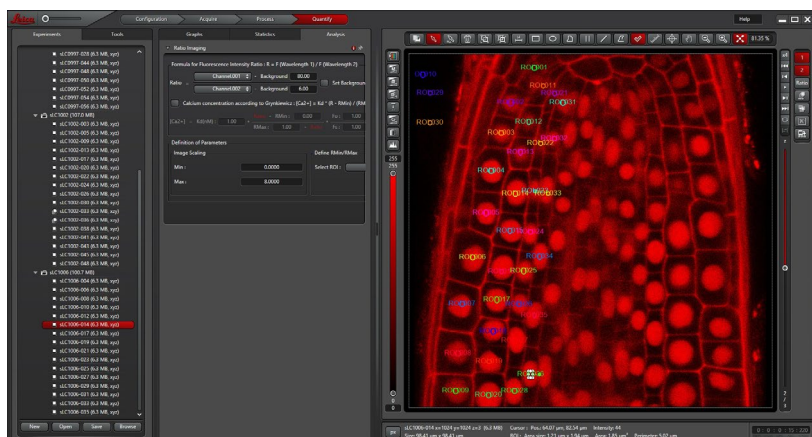
8. If two nuclei overlap, the data is not viable. Move between stacks to find possible overlaps and confirmed by using "Maxima projection"(1).
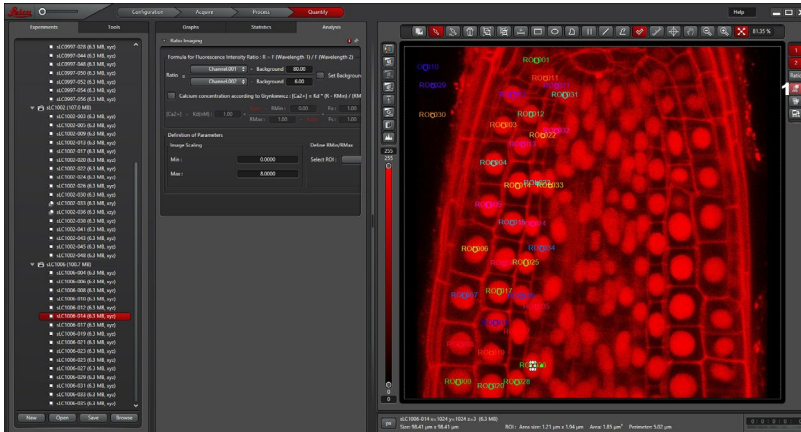
9. Select "Statistics"(1) and the reverse of DII/mDII can be found in "Ratio"(2). All data can be retrieved using "Export"(3) to Excel for further analysis.
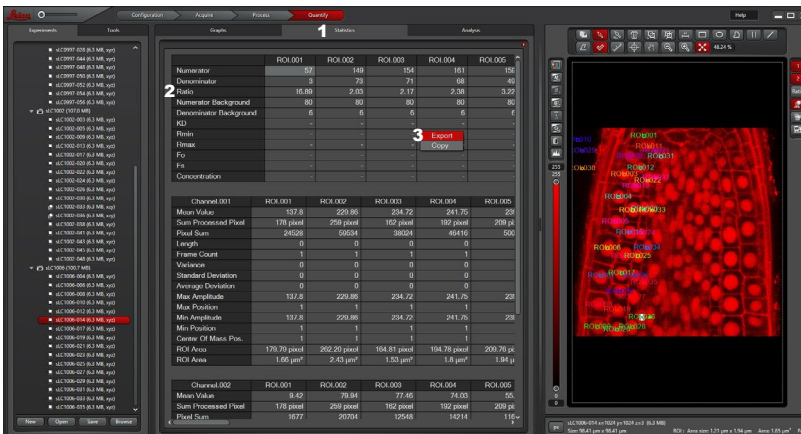
Chapter 3

OPTIMIZED AUXIN RESPONSE REPORTERS REVEAL DIFFERENCES IN LOCAL SIGNALING CAPACITY

Che-Yang Liao and Dolf Weijers

Laboratory of Biochemistry, Wageningen University, Wageningen, the Netherlands

Abstract

The phytohormone auxin has a great impact on wide spectrum of growth and developmental processes. Its activity is mediated by a short nuclear signaling pathway that involves targeted degradation of transcriptional inhibitors and subsequent transcription regulation. A key challenge in understanding the developmental roles of this hormone lies in the ability to directly visualize its activity in situ. Several response reporters have been widely used. These include the recently developed R2D2 degradation reporter and the *DR5v2* gene activation reporter. R2D2 and *DR5v2* offer improved precision and sensitivity compared to earlier reporters, but their design limits certain applications. Here, we describe a set of improvements that allow more generic application of these reporters. We first generated a ubiquitously expressed R2D2 and, following its characterization, combined it with *DR5v2* to generate the triple-color C3PO reporter. We demonstrate their potential through revealing hypothesized and new auxin maxima in various tissues and developmental stages in *Arabidopsis thaliana* showing differential auxin signaling capacity between cells. We also demonstrate the use of the *DR5v2* reporter to reveal patterns of auxin response during embryogenesis in the auxin response mutant *monopteros.* This reveals globally altered auxin maxima. The enhanced auxin reporters offer broad applications for comprehensive insight into the role auxin signal in plant biology.

Introduction

The phytohormone auxin plays a crucial role in regulating development throughout the plant life cycle, controlling processes ranging from embryogenesis to secondary growth (reviewed by [1-4]). To understand the involvement of auxin in a given developmental process, the first approach is tracking the presence and abundance of auxin in location of interest. Radioactively labeled auxin, indole-3-acetic acid (IAA)[5], immunolocalization of auxin[6] and direct mass spectrometry-based detection of auxin in protoplasts derived by fluorescence-activated cell sorting[7] have been used to directly detect auxin. While these approaches each have the distinct advantage of detecting the presence, and even absolute amount of auxin, these methods require the use of chemically fixed samples and/or treatments with auxin transport inhibitors[5-7]. These properties limit the application of these methods. In addition, as these approaches provide only a snapshot of auxin distribution, it is impossible to address dynamics of auxin accumulation. Besides the direct detection of auxin presence, auxin distribution have often been inferred from the polar localization of auxin efflux carriers (*PIN*s)[8-20] and influx carriers (*AUX1/LAX*s)[16, 21-25]. Auxin efflux and influx carriers can be tagged with fluorescent proteins and detected *in vivo* to allow long-term observation of developmental processes[12-14, 21, 26-28]. However, none of the aforementioned approaches can inform about the fraction of auxin that effectively induces a cellular response.

Despite the range of developmental events controlled by auxin, the auxin-signaling pathway, from perception to response, is short and simple. After auxin enters the nucleus, it is perceived by SKP1-CULLIN1-F-BOX (SCF) ubiquitin ligase complexes containing F-box auxin receptors TRANSPORT INHIBITOR RESISTANT1 (TIR1)[29, 30] or AUXIN F-BOX 1 to 3 (AFB1-3)[31]. Auxin facilitates binding between SCF(TIR1/AFB1-3) and AUXIN/INDOLEACETIC ACID proteins (Aux/IAAs) that leads to Aux/IAAs ubiquitination and their degradation[32, 33]. 29 *Aux/IAA*s are encoded in the *Arabidopsis thaliana* genome[34], and most Aux/IAAs consist of four domains: domain I recruits the Aux/IAA CO-REPRESSOR TOPLESS (TPL)[35, 36]; domain II interacts with SCF(TIR1/AFB1-3) in the presence of auxin and is required for auxin-induced degradation of Aux/IAAs[37-39]; domain III and IV binds to Aux/IAA targets, AUXIN RESPONSE FACTORS (ARFs)[40, 41]. ARFs are DNA-binding transcription factors that recognize specific sequences named Auxin Response Elements (*AuxREs*) in their target genes and regulate, through activation or repression, the expression of the target genes (reviewed by ref [42]).

Based on the knowledge of the auxin response pathway, several signaling reporters have been developed. A reporter to monitor auxin perception (here defined as the process from auxin-triggered binding between Aux/IAAs and SCF(TIR1/AFB1-3) to degradation of Aux/IAAs, exploits the auxin-dependent degradation of Aux/IAAs through binding between their domain II and SCF(TIR1/AFB1-3). Auxin perception

reporters consist of a minimal "degron" of domain II from an Aux/IAA protein (DII), fused to a fluorescent protein as "probe" driven by a constitutive promoter[43, 44]. In the presence of auxin, the "probe" is degraded like endogenous Aux/IAAs are, and this leads to a reduced fluorescence intensity. As a comparison for DII degradation and an indication of promoter activity in cells of interest, a point mutation is introduced into DII that prevents binding between mutated DII (mDII) and SCF(TIR1/AFB1-3). mDII then is fused with a fluorescent protein as "control" driven by same constitutive promoter used for "probe." The first such auxin perception reporter, DII-VENUS, has "probe" and "control" separated in different individual plants[43, 44]. While powerful, it is impossible to achieve cellular-level quantification of auxin perception because to interpret the DII-Venus signal in a cell, one needs the mDII-Venus reference in the same cell. An improved version, R2D2, has both "probe" and "control" fused with different fluorescent proteins and expressed from the same transgene in a single transgenic plant. Through computing the signal intensity ratio between "control" and "probe", which is referred as auxin input, a semi-quantitative readout of auxin perception level can be measured in each individual cell[45].

A conceptually different reporter to monitor auxin transcriptional response (here defined as the ARF-dependent target gene regulation following Aux/IAA degradation), exploits the direct activation of *ARF* target genes during auxin response. A response reporter can be either the promoter of an auxin-activated gene, for example the soybean *GH3*[46-50] or *Arabidopsis IAA2*[14, 51-54] genes, or a synthetic promoter consisting of *AuxRE*s followed by a minimal Cauliflower mosaic virus *35S* promoter, driving a reporter gene. Examples of such synthetic promoters are *DR5*[55] and its high-affinity derivative *DR5v2*[45], and these have been used to drive expression of various reporter genes. In the presence of auxin, ARFs are released from Aux/IAA inhibition to activate reporter genes. Signal intensity from the reporter gene is thus a proxy for auxin output.

While R2D2- and *DR5v2*-based reporters have been very useful in visualizing auxin perception and response[56-61], both have intrinsic caveats, partly due to their design. In this work, we broaden the versatility of the original R2D2 reporter through replacing its promoter with another ubiquitous promoter. In addition, we established the first auxin reporter, C3PO, that can monitor both auxin input and output through combining R2D2 and *DR5v2*. Using the new R2D2 with ubiquitously expressed "probe" and "control" and triple reporter C3PO-R revealed previously unreported auxin input maxima, and also demonstrates differential auxin signaling capacity between cells. Furthermore, we used *DR5v2* to generate a high-resolution description of auxin response in the *mp* mutant, defective for *ARF5/MONOPTEROS* (*MP*), a critical ARF for embryonic root and vasculature tissue initiation[62]. *MP* is one of the five Class A ARFs predicted to act as

gene expression activator[63], that recognizes the high affinity auxin response element in *DR5v2*[64]. Mutants with loss of function mutations in *mp* fail at root initiation during embryogenesis[62, 64-67]. Strong *mp* mutants, such as *mp*[B4149] [68], therefore, have no root and can be easily distinguished from wild type embryos. Mutants with loss of function mutations in *mp,* therefore, shall reveal altered auxin output during developmental processes through auxin response reporter, *DR5v2*.

Collectively, these tools help visualize auxin input and response dynamics in both wild type and mutant development.

Results

A ubiquitously expressed R2D2 sensor generically reports auxin responses

Auxin response can be visualized through the degradation of Aux/IAA proteins, and this principle has been exploited by the generation of the DII-Venus sensor[43]. Since the levels of fluorescence by this negative auxin sensor cannot easily be interpreted without knowing the expression levels in the absence of auxin, we previously generated a ratiometric DII-VENUS version (R2D2), where DII-VENUS signals can be normalized to the fluorescence of a stoichiometrically co-expressed mutant DII (mDII) version coupled to a tdTomato fluorescent protein[45]. Here, auxin input levels are reflected by mDII/DII fluorescent ratios in nuclei. The original R2D2 version was expressed from the *Arabidopsis RPS5A* promoter[69], which is active in young, dividing cells. However, not only young cells respond to auxin [13, 15, 70-75], and several developmental auxin responses could thus not be visualized using R2D2. Therefore, we developed a new R2D2 version, this time driven from the *Arabidopsis UBIQUITIN10 (UBI10)* promoter, which was shown to confer broad expression in various organs[76, 77]. The *UBI10*-driven R2D2 construct (termed R2D2-U) was transformed into Columbia-0 wild type background. While the original R2D2 (termed R2D2-R) did not affect normal development (Fig. 1a, 1b), plants with strong expression of the R2D2-U showed distinctive developmental abnormalities. R2D2-U heterozygotes were identical to wild type at seedling stage (Fig. 1a), and only showed mild growth retardation at rosette/flowering stages (Fig. 1b). R2D2-U homozygotes, however, showed growth arrest at seedling stage (Fig. 1a), and growth retardation at both seedling and rosette/flowering stages (Fig. 1b). It is likely that high expression of a domain II from an *Aux/IAA* protein will interfere with the degradation of endogenous *Aux/IAA* proteins, and thus such developmental defects are not unexpected. Thus, we advise to cautiously use R2D2-U, but only when kept in heterozygous state.

We next surveyed R2D2-U expression in various organs. As expected, expression was broad in the root, with signals extending far into the elongation and differentiation zone (Fig. 1c), as well as in the root cap (Fig. 1d), where *RPS5A* is not active. The mDII/DII ratio in root tips also confirmed described[78] or predicted[14, 21] auxin accumulation peaks in the quiescent center (QC) area, epidermis, and in the vascular tissue (Fig. 1d). In addition, a differential auxin accumulation in more differentiated root parts could be detected with increased levels in the vascular tissue (Fig. 1c). In sharp contrast to R2D2-R, R2D2-U could be used to infer auxin response in the hypocotyl, with both components being expressed across cell types (Fig. 1e). Finally, R2D2-U was also ubiquitously expressed in the shoot apical meristem area (Fig. 1f) and in young leaves (Fig. 1g). In all these areas, ratio imaging showed local differences in auxin response (Fig. 1a-g).

Thus, despite the caveat of phenotypic abnormalities associated with high-level expression of R2D2 components, the new R2D2-U sensor allows to generically analyze auxin input at cellular level.
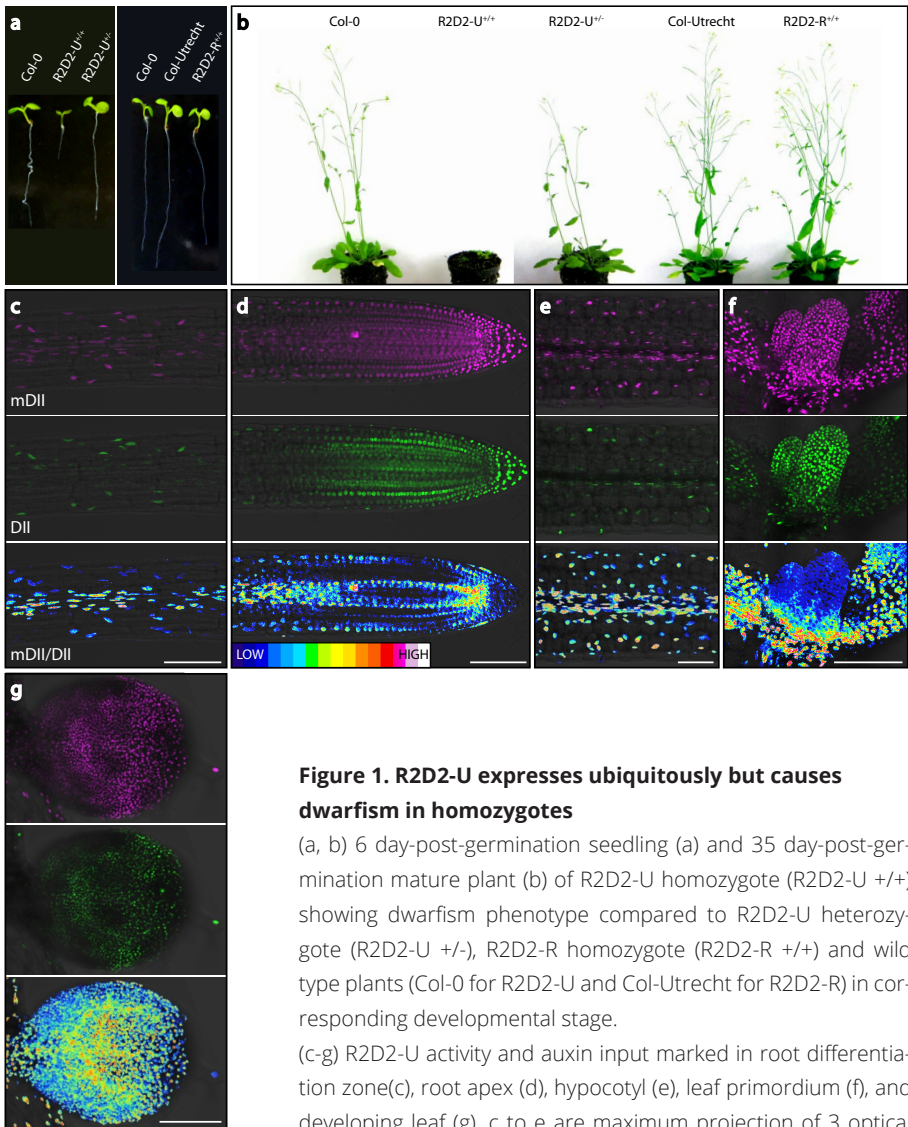
Figure 1. R2D2-U expresses ubiquitously but causes dwarfism in homozygotes

(a, b) 6 day-post-germination seedling (a) and 35 day-post-germination mature plant (b) of R2D2-U homozygote (R2D2-U +/+) showing dwarfism phenotype compared to R2D2-U heterozygote (R2D2-U +/-), R2D2-R homozygote (R2D2-R +/+) and wild type plants (Col-0 for R2D2-U and Col-Utrecht for R2D2-R) in corresponding developmental stage.

(c-g) R2D2-U activity and auxin input marked in root differentiation zone(c), root apex (d), hypocotyl (e), leaf primordium (f), and developing leaf (g). c to e are maximum projection of 3 optical sections (2 μm interval) in the middle plane of corresponding tissues; f and f are maximum projection of 15 optical sections (2 μm interval) from epidermis to the middle plane of corresponding tissues. Scale bar= 100.0 μm.

Differential auxin signaling capacities in root developmental zones and cell types

In the root apex, in addition to known auxin input maxima in vasculature and cells surrounding and within QC where high auxin concentration is expected (Fig. 1d), we identified two novel local auxin input maxima. Firstly, we found auxin input maxima in trichoblasts (root hair forming cells) between the end of the lateral root cap and the elongation zone. These auxin input maxima in trichoblasts persisted for 7 to 10 cells, and adjacent atrichoblasts (non-root hair forming cells) showed lower auxin input (Fig. 2a). Although the role of auxin transport via atrichoblasts to support root hair elongation has been described[25, 79], auxin input in these cells was not previously observed. Directly underneath the epidermal cells with increased auxin input located upstream of the end of lateral cap, cortex, endodermis and pericycle cells showed higher auxin input than their shootward and apical counterparts (Fig. 2b). This may be the domain where shootward transported auxin from lateral root cap and epidermis enter the vasculature predicted by the "auxin reverse fountain" model in the root apex[12, 14, 21].

Secondly, opposite to the new high auxin input domain, we found a lack of detectable auxin input in root cap cells, despite auxin input maxima in in adjacent cells (Fig. 2c). Interestingly, previous auxin response (*DR5*[78] and *DR5v2*[45]) and auxin concentration measurements[7] had shown that columella cells have high auxin levels and output. Thus, it is possible that differences exist in each cell type's capacity to degrade DII, irrespective of the level of auxin.

We next tested if there is differential auxin perception capacity between or within tissues. To test this hypothesis, auxin input was measured in root cap, epidermal cells in the meristem, elongation zone, and differentiation zone prior and after 30 minutes of mock (0.01% DMSO), 10 or 100 nM IAA treatment. Epidermal cells in the meristem showed the highest sensitivity toward auxin treatment by being able to perceive 10 nM of exogenous IAA. In contrast, epidermal cells in the elongation and differentiation zone only showed a significant change of auxin perception at 100 nM IAA treatment while root cap cells seemed insensitive to even 100 nM IAA treatment (Fig. 2d, Table. 1). These results suggest that capacity of auxin perception could vary from developmental stages of cells within same tissue and between tissues.
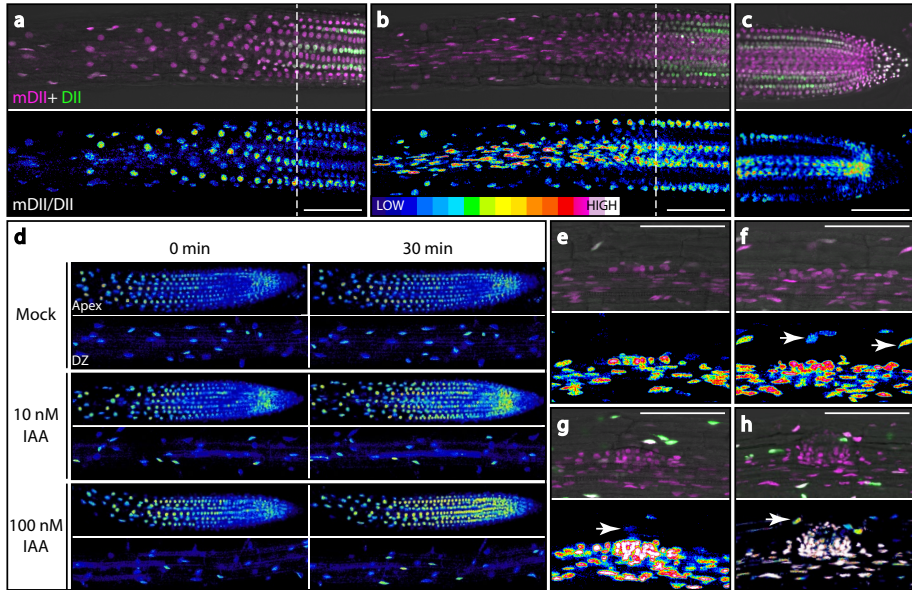
Figure 2. R2D2-U reveals auxin input maxima and differential auxin input in roots.

(a, b) R2D2-U marks high auxin input in trichoblasts (a) and moderate auxin input in cortex and endodermis (b) between meristem and elongation zone. Dash lines indicate the end of lateral root cap. Maximum projection of 3 optical sections (2 µm interval) in the surface (a) and middle plane (b) of root apex. (c, d) The absence of auxin input in root cap (c) and different auxin input level between root apex and differentiation zone (DZ) after auxin treatments (d). Maximum projection of 3 and 5 optical sections (2 µm interval) in middle plane in root tip (c) and epidermis (d), respectively. (e-h) Auxin input in lateral root primordia and overlying tissues in Stage I (e), -II (f), -III (g) and –IV (h). Arrows indicate auxin input in endodermal, cortex, or epidermal cells above lateral root primordia. Maximum projection of 3 optical sections (2 µm interval) in the middle plane of lateral root primordia. Scale bar= 100.0 µm.

Table. 1 Auxin input of epidermal cells from different developmental stages after auxin treatment

Average with standard divination (in parentheses) of signal ratio between mDII: ntdTomato and DII: n3Venus and from each developmental stage prior and after auxin treatments. * indicates significant difference (p< 0.01) between prior and after each treatment.

	Root cap (n= 18)		Meristem (n= 30)		Elongation zone (n= 30)		Differentiation zone (n= 30)	
	0 min	30 min	0 min	30 min	0 min	30 min	0 min	30 min
Mock	1.132 (0.329)	1.409 (0.390)	2.373 (0.411)	2.468 (0.482)	0.979 (0.329)	1.133 (0.343)	1.325 (0.955)	1.529 (0.823)
10 nM IAA	2.338 (0.202)	2.388 (0.250)	2.878 (0.598)	3.737* (0.503)	1.128 (0.277)	1.172 (0.335)	0.874 (0.272)	0.919 (0.253)
100 nM IAA	1.236 (0.587)	1.362 (0.807)	2.681 (0.678)	4.105* (0.825)	1.007 (0.229)	1.348* (0.262)	1.158 (0.520)	1.493* (0.610)

R2D2-U's ubiquitous expression also provides a tool for revealing auxin input in differentiated tissues and secondary growth. Lateral roots are generated from pericycle cells in the differentiated part of roots (reviewed by [80]), and visualization of auxin response during initiation requires expression of the sensor prior to initiation. Using R2D2-U, we showed that during lateral root development, at stage I (Fig. 2e), auxin input maxima were restricted to four cells in the pericycle and vasculature, while auxin input in surrounding tissues remained unaltered. At stage II (Fig. 2f) and III (Fig. 2g), auxin input maxima in primordia remained high, with outer primordia cells having higher auxin input level than inner ones. Auxin input levels in vasculature and endodermal cells directly above primordia increased. From stage IV (Fig. 2h), auxin input in primordia all increased to maximum level of our measurement scale, along with increased auxin input level in directly overlying endodermal cells.

Thus, the ubiquitously expressed R2D2-U sensor allows broad visualization of auxin maxima, and reveals intrinsic tissue differences in auxin perception.

High-resolution auxin response dynamics visualized by a three-color input/ output reporter

The notion of the differential capacity of auxin perception within and between tissues suggests that auxin perception may not be linearly translated into transcriptional output. To determine correspondence between auxin input and output at cellular level, we designed an integrated reporter that combines R2D2 and *DR5v2* auxin reporters. The reporter, termed C3PO, was generated by incorporating a *DR5v2::n3mTurqoise2* (blue fluorescence) cassette into the vectors harboring an R2D2-R auxin perception reporting cassette. C3PO-R was then introduced into Columbia-0 wild type background. Unlike R2D2-U, C3PO-R homozygotes with high expression of the reporting cassette showed no distinct phenotype at seedling and rosette/flowering stages (Fig. 3a, b).

In the C3PO-R root apex, the *RPS5A* promoter that drives the R2D2 auxin perception reporting cassette was most active in the root apical meristem; its activity then declined from the end of meristem towards the differentiation zone, where root hairs formed; the expression was undetectable in further differentiated tissue, root cap (Fig. 3c). In the meristem zone, both auxin input and output were lowest in the cortex while high auxin input and output was found in the vasculature and in cells surrounding the QC, along with high auxin output in root cap (Fig. 3c). When closely examining auxin input and output in the stele however, we found distinct differences in auxin input and output between cells. Xylem-pole pericycle cells adjacent to the QC had auxin input comparable to their adjacent vascular cells while these xylem-pole pericycle cells had lower auxin output than their adjacent vascular cells (Fig. 3d). Though auxin response in xylem-pole pericycle cells in the late basal meristem plays crucial role in lateral root priming[81-84], auxin response in xylem-pole pericycle cells in early basal meristem was not yet reported.

From the end of meristem to early elongation zone, a short auxin input maximum in trichoblasts and lower auxin input underneath, as detected in C3PO-R, were consistent with our observation in R2D2-U, with auxin output in trichoblast from the end of meristem (Fig. 3e). The maxima of auxin input and output in epidermis, however, did not completely overlap. Auxin output in trichoblasts reached its' maximum at the end of the auxin input maximum. The high auxin output persisted until the initiation of root hairs, while auxin input started to decline in the elongation zone (Fig. 3e). The difference between auxin input and output maxima could be due to differential capacity of auxin signaling between cell types (ex. low auxin input in atrichoblast, cortex, endodermis and pericycle upstream of lateral root cap coverage) and developmental stages (e.g.. trichoblast in meristem to differentiation zone).
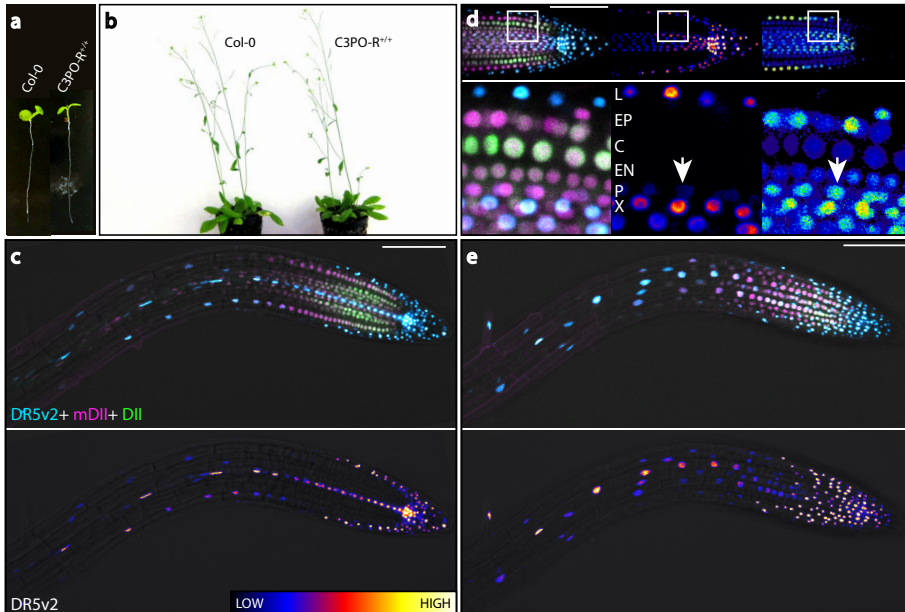
Figure 3. C3PO-R marks auxin input and output in the root apex

(a, b) 6 day-post-germination seedling (a) and 35 day-post-germination mature plant (b) of C3PO-R homozygote (C3PO-R +/+) and Col-0 wild type in corresponding developmental stage.

(c-e) C3PO-R activity in root apex in middle plane (c, d), epidermis and root cap (e). Note the position of the beginning and peak of auxin input and output in epidermis (c and e). Lower panel in d is marked region in upper panel in detail showing auxin input and output in xylem pole pericycle (arrow). L, lateral root cap; EP, epidermis; C, cortex; EN, endodermis; P, pericycle; X, Xylem. Maximum projection of 3 optical sections (2 µm interval) in the middle plane (c) and epidermis (e), and 3 optical sections (1 µm interval) in the middle plane of root apex (d). Scale bar= 100.0 µm.

During lateral root development, the *RPS5A* promoter in the C3PO-R line was active in lateral root primordia and surrounding cells from stage I to VIII (Fig. 4a-d). Throughout lateral root development, auxin input as observed in the primordia was consistent with our observation in R2D2-R. Auxin output, however, only overlaps with input from stage I to III (Fig. 4a). From stage IV (Fig. 4b, e) to VI (Fig. 4c), the auxin output maximum became restricted to the tip of the primordium, and in stage VII and VIII (Fig. 4d), auxin output maximum remained in tip of primordia with lower response in newly formed vasculature and epidermis.
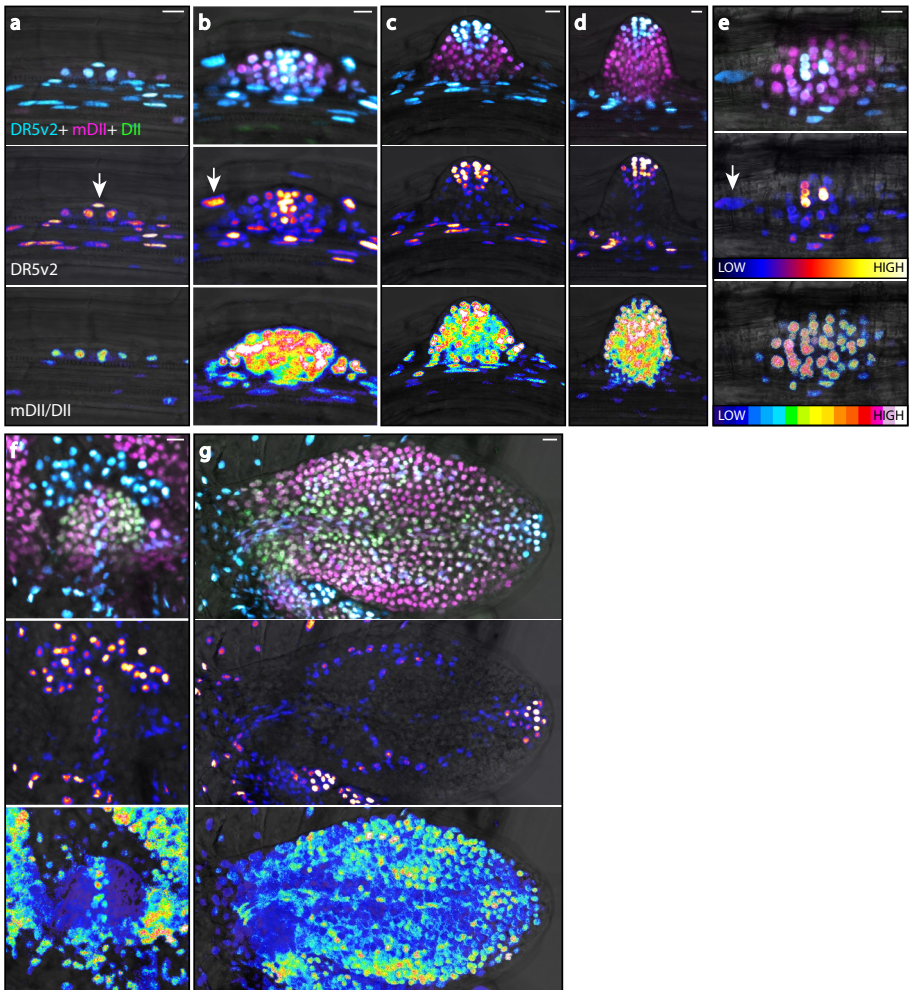
Figure 4. C3PO-R marks auxin input and output in lateral root primordia and in developing leaves

(a-e) Auxin input and output in lateral root primordial at stage I (a), -IV (b), -VI (c), –VIII (d), and –IV with primordium facing the viewer (e). Note that auxin input and output maxima do not completely overlap after stage IV. Arrows indicate auxin output in endodermal cells above lateral root primordia. Maximum projection of 3 and 5 optical sections (2 μm interval) in middle plane (a-d) and cortex to pericycle (e), respectively.

(f, g) Auxin input and output in leaf primordia (f) and developing leaf (g). Note the low auxin input in cells directly next to the leaf vein in g. Maximum projection of 10 optical sections (1 μm interval) in middle plane. Scale bar= 10.0 μm.

In the shoot apical meristem of seedlings (Fig. 4f), auxin input and output overlapped at prospective primordium initiation sites. In young developing leaves (Fig. 4g), auxin input and output overlapped although auxin input maxima were in the leaf veins and edge while auxin output maximum was in the leaf tip. Unlike auxin input maxima in other organs where the further the cells away from the maxima, the lower auxin input these cells have; cells directly adjacent to the auxin input maximum in the leaf veins had the lowest auxin input in young leaves (Fig. 4g).

Thus, through simultaneously observing auxin input and output, results from C3PO-R support our observation of differential capacity of auxin perception and response.

Auxin response patterns in the mp/arf5 mutant embryo

To test if the differential capacity of auxin response we observed was resulted only from the differential auxin perception or a combination of differential auxin perception and *ARFs*' expression pattern, we thus introduced the *DR5v2::n3Venus* reporter into *ARF5/MONOPTEROS (MP)* loss of function strong mutant allele *mp[B4149]*. During early embryogenesis, *MP* is expressed in the inner cells and lower protoderm of the proembryo along with another gene activating *ARF*, *AFR6* [85]. By comparing auxin output in the wild type and *mp* mutant embryo from the developmental stages after the first expression of *MP*, the direct impact to auxin output from losing a single *ARF* while the presence of other *ARFs* remained unaffected can be validated.

In addition to validating our hypothesis of differential capacity of auxin response, we also asked how missing a single *ARF* whose expression is limited to the subepidermal and later vascular cells during embryogenesis, impacts auxin response in the whole embryo[65]. Auxin outputs during embryogenesis, in wild type and various mutants including *mp*, has been described through *DR5* driving GFP[8, 10, 86] or GUS[87-89]. These descriptions, however, either lacks cellular resolution or focused on developmental stages after globular stage due to difficulties with detecting *DR5* in embryos.

In the wild type embryo at early globular stage before hypophysis division (Fig. 5a), auxin output was highest in the topmost suspensor cell (the hypophysis), and the subtending suspensor cell, while it is lower in vascular and ground tissue cells. Auxin output later increased in vascular cells (Fig. 5k) and upper protoderm (Fig. 5b), from which future cotyledons developed. After hypophysis division (Fig. 5l), auxin maxima remained in both daughter cells of the hypophysis, and high auxin output remained in cotyledon initials while it decreased in vascular cells until the heart stage. At transition and heart stage (Fig. 5c) auxin maxima remained in the QC and columella cells with lower auxin output in vascular cells. In the upper domain of the embryo, auxin output
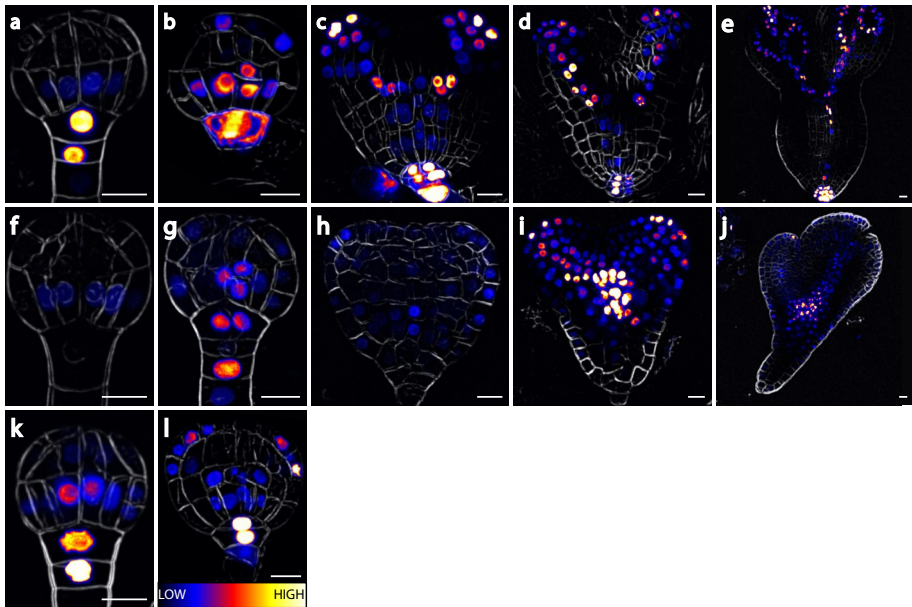
Figure 5. *DR5v2* marks abnormal auxin output in mp mutant embryos

Auxin output in wild type (a-e, k, l) and mp mutant (f-j) embryo. Early globular stage (a, f); late early globular stage (k); mid globular stage (b, g); late globular stage (l); early heart stage (c, h); late heart stage (d, i); torpedo stage (e, j). Note the reduced and lost auxin output in lower embryo and unrestricted auxin output in upper embryo in mp mutant. Maximum projection of 3 optical sections (1 µm interval) in middle plane. Scale bar= 10.0 µm.

increased in the developing vasculature and cotyledons with auxin maxima in tips of cotyledons. This auxin output pattern was then maintained through late torpedo stage (Fig. 5c-e) at which vascular branching occurs. At late torpedo stage (Fig. 5e), though auxin output pattern remained unchanged in lower domain of the embryo, auxin output maxima in cotyledons became restricted to the far most vascular cells, a few cells in epidermis and ground tissue connecting to vasculature, and new vasculature initials.

The *mp* mutant is difficult to distinguish from the wild type until the hypophysis divides. However, we did occasionally (10%; n=41 embryos) find loss of auxin output in the hypophysis of embryos in progeny of *mp* hetetozygotes (Fig. 5f). After hypophysis division (Fig. 5g), effects on auxin output caused by loss of *MP* became consistent among mutant embryos that are morphologically different from their wild type siblings with

mis-orientated division plane. Auxin output in the *mp* embryo, though still highest in daughter cells of hypophysis and high in inner cells, were strongly reduced compared to wild type. Thus, *DR5v2* reports the predicted reduction in auxin response in *mp* mutant embryos, but also showed that there is residual response in mutant embryos. In addition to reduced auxin output, ectopic low auxin output could be found in the entire embryo while high auxin output is never established in the upper protoderm. At early heart stage (Fig. 5h), restricted auxin output was completely lost, and only ectopic weak auxin output remained in the embryo with mild auxin output in presumptive cotyledon initials and vasculature. At late heart stage (Fig. 5i), auxin output in lower embryo was completely lost and never recovered, while auxin maxima in cotyledon tips and high auxin input in presumptive upper vascular cells were re-established, though less restricted compared to wild type. In addition to unrestricted auxin output throughout the upper embryo including the shoot apical meristem, an ectopic auxin maximum is established in presumptive vascular cells underneath the shoot apical meristem. At late torpedo stage (Fig. 5j), in contrast, auxin output remained absent in lower embryo, and ectopic auxin output maximum remained in the center of the embryo. In the cotyledons, instead of restricted high auxin output in vasculature and epidermal and ground tissue cells connecting to vasculature in wild type, low auxin output was unrestrained in cells surrounding supposed vasculature and epidermal and ground tissue cells in *mp* mutant embryo.

Thus, *DR5v2* expression analysis confirms a strong reduction in auxin transcriptional output in the *mp* mutant, and in addition shows that *MP* is required for focusing auxin response to a narrow domain in the embryo apex, including the vascular strands of cotyledons.

Discussion

The generically expressed R2D2-U allows monitoring auxin perception in most tissues with comparable resolution, sensitivity, and responsiveness comparable to its dividing-cell-specific predecessor, R2D2-R, and the triple cassette C3PO-R proved to be a comprehensive tool to monitor both auxin perception and positive auxin transcriptional response simultaneously. With these new tools, we did not only observed auxin input and output maxima in the root apex that were only predicted through computational simulation, but also provide experimental data that support our hypothesis of differential auxin signaling capacity between different tissues and developmental stages. In addition, the comparison of auxin response between wild type and *mp* mutant embryos through their development, we provided an update for auxin response during embryogenesis with more sensitive *DR5v2* and demonstrated the impact of losing single locally expressed auxin response factor to the global auxin response during embryogenesis.

A set of novel auxin response reporters

The broad expression of R2D2-U and ability of C3PO-R to simultaneously marking auxin input and output offer generic analysis to further dissect finer auxin signaling *in vivo*. Though most auxin input and output marked by R2D2-U and C3PO-R are consistent with known auxin output pattern from *DR5*, some seemed controversial at first glance.

Firstly, R2D2-U and C3PO-R detected high auxin input and output in trichoblasts while only low auxin input and no output were observed in atrichoblasts. This observation seemed to suggested higher auxin concentration in trichoblasts than atrichoblasts and contradicted to the assumption that atrichoblasts uptake more auxin supported by atrichoblast-specific AUX1 expression and higher *DR5* activity observed in atrichoblast after exogenous auxin (1-Naphthaleneacetic acid, NAA) treatment[25, 90]. However, the effect of auxin signaling on root hair growth occurs in trichoblasts[91, 92] and the high expression of auxin transport and transport-regulating genes in trichoblasts[93] suggests sufficient auxin input in trichoblasts to trigger auxin signaling and transport. Since atrichoblasts likely have more efficient auxin uptake than trichoblasts[21, 25], an additional auxin transport mechanism in atrichoblasts cannot yet be excluded. In addition, we cannot emphasize more that auxin input represented by R2D2 should not be interpreted as cellular auxin concentration, but as an amplitude to auxin perceived by cells to trigger downstream auxin response, and hence that auxin concentrations in trichoblasts and atrichoblasts remain to be determined.

Secondly, we found non-overlapping auxin input and output maxima in trichoblasts and atrichoblasts. Given that *DR5v2* is inactive in the absence of auxin, only gene activation results from binding of positive regulating *ARF*s can be shown. Only five (*ARF5, -6, -7, -8,* and *-19*) out of 23 *ARFs* in the *Arabidopsis* genome were predicted to

be gene activators and this ability has been experimentally demonstrated mostly in cell-based transient assays[40, 63, 66, 94]. Taken at face value, *DR5*-like reporters are thus only able to report on a small subset of the ARFs. Of these five *ARFs*, *MP* and *ARF6* are not expressed in the root epidermis and *ARF8* is lowly expression in epidermis. Only *ARF7* and *-19* are highly expressed in epidermis from late elongation zone with three times higher expression in trichoblasts than in atrichoblasts[93]. Therefore, until late elongation zone, due to the lack of predicted gene activating *ARFs*, *DR5v2* cannot be activated disregarding the auxin input and auxin response. The same principle can also explain our observation that similar auxin input levels can be detected in both protoxylem and procambium cells while only the former show high auxin output; *ARF5, -7, -19* are expressed in protoxylem while only *ARF8* is expressed in procambium[93].

Our results demonstrate the ability of R2D2-U and C3PO-R to reveal auxin input and output not only known and hypothesized maxima, but also more subtle readouts. *In vivo*, dynamic and simultaneous comparison between auxin input and output within single cell or local cells eliminates any minor physiological variations between individual cells or plants. These properties allow readout of auxin input and output to support one another and offer a possibility to explore auxin signal dynamics with unicellular resolution. However, they also reveal the complexity of auxin signaling and the precautions required for data interpretation.

Limitations to using novel auxin reporters

To overcome the limitations of the local meristem-specific expression of the *RPS5A* promoter, we generated a novel R2D2 using the *UBI10* promoter. While this reporter was useful in reporting novel auxin input sites, it also showed developmental phenotypes. The dwarfism phenotype is only observed in R2D2-U homozygotes, which means that heterozygous lines can be used, be it with caution. Similar dwarf phenotypes are also observed in auxin perception mutants, such as overexpression of wild type *Aux/IAA*[95], degradation-resistant *Aux/IAA*s mutant[96, 97],and auxin-conjugating enzyme *GH3*[72, 98].This suggests that ubiquitous high expression of the DII degron in R2D2-U homozygotes may serve as a competitive inhibitor of *SCF(TIR1/AFB1-3)*, thus interfering with normal auxin perception. This defect must be related to the site of expression, because R2D2-R and C3PO-R homozygotes do not show this aberrant phenotype despite levels of expression in meristem cells that are at least comparable to that seen in R2D2-U lines. Since both R2D2-R[45] and R2D2-U can respond to lower concentration of exogenous IAA treatment in root apical meristem than other tested developmental stages, it seems unlikely that root meristem cells have *Aux/IAA*s expression levels that are so high that they would outcompete the DII degron.

This suggests higher *SCF(TIR1/AFB1-3)* degradation capacity in cell division foci than in differentiated tissues. This assumption is consistent with the gradually reduced expression of all *TIR1/AFB* F-box proteins from the meristem towards differentiated cells[43, 93] and is further supported by our observation that root cap show a lack of auxin input, despite the constantly observed high auxin output [7, 12, 14]. The only expressed auxin perception F-box protein that shows detectable expression in root cap cells is *AFB2* [43, 93]. This would lead to low *SCF(TIR1/AFB1-3)* degradation capacity and auxin perception capacity and likely attenuates the downstream auxin signaling.

Factors like the speed of auxin uptake, expression pattern of *Aux/IAA*s, and *SCF(TIR1/AFB1-3)* ubiquitin ligase complex activity can all influence auxin perception capacity of each individual cell. Our results from R2D2-U and C3PO-R provide sound evidence supporting this hypothesis and suggest, at least in roots, differential auxin perception capacity exist between tissues and cells within tissue but with different developmental stages.

Auxin response in the embryo

While reduced auxin output in *mp* embryo mutant is expected due to losing a major *ARF*, the observed impact on auxin output is greater than expected. In early globular stage, though the reduced auxin output in lower-subepidermal cells can be explained by the lost of *MP* [65], the ectopic auxin output in protoderm and upper tier cells could be due to unspecific auxin distribution in the embryo by reduced expression of auxin efflux carrier *PIN1* and loss of auxin influx carrier *AUX1* and *LAX2* in the inner lower cells in *mp* embryo[24, 66].

From early heart stage onward, the impact of *mp* mutant increases due to *MP*'s specific expression in vasculature, cells under shoot apical meristem, and epidermis[65, 66]. However, while *mp* mutant embryos have only reduced and unrestricted auxin output without maxima in early heart stage, auxin output in the upper half of the embryo is restored with auxin maxima in cotyledon tips and vascular cells under shoot apical meristem and supposed vasculature in mid heart stage. This suggests that in addition to *MP*, there must be (an)other *ARF(s)* responsible for cotyledon and vasculature development in mid heart stage. *ARF7* is active in the cotyledon in heart stage, and its function partially overlaps with *MP* in cotyledon development[94]. However, the excessive auxin output maximum in vascular cells under the shoot apical meristem cannot be explained only by the normal expression pattern of *ARF7*. One possibility is the accumulation of auxin from shoot apical meristem and cotyledon. Though the exact effect of *ARF7* and other genes activated in heart stage in *mp* mutant embryo on auxin distribution is unknown, it is likely that auxin distribution

at the upper embryo and the cotyledons is recovered enough to re-establish auxin output maxima in cotyledon tips and supposed vasculature. However, due to the loss of auxin transporters *PIN1* and *LAX2* in the *mp* embryo, excessive auxin cannot be transported to the lower embryo and is accumulated in these cells under shoot apical meristem.

Our results have not only verified the capability of *DR5v2* to monitor altered auxin responses in auxin signaling mutant, but also proved the value of how visualization of given biological process can significantly facilitate dissecting mechanism of such process. With all advance on auxin signaling reporters, impact of auxin signaling on plant development can now be easily visualized and evaluated. The mechanisms for processes between auxin signaling and subcellular response during morphogenesis, however, still remain elucidated due to limited toolset and experimental methods.

Materials and Methods

Plant material and growth condition

All primers used in this study are listed in Table. 2. R2D2-U in *pGIIM/pUBQ10::mDII:ntdTomato-pUBQ10::DII:n3Venus* was generated via replacing *pRPS5A* in R2D2-R, *pGIIM/pRPS5A::mDII:ntdTomato-pRPS5A::DII:n3Venus*, with *pUBQ10*. To engineer *pRPS5A::DII* and *pRRPS5A::mDII* reporter cassettes, *pRPS5A::DII* and *pRRPS5A::mDII* reporter cassettes were amplified from genomic DNA of *pRPS5a::DII:Venus* and *pRPS5a::mDII:Venus* reporter lines using primer set "pRPS5a::DII/mDII" then cloned into pPLV08 via ligation-independent cloning as described[45] to generate two plasmids, "*pGIIK/pRPS5a::DII:sCFP*" and "*pGIIK/pPS5a::mDII:sCFP*." *pRPS5A* in "*pGIIK/pRPS5a::DII:sCFP*" and "*pGIIK/pPS5a::mDII:sCFP*" were removed via Acc65I digestion and replaced by *pUBQ10*, which was amplified from WAVE002[99] using primer set "pUBQ10", followed by *Acc65I* digestion, via conventional cloning to generate two plasmids, "*pGIIK/pUBQ10::DII:sCFP*" and "*pGIIK/pUBQ10::mDII:sCFP*." To generate R2D2-U, *pUBQ10::DII* and *pUBQ10::mDII* reporter cassettes amplified from "*pGIIK/pUBQ10::DII:sCFP*" and "*pGIIK/pUBQ10::mDII:sCFP*" using primer sets "pUBQ10::DII" and "pUBQ10::mDII" were sequentially cloned into *pGIIM/LIC_ SwaI-ntdTomato- LIC_HpaI-n3Venus* as described[45].

Table. 2 Primers used in this study

PSirimer set	Forward	Reverse
pRPS5a::DII/mDII	TAGTTGGAATGGGTTCGG GCCATAATCGTGAGTAGA	TTATGGAGTTGGGTTCCTC TCCGGGATGATCTCACCG
pUBQ10	TTTGGTACCAGTCTAGCT CAACAGAGCTTT	TTTGGTACCGGTATTGTT TTATAGAAGAAG
pUBQ10::DII	TAGTTGGAATAGGGTTCCC AGTCTAGCTCAACAGAGC	AGTATGGAGTTGGGTTCTC TCCGGGATGATCTCACCG
pUBQ10::mDII	TAGTTGGAATAGGATTTCC CAGTCTAGCTCAACAGAGC	AGTATGGAGTTGGATTTCCC TCTCCGGGATGATCTCACCG
mTurqoise2+ STOP	TTTTGGATCCGGTGGTATG GTGAGCAAGGGCGAGGA	TTTTAGATCTTTACTTG TACAGCTCGTCCATGC
mTurqoise2 non-STOP	TTTTGGATCCGGTGGTATG GTGAGCAAGGGCGAGGA	TTTTAGATCTCTTGTA CAGCTCGTCCATGCC
NLS-mTurqoise non-STOP	TTTTGGATCCCATGGCTC CAAAGAAGAAGAGAAAG GTCATGGTGAGCAAGGG CGAGGA	TTTTAGATCTCTTGTA CAGCTCGTCCATGCC
Additional AscI	CTAGATTAATTAAGACAC AGGCGCGCCT	CTAGAGGCGCGCC TGTGTCTTAATTAAT

C3PO-R in *pGIIM/DR5v2::n3mTurqoise2-pRPS5A::mDII:ntdTomato-pRPS5A::DII:n3Venus* was generated via inserting DR5v2::n3mTurqoise2 into R2D2-R. To generate *n3mTurqoise2*, a triple mTurqoise2 N-terminally fused with nucleus localization signal (NLS), three components: an mTurqoise2 coding sequence (CDS) with a stop codon, an mTurqiose2 CDS without stop codon, and an NLS: mTurqoise2 without stop codon, was generated via PCR from plasmid template "pmTurqoise2-C1[100]" using primer sets, "mTurqoise2+ STOP", "mTurqoise2 non-STOP", and "NLS-mTurqoise non-STOP" were sequentially cloned into *pGIIK/LIC_SwaI-LIC_HpaIv2-tNOS* as described for generating NLS:3xEGFP[101]. The *n3mTurqoise2-tNOS* cassette was then excised via *BamHI-XbaI* double-digestion and inserted into *pGIIK/DR5v2::ntdTomato-tNOS*, whose *ntdTomato-tNOS* cassette had been removed via *BamHI-XbaI* double-digestion in advance, via conventional cloning to generate *pGIIK/DR5v2::n3mTurqoise2-tNOS*. An *AscI* restriction site from oligo dimer "Additional AscI" was inserted into *XbaI* digested *pGIIK/DR5v2::n3mTurqoise2-tNOS* via conventional cloning before ligating DR5v2::n3mTurqoise2-tNOS excised by *Bsp120I-AscI* double-digestion with *Bsp120I-AscI* double-digested *pGIIM/pRPS5A::mDII:ntdTomato-pRPS5A::DII:n3Venus* to generate *pGIIM/DR5v2::n3mTurqoise2-pRPS5A::mDII:ntdTomato-pRPS5A::DII:n3Venus*.

All transgenic lines were generated in wild type *Arabidopsis* thaliana Col-0 ecotype via floral dip[102] and selected using Methothrexate as described[45]. *Arabidopsis* plants were grown at 22 °C in 16 h/8 h light/dark cycles for every experiment. All seeds were surface sterilized, sown on half-strength Murashige and Skoog medium with 0.8% Daichin agar (Duchefa) (1/2 MS plate) and vernalized at 4 °C for 2 d. For microscopic analysis of root, seedlings were grown vertically for 5 d after transfer to growth chamber; this period was decreased to 3 or 4 d for microscopic analysis in shoot.

Microscopic analysis

Images were acquired in 8-bit format using a Leica TCS SP5II confocal laser scanning microscope with 20× numerical aperture (NA) = 0.75 and 63× NA = 1.20 water-immersion objective. mTurqoise2 and Venus were excited by Argon-ion laser, tdTomato, propidium iodide, and Renaissance 2200 were excited using a diode laser, and their emissions were detected sequentially with Leica HyD in photon counting mode for quantification and comparison between channels. Excitation and detection of fluorophores were configured as follows: mTurqoise2 was excited at 458 nm and detected at 468–495 nm; Venus was excited at 514 nm and detected at 524–540 nm; tdTomato was excited at 561 nm and detected at 571–630 nm; propidium iodide was excited at 561 nm and detected at 571–700 nm; Renaissance 2200 was excited at 405 nm and detected at 430–470 nm. The pinhole was set to 2.0 Airy Unit, and the virtual ratio images between channels were generated as described[45].

For live imaging of roots treated by auxin, 20x objective were used along with 2 Airy Unit for pinhole size, and the slides were prepared as described[45]. Demineralized water was used as mounting media, 0.01% dimethyl sulfoxide (DMSO) dissolved in demineralized water and given concentrations of IAA (Duchefa) dissolved in 0.01% DMSO was used as mock and treatment solutions, respectively.

Acknowledgements

References

1. Vanneste, S. & Friml, J. *Cell* **136**, 1005-1016 (2009).
2. Berleth, T. *J. Plant Growth Regul.* **20**, 14-21 (2001).
3. De Rybel, B., Mahonen, A.P., Helariutta, Y. & Weijers, D. *Nat. Rev. Mol. Cell Biol.* **17**, 30-40 (2016).
4. Smit, M.E. & Weijers, D. *Curr. Opin. Plant Biol.* **28**, 99-105 (2015).
5. Morris, D.A. & Thomas, A.G. *J. Exp. Bot.* **29**, 147-157 (1978).
6. Forestan, C. & Varotto, S. in Methods in Molecular Biology, Vol. 959 223-233 (Humana Press Inc., 2013).
7. Petersson, S.V. et al. *Plant Cell* **21**, 1659-1668 (2009).
8. Benkova, E. et al. *Cell* **115**, 591-602 (2003).
9. Friml, J. et al. *Cell* **108**, 661-673 (2002).
10. Friml, J. et al. *Nature* **426**, 147-153 (2003).
11. Friml, J., Wisniewska, J., Benkova, E., Mendgen, K. & Palme, K. *Nature* **415**, 806-809 (2002).
12. Blilou, I. et al. *Nature* **433**, 39-44 (2005).
13. Bilsborough, G.D. et al. *Proc Natl Acad Sci U S A* **108**, 3424-3429 (2011).
14. Grieneisen, V.A., Xu, J., Maree, A.F.M., Hogeweg, P. & Scheres, B. *Nature* **449**, 1008-1013 (2007).
15. Péret, B. et al. *Nat. Cell Biol.* **14**, 991-998 (2012).
16. Petrasek, J. & Friml, J. *Development* **136**, 2675-2688 (2009).
17. Scarpella, E., Marcos, D., Friml, J. & Berleth, T. *Genes Dev.* **20**, 1015-1027 (2006).
18. Marcos, D. & Berleth, T. in Methods in Molecular Biology, Vol. 495 11-20 (2009).
19. Petrasek, J. et al. *Science* **312**, 914-918 (2006).
20. Wisniewska, J. et al. *Science* **312**, 883 (2006).
21. Band, L.R. et al. *Plant Cell* **26**, 862-875 (2014).
22. Swarup, K. et al. *Nat. Cell Biol.* **10**, 946-954 (2008).
23. Marchant, A. et al. *Plant Cell* **14**, 589-597 (2002).
24. Robert, H.S. et al. *Development* **142**, 702-711 (2015).
25. Jones, A.R. et al. *Nat. Cell Biol.* **11**, 78-84 (2009).
26. Abas, L. et al. *Nat. Cell Biol.* **8**, 249-256 (2006).
27. Heisler, M.G. et al. *Curr. Biol.* **15**, 1899-1911 (2005).
28. De Reuille, P.B. et al. *Proceedings of the National Academy of Sciences of the United States of America* **103**, 1627-1632 (2006).
29. Dharmasiri, N., Dharmasiri, S. & Estelle, M. *Nature* **435**, 441-445 (2005).
30. Kepinski, S. & Leyser, O. *Nature* **435**, 446-451 (2005).
31. Dharmasiri, N. et al. *Dev. Cell* **9**, 109-119 (2005).
32. Gray, W.M., Kepinski, S., Rouse, D., Leyser, O. & Estelle, M. *Nature* **414**, 271-276 (2001).
33. Tan, X. et al. *Nature* **446**, 640-645 (2007).

34. Remington, D.L., Vision, T.J., Guilfoyle, T.J. & Reed, J.W. *Plant Physiol.* **135**, 1738-1752 (2004).
35. Szemenyei, H., Hannon, M. & Long, J.A. *Science* **319**, 1384-1386 (2008).
36. Tiwari, S.B., Wang, X.J., Hagen, G. & Guilfoyle, T.J. *Plant Cell* **13**, 2809-2822 (2001).
37. Kepinski, S. & Leyser, O. *Proc Natl Acad Sci U S A* **101**, 12381-12386 (2004).
38. Ramos, J.A., Zenser, N., Leyser, O. & Callis, J. *Plant Cell* **13**, 2349-2360 (2001).
39. Zenser, N., Ellsmore, A., Leasure, C. & Callis, J. *Proc Natl Acad Sci U S A* **98**, 11795-11800 (2001).
40. Tiwari, S.B., Hagen, G. & Guilfoyle, T. *Plant Cell* **15**, 533-543 (2003).
41. Kim, J., Harter, K. & Theologis, A. *Proceedings of the National Academy of Sciences of the United States of America* **94**, 11786-11791 (1997).
42. Wang, R. & Estelle, M. *Curr. Opin. Plant Biol.* **21**, 51-58 (2014).
43. Brunoud, G. et al. *Nature* **482**, 103-U132 (2012).
44. Vernoux, T. et al. *Mol. Syst. Biol.* **7** (2011).
45. Liao, C.Y. et al. *Nat. Methods* **12**, 207-210, 202 p following 210 (2015).
46. Bierfreund, N.M., Reski, R. & Decker, E.L. *Plant Cell Rep.* **21**, 1143-1152 (2003).
47. Fujita, T. et al. *Evol. Dev.* **10**, 176-186 (2008).
48. Pacios-Bras, C. et al. *Plant Mol. Biol.* **52**, 1169-1180 (2003).
49. Sakakibara, K. et al. *Development* **130**, 4835-4846 (2003).
50. Yi, L., Wu, Y.H., Hagen, G. & Guilfoyle, T. *Plant and Cell Physiology* **40**, 675-682 (1999).
51. Swarup, R. et al. *Nat. Cell Biol.* **7**, 1057-1065 (2005).
52. Swarup, R. et al. *Plant Cell* **19**, 2186-2196 (2007).
53. Bishopp, A. et al. *Curr. Biol.* **21**, 917-926 (2011).
54. Swarup, R. et al. *Genes Dev.* **15**, 2648-2653 (2001).
55. Ulmasov, T., Liu, Z.-B., Hagen, G. & Guilfoyle, T.J. *Plant Cell* **7**, 1611-1623 (1995).
56. Bhatia, N. et al. *Curr. Biol.* **26**, 3202-3208 (2016).
57. Figueiredo, D.D., Batista, R.A., Roszak, P.J., Hennig, L. & Kohler, C. *Elife* **5** (2016).
58. Figueiredo, D.D., Batista, R.A., Roszak, P.J. & Kohler, C. *Nat Plants* **1**, 15184 (2015).
59. Moller, B.K. et al. *Proc Natl Acad Sci U S A* **114**, E2533-E2539 (2017).
60. Roodbarkelari, F., Du, F., Truernit, E. & Laux, T. *BMC Biol.* **13** (2015).
61. Xuan, W. et al. *Science* **351**, 384-387 (2016).
62. Berleth, T. & Jurgens, G. *Development* **118**, 575-587 (1993).
63. Ulmasov, T., Hagen, G. & Guilfoyle, T.J. *Proc Natl Acad Sci U S A* **96**, 5844-5849 (1999).
64. Boer, D.R. et al. *Cell* **156**, 577-589 (2014).

65. Hamann, T., Benkova, E., Baurle, I., Kientz, M. & Jurgens, G. *Genes Dev.* **16**, 1610-1615 (2002).
66. Schlereth, A. et al. *Nature* **464**, 913-916 (2010).
67. Weijers, D. et al. *Dev. Cell* **10**, 265-270 (2006).
68. Weijers, D. et al. *EMBO J.* **24**, 1874-1885 (2005).
69. Weijers, D. et al. *Development* **128**, 4289-4299 (2001).
70. Gray, W.M., Östin, A., Sandberg, G., Romano, C.P. & Estelle, M. *Proceedings of the National Academy of Sciences of the United States of America* **95**, 7197-7202 (1998).
71. Casimiro, I. et al. *Plant Cell* **13**, 843-852 (2001).
72. Park, J.E. et al. *J. Biol. Chem.* **282**, 10036-10046 (2007).
73. Lee, R.D.W. & Cho, H.T. *Frontiers in Plant Science* **4** (2013).
74. Rigas, S. et al. *New Phytol.* **197**, 1130-1141 (2013).
75. Zadnikova, P. et al. *Development* **137**, 607-617 (2010).
76. Norris, S.R., Meyer, S.E. & Callis, J. *Plant Mol. Biol.* **21**, 895-906 (1993).
77. Sun, C.W. & Callis, J. *Plant J.* **11**, 1017-1027 (1997).
78. Sabatini, S. et al. *Cell* **99**, 463-472 (1999).
79. Pitts, R.J., Cernac, A. & Estelle, M. *Plant J.* **16**, 553-560 (1998).
80. Péret, B., Larrieu, A. & Bennett, M.J. *J. Exp. Bot.* **60**, 3637-3643 (2009).
81. De Smet, I. et al. *Development* **134**, 681-690 (2007).
82. Kircher, S. & Schopfer, P. *J. Exp. Bot.* **67**, 1411-1420 (2016).
83. Moreno-Risueno, M.A. et al. *Science* **329**, 1306-1311 (2010).
84. Xuan, W. et al. *Curr. Biol.* **25**, 1381-1388 (2015).
85. Rademacher, E.H. et al. *Plant J.* **68**, 597-606 (2011).
86. Robert, H.S. et al. *Curr. Biol.* **23**, 2506-2512 (2013).
87. Ni, D.A., Wang, L.J., Ding, C.H. & Xu, Z.H. *Cell Res.* **11**, 273-278 (2001).
88. Grunewald, W. et al. *EMBO Reports* **14**, 1136-1142 (2013).
89. Weijers, D., Van Hamburg, J.P., Van Rijn, E., Hooykaas, P.J. & Offringa, R. *Plant Physiol.* **133**, 1882-1892 (2003).
90. De Rybel, B. et al. *Nat. Chem. Biol.* **8**, 798-805 (2012).
91. Cho, M., Sang, H.L. & Cho, H.T. *Plant Cell* **19**, 3930-3943 (2007).
92. Knox, K., Grierson, C.S. & Leyser, O. *Development* **130**, 5769-5777 (2003).
93. Brady, S.M. et al. *Science* **318**, 801-806 (2007).
94. Hardtke, C.S. et al. *Development* **131**, 1089-1100 (2004).
95. Yan, D.W. et al. *PLoS ONE* **8** (2013).
96. Ku, S.J., Park, J.Y., Ha, S.B. & Kim, J. *J. Plant Physiol.* **166**, 548-553 (2009).
97. Muto, H., Watahiki, M.K., Nakamoto, D., Kinjo, M. & Yamamoto, K.T. *Plant Physiol.* **144**, 187-196 (2007).

98.   Westfall, C.S. et al. *Proceedings of the National Academy of Sciences of the United States of America* **113**, 13917-13922 (2016).
99.   Geldner, N. et al. *Plant J.* **59**, 169-178 (2009).
100. Goedhart, J. et al. *Nature Communications* **3** (2012).
101. Takada, S. & Jürgens, G. *Development* **134**, 1141-1150 (2007).
102. Davis, A.M., Hall, A., Millar, A.J., Darrah, C. & Davis, S.J. *Plant Methods* **5** (2009).

Chapter 4

A TOOLKIT FOR STUDYING CELLULAR REORGANIZATION DURING EARLY *ARABIDOPSIS THALIANA* EMBRYOGENESIS

Che-Yang Liao and Dolf Weijers

Laboratory of Biochemistry, Wageningen University, Wageningen, the Netherlands

Abstract

Considerable progress had been made to understand the influence of physical and genetic factors on the patterns of cell division in various model systems. However, how each of these factors direct changes in subcellular structures has remained unclear. Generic machineries for the execution of cell expansion and division have been characterized, but how these are influenced by genetic regulators and physical cell properties remains an open question. To a large degree, the complexity of growing post-embryonic tissues, and the lack of precise predictability have prevented the extraction of rigid correlations between subcellular structures and future cell division orientation. The *Arabidopsis* embryo offers an exquisitely predictable and simple model for studying such correlations, but so far the tools and methodology to study subcellular structures in the early embryo were lacking. Here, we describe a set of markers to visualize a range of subcellular structures in the early *Arabidopsis* embryo. We have designed a series of fluorescent cellular reporters optimized for embryos, and demonstrate the effectiveness of using these "ACE" reporters with simple 3D imaging procedures that preserve delicate cellular structures. We describe ontogeny of subcellular structures in the early embryo, and found that central/peripheral cell polarity is established much earlier than suspected. In addition, we show that the Actin and microtubule cytoskeleton have distinct topologies in the embryo. These tools and methods will allow detailed analysis of the cellular reorganization events underlying morphogenesis in the *Arabidopsis* embryo.

Introduction

Morphogenesis in multicellular organisms depends on individual cells' decisions on the direction in which growth or division occurs. Particularly in plants, where rigid cell walls prevent cell migration, pre-mitotic control of cell division orientation is a crucial contributor to organized three-dimensional development [1]. A key question in plant developmental biology, therefore, is how the decision of individual cells on the direction in which to divide is regulated. It has been established that three major factors drive cell division orientation: Firstly, the initial geometry of a cell biases the preferred orientation of cell division [2]. Secondly, tissue-scale stresses influence cell division orientation [3, 4] and thirdly, genetic factors can drive defined orientations of cells divisions such that cell division orientation is an output of developmental regulations [5, 6]. Whatever triggers the oriented cell division; the input signal must be translated to cellular re-organization to facilitate re-orientation of division plane. A key challenge therefore is to identify the cellular components that are being modulated by regulatory input to effect cell division orientation.

From various different model systems, it is clear that there is a core cell division machinery that executes pre-mitotic orientation cues [7, 8]. This core mechanism – the mitotic and cytokinetic machinery – forms a spindle perpendicular to the pre-prophase band to segregate chromosomes. Following chromosome segregation, the midline of the spindle is targeted by Golgi-derived vesicles along microtubule and actin filaments, thus forming a phragmoplast to build a cell plate between the newly divided nuclei [9].

Thus, three key cytoskeletal indicators of oriented cell division are the pre-prophase band whose position and orientation forecast the phragmoplast[10, 11]; cortical actin and actin cables anchoring the spindles during mitosis and later daughter nuclei during cytokinesis [12, 13]; and phragmoplast that determines the physical division plane [14]. These cytoskeletal structures follow both microtubule and actin cytoskeleton that are important for determining division plane [15]. Indeed there is ample evidence for the involvement of these structures in different contexts [7]. How the cytoskeleton is manipulated to modify orientation of division, however, is not well understood.

Essentially all organelles and cellular structures are coordinately orchestrated to allow cell division [9, 16]. Thus, each of these, especially the vacuole [17] and the nucleus [18], can either facilitate or constrain choices for cell division orientation. The roles these structures play in oriented cell division have remained largely unexplored. In addition to subcellular structures that mediate cell division execution, the perception of cellular coordinates relative to the body/tissue axis could serve as a reference for protein polar transport/localization and determination of cell division orientation. How polarity information is established and integrated into the division plane is also far from clear.

Analysis of contributions of any cellular structure to oriented cell division requires that cellular morphology is relatively simple and/or predictable. Alternatively, structures should be followed over time in order to draw correlations between changes in these structures and future cell division orientation. Thus far, most analysis of oriented cell division has been performed in meristematic tissues of generally complex topologies with limited predictability [1]. Here we use the early *Arabidopsis* embryo as a model for oriented cell division. During the first rounds of cell division, a highly regular pattern of cells emerges, from which the precursors of all seedling tissues and organs are formed [19]. From earlier 3D analysis, it has become clear that some cell divisions are symmetric, following only the geometry of the cell, while others are highly asymmetric, following tight genetic control to deviate from a default, symmetric division [20]. In this system, cell division orientation choice is influenced by the plant hormone auxin, whose activity favors asymmetric division [20]. While an excellent model system for studying symmetric and asymmetric division, as well as switches in cell division orientations, a key open question is which cellular structures are subject to auxin-dependent regulation. Thus far, it has however been impossible to address this question, as little if any tools were available to visualize subcellular structures in early embryos.

Here, we have generated the tools required to answer this important question, and to study cellular (re)organization in early *Arabidopsis* embryos.

Results

A set of fluorescent cellular markers for embryogenesis

To develop a panel of markers for subcellular structures in the *Arabidopsis* embryo, we first selected a set of established reporters (Supplementary Table 1) that includes: (1) uniformly distributed plasma membrane proteins for highlighting cell contours [21, 22]; (2) plasmodesmata-specific proteins for evaluating connectivity between cells [23]; (3) organelle-specific proteins labeling endosome, trans-Golgi network, or tonoplast [21]; (4) nuclear pore markers [24]; (5) cytoskeleton markers labeling either F-actin [25, 26] or tubulin [27]. In addition to the dynamics of cellular components, to evaluate the establishment of polarity, which could provide spatial information to the cell, we also include (6) a set of polar localized proteins labeling the apical [28], basal [29], central [30] or peripheral [30] plasma membrane in post-embryonic tissues. To achieve embryo-specific expression of reporters, each was expressed from the embryo-specific *Arabidopsis WOX2* promoter [31], as well as from the meristematic *Arabidopsis RPS5A* promoter [32]. These markers were named ACE (*Arabidopsis Cellular markers for Embryogenesis*; Supplementary Table 1). Though ACE driven by *pRPS5A* (ACE-R) were uniformly expressed in the complete embryo, *pRPS5A*'s high activity in the endosperm and maternal tissues made imaging difficult, as fluorescence intensity was very high in cells surrounding embryos in embryo preparations (Fig. 1a). In contrast, *pWOX2*-driven ACE markers (ACE-W) were specifically expressed in the pro-embryo, two uppermost suspensor cells, and the chalaza from 2-cell to early globular stage with higher expression level compared to ACE-R (Fig. 1b-i). After early globular stage, activity of *pWOX2* started to decrease in the basal part of the embryo and two topmost cells in the suspensor (Fig. 1h). These properties made ACE-R more suitable for dissecting cell biology in suspensor, embryo proper after early globular stage, and seed development while ACE-W were more suitable for dissecting cell biology in early embryo proper and thus used here unless mentioned otherwise.

Optimizing preservation of delicate cellular structures

Upon examining the expression of ACE-W lines in the embryos with common microscopy procedures [33, 34], we found that particularly lines that mark delicate cellular structures did not show expected patterns. Microtubule and actin architectures were either fragmentary or completely depolymerized with reporter protein only in the cytosol (Fig. 2a,b). Intact microtubule and actin architectures could be observed in corresponding ACE-R root apical meristem (Supplementary Fig. 1) suggesting that the markers' capacities to label each component were not compromised. Given that a structured cytoskeleton must exist in embryos, we conclude that a different procedure is required to preserve such structures.
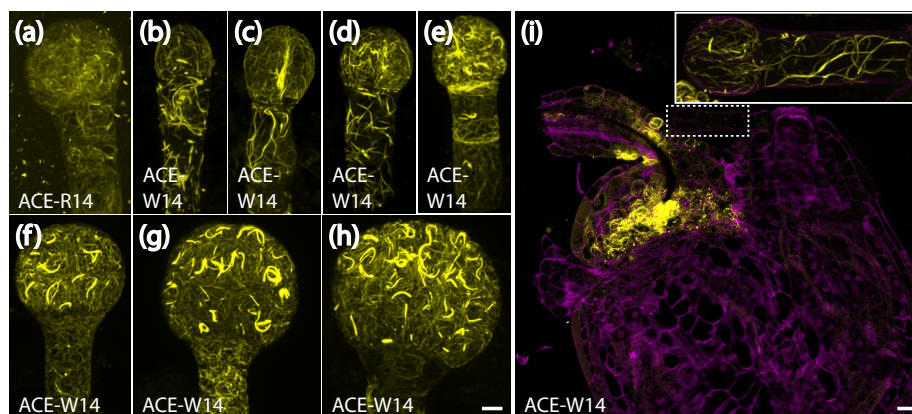
Fig. 1. Expression of ACE-R and ACE-W during embryogenesis
(a) Maximum intensity projection of actin filaments labeled by ACE-R14 (Lifeact: tdTomato) in 16-cell embryo. (b-h) Maximum intensity projections of actin filaments labeled by ACE-W14 (Lifeact: tdTomato) in 1-cell (b), 2-cell (c), 4-cell (d), 8-cell (e), 16-cell (f), early-globular (g), and late-globular (h) embryos. (i) Overview of ACE-W14 (Lifeact: tdTomato) expression in the seed. Different acquisition setting was used to accommodate high expression in chalaza. Inset: maximum intensity projection of the 2-cell embryo in the main panel marked by dashed box with acquisition setting used for embryos. Scale bar for (a-h): 5 µm.

To preserve microtubule architectures for qualitative and quantitative analysis, we tested various mounting media (Supplementary Table 2) and various sample preparation procedures. Intact microtubule architectures in live protoplasts and late embryos had been achieved with 0.55 M mannitol [35] and 10% glucose [36], respectively. However, though embryos extracted with the established procedure [33, 34] with 5% glycerol in 1xPBS solution replaced with either 0.55 M mannitol or 10% glucose showed no sign of plasmolysis nor swelling and had preserved spindles and PPB, intact cortical microtubule arrays were rarely found. In the rare cases that the cortical microtubule arrays remained intact, the cortical microtubule array showed no clear sign of deterioration after 60 minutes of exposure in 0.55 M mannitol and 10% glucose (Fig. 2e). Therefore, since both 0.55 M mannitol and 10% glucose provided conditions to preserve microtubule architectures in embryo for at least 60 minutes, microtubule depolymerization must have occurred before the embryos' exposure to the mounting medium, likely due to the pressure applied during embryo extraction from seeds. To stabilize microtubules, microtubule stabilizing buffer (MTSB) [37] and 10 µM microtubule stabilizer paclitaxel (Taxol) [38] was included creating embryo microtubule mounting
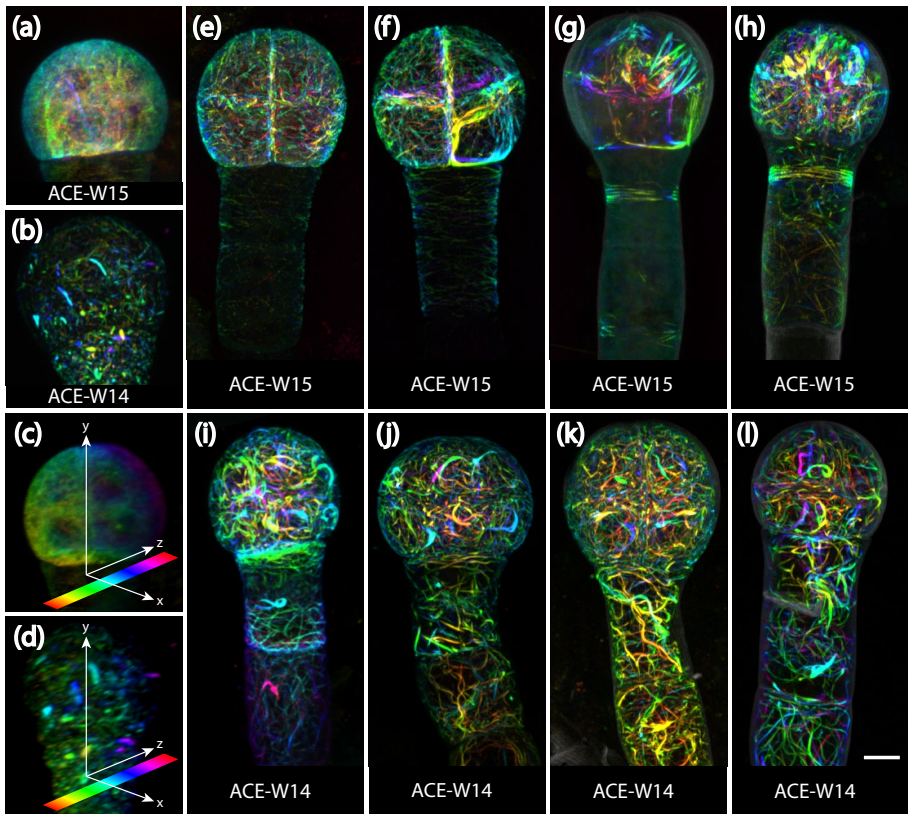
Fig. 2. Effects of mounting media on cytoskeleton integrity in embryos

(a,b) Maximum intensity projections of microtubule (a; ACE-W15; mGFP: AtTUA6) and actin (b; ACE-W14; Lifeact: tdTomato) markers in 8-cell embryos in 5% glycerol and 4% paraformaldehyde in 1x PBS solution. (c,d) Depth color coding key of all panels illustrated by rotating embryos in (a; panel c) and (b; panel d) by 90 degrees. LUT shows color values corresponding to depth of image in z-dimension. (e-l) Maximum projections of microtubule (e-h; ACE-W15; mGFP: AtTUA6) and actin (i-l; ACE-W14; Lifeact: tdTomato) markers in 8-cell embryos imaged in EGM solution (e,i), EMTM solution (f,j), EMTC solution (g), EGC solution (k), or EMTM followed by adding EMTC (h,l). All images from same markers were acquired with same acquisition settings. Scale bar: 5 μm.

(EMTM) solution. While Taxol treatment could alter microtubule architecture and cause cell swelling after prolonged (2-24 hours) treatment [38-40], no significant differences in microtubule orientation and microtubule anisotropy were detected between root epidermal cells incubated with or without Taxol, even after 90 minutes of treatments (Supplementary Fig. 2; Supplementary Table 3). Seeds incubated in EMTM for 15 minutes before embryo extraction preserved microtubule architectures homogenously labelled by TUA6-GFP in over 90% (n=74/81) of extracted embryo for at least 60 minutes after extraction (Fig. 2f). However, while this procedure allowed visualization of microtubules, topology of the network relative to cell shape could not be inferred without counterstaining plasma membrane or the cell wall. Thus, we included 0.1% of the cell wall stain Renaissance SR2200 in EMTM (named embryo microtubule counterstaining solution, EMTC). This led to depolymerization of cortical microtubules (Fig. 2g) and suggests that Renaissance SR2200 may compromise Taxol-dependent microtubule stabilization. To circumvent the negative effect of SR2200, seeds were first incubated in EMTM for 15 min to stabilize microtubules, and an equal volume of EMTC was then added immediately before embryo extraction. With this modification, microtubule architectures were preserved (Fig. 2h).

Actin architectures, on the other hand, could be preserved in all tested mounting media except 5% glycerol in 1xPBS solution with actin filaments and cables homogenously labelled by Lifeact (Fig. 2i-k). Since Taxol targets specifically tubulin [41], we thus tested omitting MTSB and Taxol in EMTM and EMTC (named embryo general mounting solution, EGM, and embryo general counterstaining, EGC, respectively) and found no clear negative effect on the integrity of actin architectures (Fig. 2l).

Having established optimized imaging media and methods, we next imaged a panel of ACE-W markers for subcellular structures (Supplementary Fig. 3). Reporters marking plasma membrane domains, plasmodesmata, organelles, or nuclei were imaged in EGC. Plasmamembrane-localized protein PIP2, NPSN12, BOR1, and NIP5;1 evenly labelled their corresponding domains, although PIP2, NPSN12, and NIP5;1 were also found intracellularly (Fig. 3a-c, Supplementary Fig. 3); markers derived from Rab protein families labelled various stages of endosomes appeared as punctate, dot-like structures in the cytoplasm (Fig. 3d) with minor fluorescence intensity variation between each endosome labeled by RabF2b and RabC1 when compared to those labeled by VTI12 (Supplementary Fig. 3); Golgi bodies labelled by GOT1p and SYP32 also appeared as punctate, dot-like structures in the cytoplasm but with uniform fluorescence intensity among all labeled Golgi bodies (Fig. 3e, Supplementary Fig. 3); tonoplast specific VAMP711 evenly labelled the tonoplast marking the contour of vacuoles (Fig. 3f, Supplementary Fig. 3); NUP54 and NUP75, labelled the nuclear pore complexes as dots
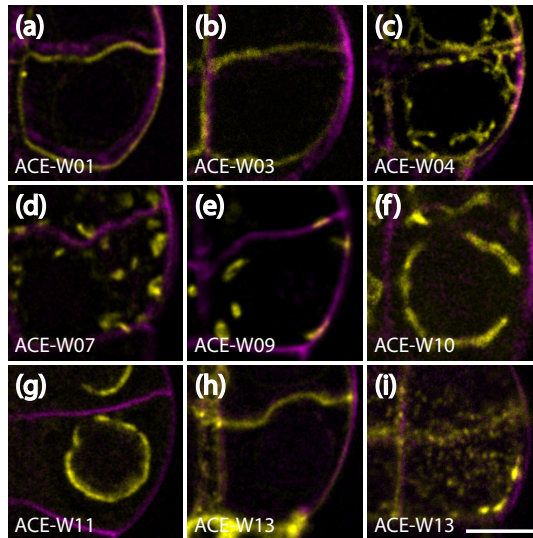
Fig. 3. ACE-W markers label cellular compartments in embryos
Single optical sections of plasma membrane (a; ACE-W01; AtPIP2A: GFP), inner membrane (b, ACE-W03; BOR1: mCitrine), outer membrane (c; ACE-W04; mCherry: NIP5;1), trans-Golgi network and early endosomes (d; ACE-W07; eYFP: VTI12), Golgi complex (e; ACE-W09; eYFP: GOT1p), to-noplast and vacuole (f; ACE-W10; eYFP: VAMP711), nuclear pore complex (g; ACE-W11; AtNUP54: GFP) and plasmodesmata (h,i; ACE-W13; mCherry: AtPDCB1) markers. Note that all markers are imaged in the center of one of the lower tier cells in an 8-cell embryo, except panel (i), which is imaged at the upper cell surface. Scale bar for all panels: 5μm.

embedded in the nuclear envelope and in the cytoplasm (Fig. 3g, Supplementary Fig. 3); and plasmodesmata callose binding PDCB1 labelled the plasmodesmata as dots on the interfaces between cells (Fig. 3h,i, Supplementary Fig. 3). All markers labelled patterns consistent with their designated cellular components, and in line with morphologies described in other organs [21-25, 27, 30, 42-48].

Thus, with this panel of markers, and an optimized imaging procedure, we can now visualize both robust and fragile subcellular structures in the early *Arabidopsis* embryo.

Early establishment of central/peripheral polarity

To answer the question of when polarity axes are established and implemented in each cell during embryogenesis, we studied four polarly localized proteins, OPS [28], BASL [29], BOR1 [30], and NIP5;1 [30] that labelled apical, basal, central, and central side of the cells relative to the body axis, respectively. While ACE lines harboring BOR1 (ACE-W03) and NIP5;1 (ACE-W04) were obtained and showed clear fluorescence signals (Fig. 4a-c, g-i), no transgenic plants were obtained from reporters containing OPS nor BASL despite multiple attempts.

We hypothesized that polarity was established at the latest before the 16-cell stage, when protoderm is separated from inners cells in a genetically regulated asymmetric cell division [20]. It was likely that polarity perception would be involved in positioning the cell division plane parallel to the embryo surface.

The BOR1 marker was found most abundantly on plasma membrane facing toward the central axis and the suspensor with lower fluorescence intensity in the peripheral plasma membrane at 4- and 8-cell stage (Fig. 4a, b). Fluorescence became exclusive to the plasma membrane facing toward the central axis and the suspensor in 16-cell embryos (Fig. 4c). However, the higher BOR1 levels were found in plasma membrane facing toward the central axis and towards the suspensor could be due to the sum of fluorescence intensity from two neighboring plasma membranes compared to the single peripheral plasma membrane. To non-invasively verify the polar localization of BOR1 in the early embryo, we compared the fluorescence intensity profiles with that of the homogenous plasma membrane proteins, PIP2 [22] (ACE-W01) and NPSN12 [21] (ACE-W02). A 5 µm wide cross section across the embryo was selected for fluorescence intensity profiles, and the central/peripheral fluorescence intensity ratios were calculated (Fig. 4j). If there were any preferential localization, the fluorescence intensity profile of the given protein would be different from the fluorescence intensity profiles of homogenous plasma membrane proteins. We first compared fluorescence profiles and central/peripheral fluorescence intensity ratios between PIP2 and NPSN12 to validate this approach. From 4- to 16-cell stage, fluorescence profiles of PIP2 and NPSN12 all had peaks at position corresponding to the plasma membrane with comparable height and sometimes even lower peak at the central plasma membrane (Fig. 4d-f). There was no significant difference in their central/peripheral fluorescence intensity ratios (Supplementary Table 4). When compared with the fluorescence intensity profiles of PIP2, BOR1 had a distinct peak at the center and lower peaks at the flanks of the fluorescence intensity profile in 4- and 8-cell embryos, while no peaks remain in the flanks with distinct peak in the center and middle of the fluorescence intensity profile at 16-cell embryo (Fig. 4a-f). The difference in the fluorescence intensity profiles were
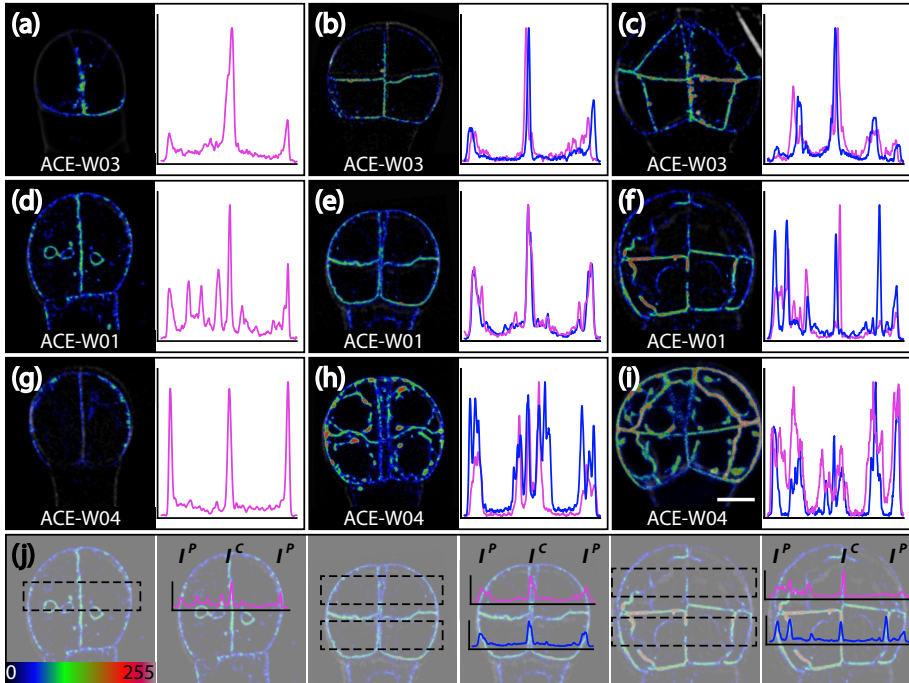
Fig. 4. Early establishment of inner-outer cell polarity in embryos

Single optical sections through 2-cell (a,d,g), 8-cell (b,e,h) and 16-cell (c,f,i) embryos expressing inner membrane marker ACE-W03 (a-c; BOR1: mCitrine), general plasma membrane marker ACE-W01(d-f; AtPIP2A: GFP) or outer membrane marker ACE-W04 (g-i; mCherry: NIP5;1). Images are shown in an intensity color scale according to the LUT in the bottom left. In each panel, the fluorescence intensity profile is shown in a graph on the right side. Positions of each region for intensity profiles are indicated in panel (j) underneath each row of embryos. Fluorescence intensity profiles of upper (magenta) and lower (blue) tier cells were generated through averaging fluorescence intensity of each pixel with the same x coordinate in the regions of interest (ROI) shown as dashed boxes. The fluorescence intensity ratios are ratios between IC and IP. Images from the same markers were acquired with same acquisition setting and are in same scale. Scale bar: 5 µm.

further supported by the significantly higher central/peripheral fluorescence intensity ratios of BOR1 compared to those of PIP2 and NPSN12 from 4- to 16- cell embryo (Supplementary Table 4). We thus concluded that BOR1 was polarly localized on the central faces of plasma membranes from at least as early as the 4-cell embryo.

We next analyzed NIP5;1 which had previously been shown to mark outer membranes [30]. Unlike the consistent polar plasma membrane-localized BOR1, NIP5;1 was not only found on the peripheral plasma membrane, but also accumulated in intracellular compartments in 4- to 16-cell embryo (Fig. 4g-i). NIP5;1's fluorescence intensity profiles in most 4- and 8-cell embryos had three peaks with comparable height with additional peaks when the sampling area crossed the intracellular compartment with accumulated NIP5;1. NIP5;1's fluorescence intensity profiles in most 4- and 8-cell embryos were similar to those of PIP2 (Fig. 4g,h). In 16-cell embryos, the peripheral localization of NIP5;1 became more consistent and distinct (Fig. 4i). NIP5;1's fluorescence intensity profiles had a central peak lower than the flanking peaks (Fig. 4i). NIP5;1's central/peripheral fluorescence intensity ratios though had lower average, were not significantly different from PIP2 and NPSN12 until 16-cell and 8-cell embryos, respectively (Supplementary Table 4). These results suggested that while NIP5;1 could be polarly localized to the peripheral plasmamembrane from 4-cell embryo, NIP5;1's peripheral localization only became robust in the 16-cell embryo.

In conclusion, BOR1 was robustly centrally localized from 4-cell embryo onwards while NIP5;1, though of which peripheral localization was observed from 4-cell embryos, was only robustly peripherally localized in the upper tier of embryos from 16-cell embryos. These results suggested that the ability to distinguish between central and peripheral plasma membrane and to deploy specific proteins to their corresponding locations is already established in 4-cell embryo.

Crowded embryo cells show no preferential organelle position

To determine if there was any preferential localization or morphological change of the endomembrane system during early embryogenesis, we examined the distribution and morphology of Golgi complex, various stages of endosomes, and vacuoles from 4-cell to 16-cell stage.

Endosomes marked by ACE-W07 and Golgi complexes marked by ACE-W09 were both loosely distributed close to the plasmamembrane in 4- and 8-cell embryos, and their density in each cell seemed to increase in 16-cell embryos (Fig. 5a,b). This increased density suggested an increased secretion and endocytosis activity to accommodate the increase in embryo volume from 16-cell stage onward [20]. However, no distinguishable local aggregation of Golgi complexes and endosomes were observed from 4- to 16-cell embryos (Fig. 5a,b).

Vacuoles marked by tonoplast specific ACE-W10 on the other hand, showed a wide range of morphologies and distributions during early embryogenesis.

Three types of vacuole morphologies were found in 4- to 16-cell embryos. Type 1 represented large foil-like vacuoles with distinguishable transvacuolar strands, but without distinct bulbs (Fig. 5c, d). This type of vacuoles tightly enclosed a spherical space in the cell, presumably the nucleus (Fig. 5d). Type 2 vacuoles were also large, but with several distinguishable bulbs emanating from the spherical space, which the vacuoles loosely enclosed (Fig. 5e,f). Type 3, unlike the former two, was composed of vacuoles with many small bulbs seemingly filling the cell (Fig. 5g,h). All types of vacuole morphologies were observed from 4- to 16-cell stages and could vary between cells in each embryo (Fig. 5c,e,g). Though most embryos have all cells with the same vacuole morphology, combinations of different vacuole morphologies could occasionally be found (Fig. 5g). Similar changes of vacuole morphology were also observed in earlier finding in shoot meristem cells [49] suggesting embryos might share vacuole dynamics with meristematic cells.

Nuclear envelopes marked by ACE-W11 revealed that nuclear envelope morphology also changed as cellular development progressed in 4- to 16-cell embryos. Two types of nuclear envelope morphologies were found in both embryo proper and suspensor at all stages examined. The first type had a smooth surface with NUP54 evenly distributed and enclosing a spherical space (figure 5i), while the second type showed a wavy surface (Fig. 5j). Both types could be found in the same embryo (Fig. 5k). To confirm the identity/ nature of the spherical space surrounded by the vacuole and determine if the nuclei movement was involved in the asymmetric cell division between 8- and 16-embryos, we measured the diameter of the nuclei in 8-cell embryos to determine if it was consistent with the diameter of the spherical space encompassed by the vacuoles. The average diameter of the nuclei in 8-cell embryo was 5.6±0.7µm (n=131 nuclei) at 8-cell stage. Therefore, with the relative large nuclei in the embryo cells and the similarity in both shape and positioning with the spherical space surrounded by the vacuole, it was likely the spherical space encompassed by the vacuole could only be the nuclei but also suggested very limited room for nuclei movement without deforming the nuclei.

In conclusion, each cell in 4- to 16-cell embryos was filled with non-polar localized endosome and Golgi close to the plasma membrane, with vacuoles, either tightly or loosely enclosing the nuclei, which showed no clear movement at the symmetric and asymmetric division between 4- and 8-cell embryo and between 8- and 16-cell embryos, respectively. The lack of polar aggregation of endosomes and Golgi complexes or preferential positioning of vacuoles suggested that there might not be directional cell growth or expansion at early embryogenesis. While the lack of nuclei movements suggested that nuclear movement might not be required for the asymmetric cell division between 8- and 16-cell embryos.

ACE-W07

ACE-W09

ACE-W10

ACE-W11

shallow   deep
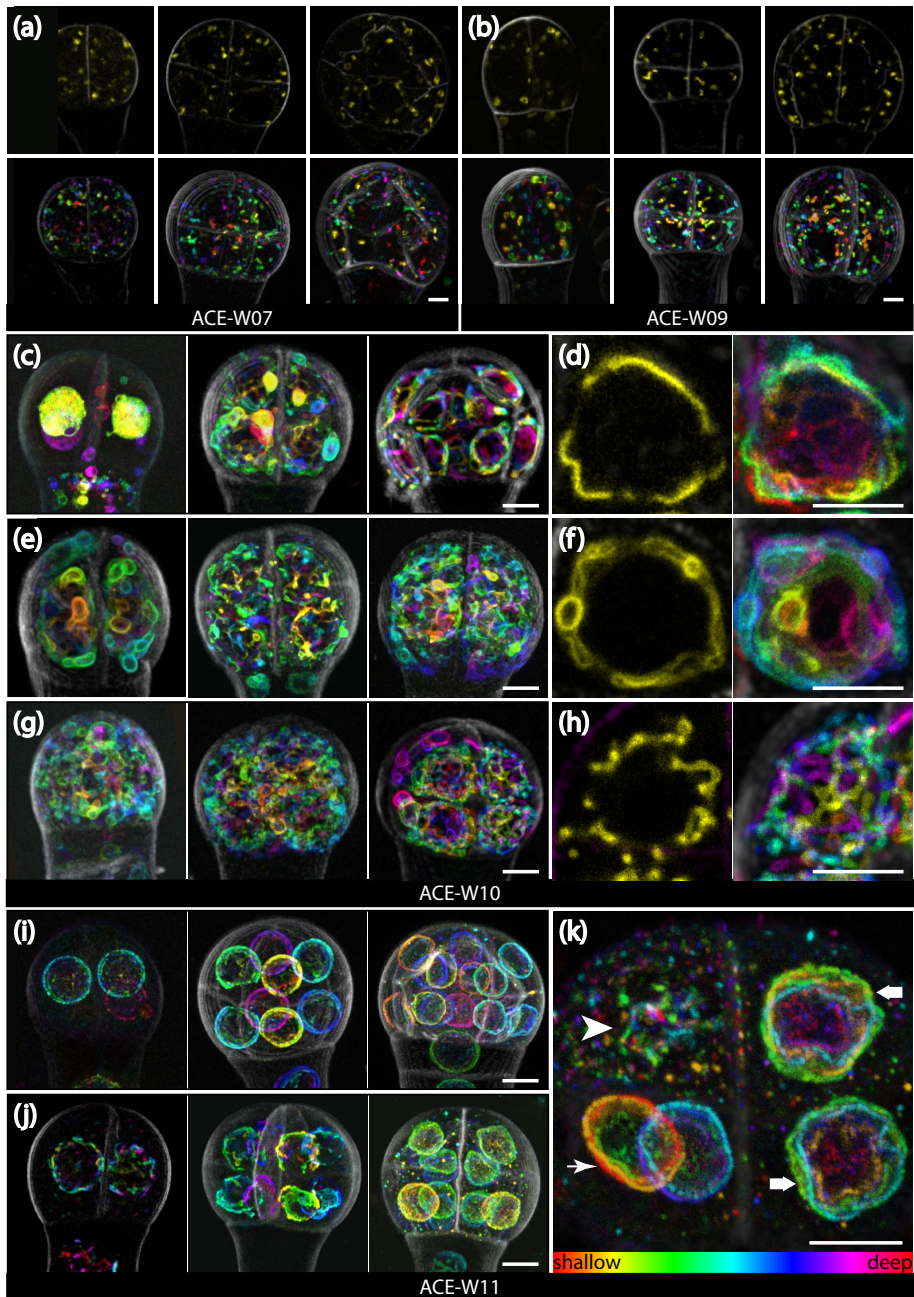
Fig. 5. Endomembrane morphologies in early embryos

(a,b) Single optical sections (top rows) and depth-coded maximum intensity projections (bottom rows) of endosomes and trans-Golgi network (a; ACE-W07; eYFP: VTI12) and Golgi complex (b; ACE-W09; eYFP: GOT1p) in 4-cell (left row), 8-cell (middle row) and 16-cell (right row) embryos.

(c-h) Maximum intensity projections of depth coded stacks of vacuoles labeled by ACE-W10 (eYFP: VAMP711) in 4-cell (c,e,g; left rows), 8-cell (c,e,g; middle rows), and 16-cell (c,e,g; right rows) embryos. (d,f,h) represent zoomed in of single cells representing corresponding vacuole morphologies in (c), (e) and (g), respectively, and are shown as single optical section (left row) or depth-coded maximum intensity projection (right row). Distinct vacuole morphologies are Type 1 (c,d), Type 2 (e,f) and Type 3 (g,h).

(i-k) Maximum intensity projection of depth coded stacks of nuclear envelopes labeled by the nuclear pore complex marker ACE-W11 (AtNUP54: GFP) in 4-cell (left row in i,j), 8-cell (middle row in i,j), and 16-cell (right row in i,j) embryos. (i) represents embryos with smooth nuclear envelopes and (j) shows embryos with wavy nuclear envelopes. (k) Maximum projection of depth coded stack of an 8-cell embryo with both smooth (arrows) and wavy (thick arrow) nuclear envelopes, and nuclear pore complexes accumulating in the spindle during mitosis (arrowhead). All images of the same marker were acquired with identical acquisition setting. Scale bars: 5 μm.

Cytoskeleton organization during embryogenesis

To understand how the cytoskeleton is rearranged to accommodate the constant change of division plane during early embryogenesis, we examined actin and microtubule architecture labelled by Lifeact (ACE-W14) and TUA6 (ACE-W15) in 4-cell to early globular embryos.

We found that actin architectures in early embryos were very different from earlier studies in post-embryonic meristem and differentiated cells [25, 50-56]. In mitotic cells in the root apical meristem, actin is found mainly as a fine and dense meshwork without F-actin bundles [53, 54]. In the embryo however, cells had thick F-actin bundles forming a dense meshwork throughout the cytoplasm without prominent orientation (Fig. 6 a-e). From early-globular embryos, the F-actin meshwork seemed more organised than in younger embryos (Fig. 6e). Notable, F-actin bundles stretched around the nuclei at later stages (Fig. 6c). In addition, from 8-cell embryo onwards, a thick arch F-actin bundle could be found in each embryo proper cell (Fig. 6c-e). These arch structures were associated with the nuclei though not always at the nucleus equator, and orientations were not correlated to the orientations of previous nor following cell division (Fig. 6c-e). In suspensor cells, the noticeable difference is the absence of the peri-nuclear arch and the cortical actin filaments when compared with in embryo proper cells (Fig. 6a-e).
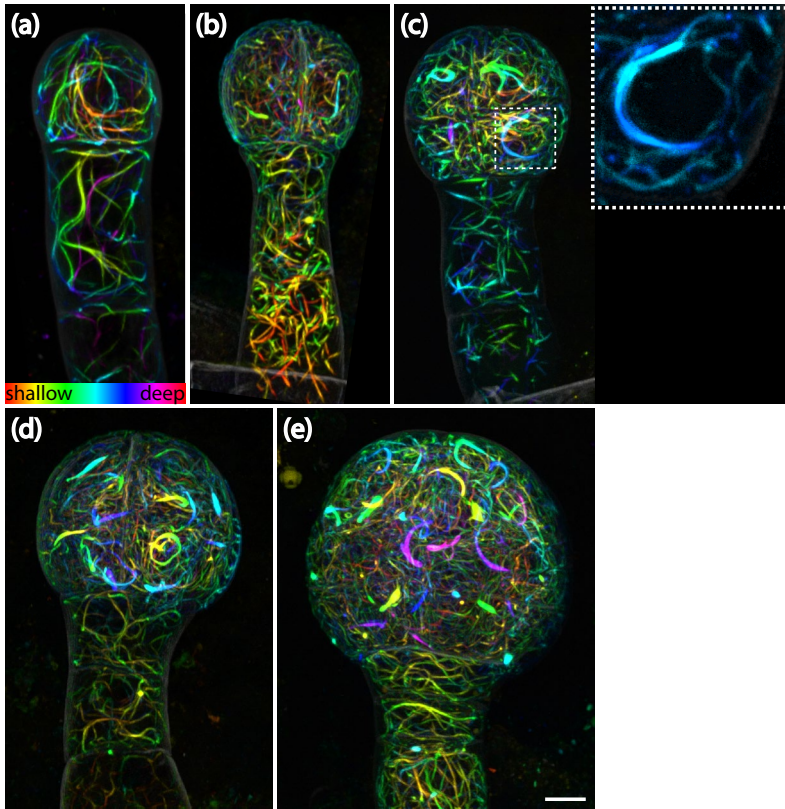
Fig. 6. Actin topology in early embryos

Maximum intensity projections of depth-coded stacks of actin labelling (ACE-W14; Lifeact: tdTo-mato) in 2-cell (a), 4-cell (b), 8-cell (c), 16-cell (d) and early globular (e) embryos. The inset in panel (c) shows a peri-nuclear actin arch.

Images were acquired with same acquisition setting and are in same scale. Scale bar: 5 µm.

In addition, the F-actin bundle meshwork in the suspensor cells were looser than in embryo proper cells and showed no prominent orientation (Fig. 6a-e).

Microtubules in early embryos were straight cables (Fig. 7a). Microtubule structures including cortical microtubule array, cytoplasmic microtubule bundles, pre-prophase bands, spindles, and phragmoplast were present with mitotic and cytokinesis related structures with their orientations consistent with expected cell division orientation (Fig. 7b). Only cortical microtubule array on the periclinal faces could be examined due technical limitations (see Discussion), and pro-embryo cells and suspensor cells showed obvious difference in their cortical microtubule arrangements. In pro-embryo cells, the cortical microtubule arrays were dense and seemed to lack prominent orientation during most of the interphase though occasionally, presumably at the early G1 or/and late G2 phase, became more organised (Fig. 7c-f). In suspensor cells, cortical microtubule arrays were less dense and seemed more organised with their orientation being perpendicular to the embryo axis (Fig. 7c-e). With the uniform periclinal cortical microtubule array and the single-cell-layer nature of suspensor cells, the periclinal cortical microtubule array of suspensor cells could be readily analysed with FibrilTool [57], and the results supported the dominant orientation (Fig. 7g-i).

In conclusion, all mitotic and cytokinetic cytoskeleton structures were found in early embryos and their orientations followed the expected cell division orientations. This suggests both F-actin meshwork and microtubules in embryo cells behave as described in late and post-embryonic cells.
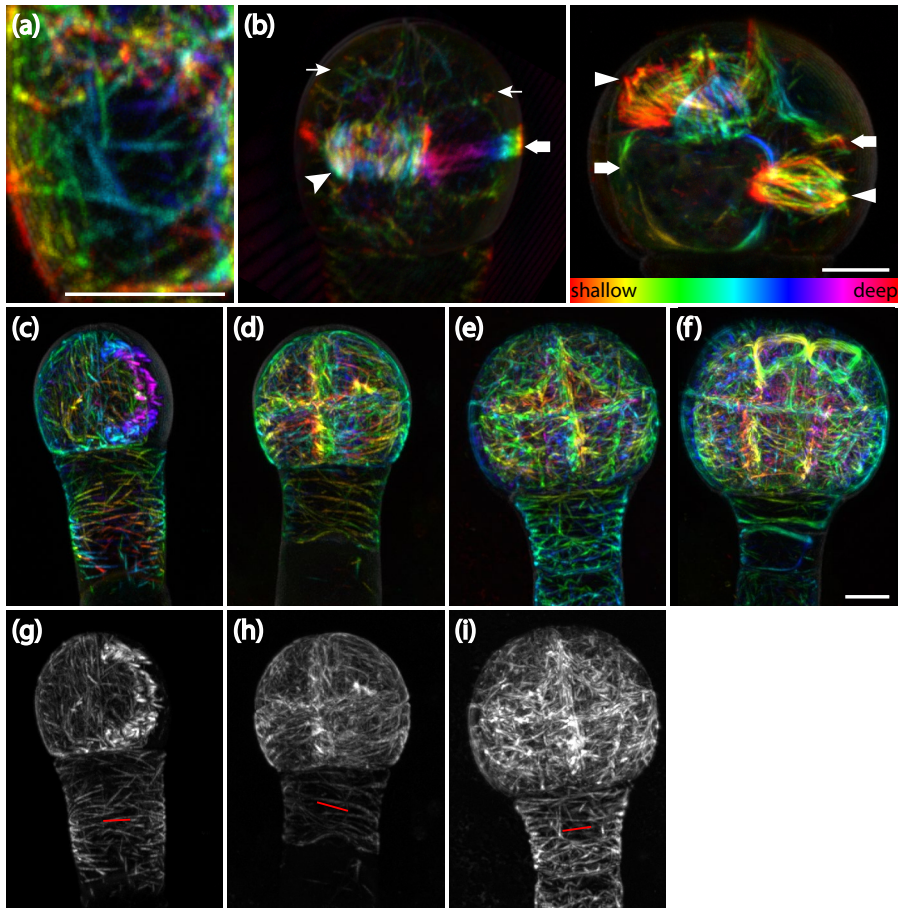
Fig. 7. Microtubule topologies in early embryos

Labelling of Microtubules with the ACE-W15 (mGFP: AtTUA6) marker reveals filaments (a), as well as cytoplasmic signals (thin arrows in left image of panel b), phragmoplast (arrowhead in left image of panel b), preprophase band (thick arrows in both left and right images in panel b), and spindles (triangles in right image in panel b) in early embryos. (c-i) Microtubules in 4-cell (c,g), 8-cell (d,h), and 16-cell (e,i) and early globular (f) embryos shown either as depth-coded stacks (c-f) or maximum intensity projections (g-i). Orientation of cortical microtubules in the suspensor is marked by red lines in (g-i). Images were acquired with same acquisition setting and are in same scale, except (a) and (b). Scale bar: 5 μm.

Discussion

In this study, we have generated a comprehensive set of cellular reporters driven by *RPS5A* and *WOX2* promoters that were specifically designed for imaging cellular reorganization in early *Arabidopsis* embryos. With these cell type-specific promoters, expression level of he reporter genes could be maximized while minimizing the background signal from surrounding cells, and preventing morphological defects commonly found when using constitutive and ubiquitous reporters [50, 58]. This feature allowed us to capture clear cellular structures to dissect the cellular organization and regulation in embryos. The combination of embryo specific ACE's and our optimized imaging procedure allowed preserving delicate cellular structures and detailed documentation of their three-dimensional architectures and thus overcomes the major obstructions for dissecting cellular reorganization in embryos.

Using this panel of markers, we addressed a number of questions. First, we found that central-peripheral cellular polarity is established extremely early in the embryo. This was evident from the polar localization of BOR1 and later NIP5;1 proteins. Both are polarity probes that were mis-expressed in early embryo and still targeted to expected inner or outer domain based on imaging in multi-layered post-embryonic tissues [30]. This suggests that a polar transport and/or sorting mechanism is already established in early embryos, but also that the central-peripheral faces of early embryo cells are molecularly distinguished as early as from the second, and perhaps even the first, cell division. Importantly, establishment of central-peripheral polarity in each cell does not depend on the presence of multiple cell layers. In addition, a large portion of embryonic cells was occupied by the nucleus, vacuoles, and other organelles along with the dense F-actin bundle meshwork. This suggests that cytoplasmic volume is very limited, and therefore intracellular trafficking and active cytoplasmic streaming may be relatively efficient in early embryo cells. These properties of early embryonic cells made it unlikely that gradients of small molecule diffusible morphogens in each cell serve as guide for polarity establishment. Therefore, the polarity establishment at early embryo might be caused by other factors such as a combination of the molecular property of cell walls and genetic regulation.

Besides limiting the small molecule gradients within the cells, the small sizes of embryo proper cells with the relatively large nuclei also restrict nuclear movement. In an 8-cell embryo, with a diameter of 5.6 µm, each nucleus could only move within a sphere with a diameter 6.4 µm, or 0.4 µm in each direction when the nucleus is in the center of this sphere, without deforming the nucleus as we observed. This suggests that nuclei movement might not occur nor be required for the asymmetric cell division between 8- and 16-cell embryos to establish the central and peripheral cell layers for proper pattern formation. Nucleus position has been shown to be correlated with

division plane in asymmetric divisions [59, 60] , where the division plane goes through the center of the prior nucleus position. However, both symmetric and asymmetric divisions in early embryo cells can be generated following this principle without moving the nucleus.

Our finding that the mitotic and cytokinetic microtubule architectures aligned with the expected division orientation in the early embryo, suggested that microtubule dynamics may be similar to those in post-embryonic cells. Given that early embryo cells can easily be segmented in 3D (Yoshida *et al*., 2014), and that cell division patterns in *Arabidopsis* embryos are highly predictable, this now opens the possibility to determine contributions of genetically regulated cytoskeletal remodeling to cell division control. However, there are limitations to imaging microtubules in the embryo that can not easily be overcome. Firstly, all outer membranes are curved, and thus cytoskeleton topology can not easily be extracted. Secondly, high-resolution imaging is limited to those membranes that lie in the x/y plane because resolution along the z-axis is much lower using confocal microscopy, and embryos can not easily be tilted during observation. Therefore, instead treating each cell as a plane and process images through maximum projection, three-dimensional reconstruction and analysis will be the next technical challenge for any quantitative analysis on the cytoskeleton organization during embryogenesis.

Beyond these examples, we expect that many outstanding questions related to the cell biology of tissue patterning can now be addressed using this set of marker lines.

Materials and Methods

Plasmid construction and plant material

All constructs, reporter cassettes and their corresponding DNA templates as well as all oligonucleotides used in this study are listed in Supplementary Table 2. *pGIIB/ pWOX2::LIC:tNOS* was generated through excising "*pRPS5A*" cassette in *pPLV28* [61] with *Acc65I* digestion and ligated with *Acc65I* digested "*pWOX2*" cassette. "*pWOX2::LIC*" cassette in *pGIIB/pWOX2::LIC:tNOS* was then excised with *ACC65I* and *NotI* double digestion and ligated with *pGIIN* (kind gift from T. Laux, University Freiburg, Germany) linearized with same restriction digestion to generate *pGIIN/pWOX2::LIC:tNOS*. All reporting cassettes except "*Lifeact*" were introduced into *HpaI* linearized *pPLV28* and *pGIIN/pWOX2::LIC:tNOS* through ligation independent cloning [62] to generate ACE reporter constructs with corresponding promoter. *pGIIB/pRPS5A::Lifeact:tdTomato:tNOS* was generated through introducing oligonucleotide dimer "*Lifeact*" into *pGIIB/pRPS5A::LIC:tdTomato:tNOS* through ligation independent cloning. *pGIIB/pRPS5A::LIC:tdTomato:tNOS* was generated through ligating *BamHI* linearized *pPLV28* with ""*tdTomato*" excised from *pPLV23* [61]. *pGIIN/pWOX2::Lifeact:tdTomato:tNOS* was generated through introducing "*Lifeact:tdTomato*" amplified from *pGIIB/pRPS5A::LIC:tdTomato:tNOS* into *HpaI* linearized *pGIIN/pWOX2::LIC:tNOS* via ligation independent cloning.

All ACE reporting constructs were introduced into *Arabidopsis thaliana* ecotype *Col-Utrecht* with the *mpB4149* mutation [63] heterozygous in the background, through floral dip [64]. T1 transgenic plants of ACE-R markers were selected with DL-Phosphinotricin (SIGMA), and T1 transgenic plants of ACE-W markers were selected with Norflurazon (Supelco) [65]. T3 homozygotes without the *mpB4149* allele were used in this study.

Seeds harboring *p35S:: GFP: TUA6* were sterilized via incubated in five times dilution of household bleach containing approximate 5% sodium hypochlorite with demineralized water for 10 minutes followed by 5 times washing with sterilized demineralized water. The sterilized seeds were plated on 1/2MS0 medium plates containing 0.8% agar. After stratification at 4°C for two days, the plates were transferred to phytochamber (22°C, 16 hours light and eight hours dark). After six days of growth in the phytochamber, the seedlings used to test short-term effect of Taxol on microtubule organization.

Microscopy and image analysis

Embryo samples were prepared as described in Supplementary Fig. 4 with mounting and counterstaining solutions listed in Supplementary Table 2. Fluorescence intensity profiles used for verifying BOR1 and NIP5;1 polar localization were generated through the "Analyze/plot profile" function in Fiji [66]. A 5 µm wide band perpendicular to the suspensor axis that crossed a region directly above or under the cell wall, which separates the upper and lower tiers of embryo proper, was defined as the region of

interest (ROI) for quantification. The ROIs and results were saved, and the fluorescence intensity profiles were exported and plotted in MS Excel™. Plasma membrane signals of each face in each fluorescence intensity profile were defined through examining the corresponding confocal image and identifying the coordinate ranges of each face in the ROI, the maximum intensity in each coordinate range was then extracted using MS Excel™ to calculate the central-peripheral fluorescence intensity ratio.

Root treatments with paclitaxel (SIGMA) were conducted through live imaging and the samples were prepared as described in Supplementary Fig. 5, and microtubule orientation and anisotropy were analyzed as described[57].

Images were acquired in 8-bit format using a Leica TCS SP5II confocal laser scanning microscope with 63× NA = 1.20 water-immersion objective with pinhole set to 1.0 Airy Unit. mGFP and mCitrine were excited by Argon-ion laser, tdTomato, and SCRI Renaissance Stain 2200 (SR2200) (Renaissance Chemical) were excited using a diode laser, and their emissions were detected sequentially with Leica HyD in photon counting mode. Excitation and detection of fluorophores were configured as follows: mGFP was excited at 488 nm and detected at 498–528 nm; Venus was excited at 514 nm and detected at 524–554 nm; tdTomato was excited at 561 nm and detected at 571–630 nm; Renaissance 2200 was excited at 405 nm and detected at 430–470 nm.

Acknowledgements

References

1. Sablowski, R. *Curr. Opin. Plant Biol.* **34**, 54-60 (2016).
2. Besson, S. & Dumais, J. *Proc Natl Acad Sci U S A* **108**, 6294-6299 (2011).
3. Louveaux, M., Julien, J.D., Mirabet, V., Boudaoud, A. & Hamant, O. *Proc Natl Acad Sci U S A* **113**, E4294-4303 (2016).
4. Landrein, B. et al. *Elife* **4**, e07811 (2015).
5. De Rybel, B. et al. *Dev. Cell* **24**, 426-437 (2013).
6. van Dop, M., Liao, C.Y. & Weijers, D. *Curr. Opin. Plant Biol.* **23**, 25-30 (2015).
7. Buschmann, H. & Zachgo, S. *Trends Plant Sci.* **21**, 872-883 (2016).
8. Rasmussen, C.G., Humphries, J.A. & Smith, L.G. in Annual Review of Plant Biology, Vol. 62 387-409 (2011).
9. Smertenko, A. et al. *Trends Cell Biol.* **27**, 885-894 (2017).
10. Pickett-Heaps, J.D. & Northcote, D.H. *J. Cell Sci.* **1**, 121-128 (1966).
11. Pickett-Heaps, J.D. & Northcote, D.H. *J. Cell Sci.* **1**, 109-120 (1966).
12. Traas, J.A. et al. *J. Cell Biol.* **105**, 387-395 (1987).
13. Lloyd, C.W. & Traas, J.A. *Development* **102**, 211-221 (1988).
14. Gunning, B.E. & Wick, S.M. *Journal of cell science. Supplement* **2**, 157-179 (1985).
15. Rasmussen, C.G., Wright, A.J. & Muller, S. *Plant J.* **75**, 258-269 (2013).
16. Boruc, J. & Van Damme, D. *Curr. Opin. Plant Biol.* **28**, 92-98 (2015).
17. Cutler, S.R. & Ehrhardt, D.W. *Proc Natl Acad Sci U S A* **99**, 2812-2817 (2002).
18. Murata, T. & Wada, M. *Planta* **183**, 391-398 (1991).
19. Palovaara, J., De Zeeuw, T. & Weijers, D. in Annual Review of Cell and Developmental Biology, Vol. 32 47-75 (2016).
20. Yoshida, S. et al. *Dev. Cell* **29**, 75-87 (2014).
21. Geldner, N. et al. *Plant J.* **59**, 169-178 (2009).
22. Nelson, B.K., Cai, X. & Nebenführ, A. *Plant J.* **51**, 1126-1136 (2007).
23. Simpson, C., Thomas, C., Findlay, K., Bayer, E. & Maule, A.J. *Plant Cell* **21**, 581-594 (2009).
24. Tamura, K., Fukao, Y., Iwamoto, M., Haraguchi, T. & Hara-Nishimura, I. *Plant Cell* **22**, 4084-4097 (2010).
25. Era, A. et al. *Plant Cell Physiol.* **50**, 1041-1048 (2009).
26. Riedl, J. et al. *Nat. Methods* **5**, 605-607 (2008).
27. Ueda, K., Matsuyama, T. & Hashimoto, T. *Protoplasma* **206**, 201-206 (1998).
28. Truernit, E., Bauby, H., Belcram, K., Barthélémy, J. & Palauqui, J.C. *Development* **139**, 1306-1315 (2012).
29. Dong, J., MacAlister, C.A. & Bergmann, D.C. *Cell* **137**, 1320-1330 (2009).
30. Takano, J. et al. *Proceedings of the National Academy of Sciences of the United States of America* **107**, 5220-5225 (2010).
31. Breuninger, H., Rikirsch, E., Hermann, M., Ueda, M. & Laux, T. *Dev. Cell* **14**, 867-876 (2008).

32. Weijers, D. et al. *Development* **128**, 4289-4299 (2001).
33. Llavata-Peris, C., Lokerse, A., Möller, B., De Rybel, B. & Weijers, D. in Methods in Molecular Biology, Vol. 959 137-148 (2013).
34. Musielak, T.J., Schenkel, L., Kolb, M., Henschen, A. & Bayer, M. *Plant Reprod* **28**, 161-169 (2015).
35. Shi, L. et al. *Biochem. Biophys. Res. Commun.* **405**, 632-637 (2011).
36. Wang, Q. & Huang, S. *Mol Plant* **7**, 1397-1401 (2014).
37. Soltys, B.I. & Borisy, G.G. *J. Cell Biol.* **100**, 1682-1689 (1985).
38. Baskin, T.I., Wilson, J.E., Cork, A. & Williamson, R.E. *Plant Cell Physiol.* **35**, 935-942 (1994).
39. Bannigan, A., Wiedemeier, A.M., Williamson, R.E., Overall, R.L. & Baskin, T.I. *Plant Cell Physiol.* **47**, 949-958 (2006).
40. Mathur, J. & Chua, N.H. *Plant Cell* **12**, 465-477 (2000).
41. Manfredi, J.J., Parness, J. & Horwitz, S.B. *J. Cell Biol.* **94**, 688-696 (1982).
42. Hunter, P.R., Craddock, C.P., Di Benedetto, S., Roberts, L.M. & Frigerio, L. *Plant Physiol.* **145**, 1371-1382 (2007).
43. Ivanov, S. & Harrison, M.J. *Plant J.* **80**, 1151-1163 (2014).
44. Takano, J., Miwa, K., Yuan, L., Von Wirén, N. & Fujiwara, T. *Proceedings of the National Academy of Sciences of the United States of America* **102**, 12276-12281 (2005).
45. Takano, J. et al. *Plant Cell* **18**, 1498-1509 (2006).
46. van der Honing, H.S., van Bezouwen, L.S., Emons, A.M.C. & Ketelaar, T. *Cytoskeleton* **68**, 578-587 (2011).
47. Wang, H.J. et al. *Plant Physiol.* **173**, 566-581 (2017).
48. Benitez-Alfonso, Y. et al. *Dev. Cell* **26**, 136-147 (2013).
49. Seguí-Simarro, J.M. & Staehelin, L.A. *Planta* **223**, 223-236 (2006).
50. Dyachok, J., Sparks, J.A., Liao, F., Wang, Y.S. & Blancaflor, E.B. *Cytoskeleton (Hoboken)* **71**, 311-327 (2014).
51. Ketelaar, T. et al. *Curr. Biol.* **14**, 145-149 (2004).
52. Rahman, A. et al. *Plant J.* **50**, 514-528 (2007).
53. Sheahan, M.B., Staiger, C.J., Rose, R.J. & McCurdy, D.W. *Plant Physiol.* **136**, 3968-3978 (2004).
54. Voigt, B. et al. *Eur. J. Cell Biol.* **84**, 595-608 (2005).
55. Wang, Y.S., Motes, C.M., Mohamalawari, D.R. & Blancaflor, E.B. *Cell Motil. Cytoskeleton* **59**, 79-93 (2004).
56. Wang, Y.S., Yoo, C.M. & Blancaflor, E.B. *New Phytol.* **177**, 525-536 (2008).
57. Boudaoud, A. et al. *Nat Protoc* **9**, 457-463 (2014).
58. Abe, T. & Hashimoto, T. *Plant J.* **43**, 191-204 (2005).
59. Kimata, Y. et al. *Proc Natl Acad Sci U S A* **113**, 14157-14162 (2016).

60. Robinson, S. et al. *Science* **333**, 1436-1440 (2011).
61. De Rybel, B. et al. *Plant Physiol.* **156**, 1292-1299 (2011).
62. Aslanidis, C. & de Jong, P.J. *Nucleic Acids Res.* **18**, 6069-6074 (1990).
63. Willemsen, V. et al. *Plant Cell* **15**, 612-625 (2003).
64. Clough, S.J. & Bent, A.F. *Plant J.* **16**, 735-743 (1998).
65. Misawa, N. et al. *Plant J.* **4**, 833-840 (1993).
66. Schindelin, J. et al. *Nat. Methods* **9**, 676-682 (2012).
67. Benitez-Alfonso, Y. et al. *Dev. Cell* **26**, 136-147 (2013).

Supplementary information

Supplementary Table 1. Catalog of ACE lines

Marked compartment	ACE-R/W ##	Marker
Plasma membrane	01	AtPIP2A: GFP[22]
Plasma membrane	02	eYFP: NPSN12[21]
Central face	03	BOR1: mCitrine [30]
Peripheral face	04	mCherry: NIP5;1[30]
Late endosome, pre-vacuolar compartment	05	eYFP: RabF2b[21, 22]
Endosome, post-Golgi	06	eYFP: RabC1[21]
Early endosome, trans-Golgi network	07	eYFP: VTI12[21]
Golgi Complex	08	eYFP: SYP32[21]
Golgi complex	09	eYFP: GOT1p[21]
Tonoplast	10	eYFP: VAMP711[21]
Nuclear pore complex	11	AtNUP54: GFP[24]
Nuclear pore complex	12	AtNUP75: GFP[24]
Plasmodesmata	13	mCherry: AtPDCB1[23]
Actin filaments	14	Lifeact: tdTomato[26]
Microtubules	15	mGFP: AtTUA6[27]

Supplementary Table 2. Mounting solutions used in this study

Solution	Purpose	Composition
Embryo microtubule mounting (EMTM)	Provide adequate osmotic pressure for embryo cells. Stabilize microtubule architecture before embryo extraction.	10% glucose 10 µM Taxol 1x MTSB
Embryo microtubule counterstaining (EMTC)	Provide adequate osmotic pressure for embryo cells. Stabilize microtubule architecture. Provide counterstain for cellular contour.	10% glucose 10 µM Taxol 0.1% SR2200 1x MTSB
Embryo general mounting (EGM)	Provide adequate osmotic pressure for embryo cells.	10% glucose
Embryo general counterstaining (EGC)	Provide adequate osmotic pressure for embryo cells. Provide counterstain for cellular contour	10% glucose 0.1% SR2200
Remarks: All solutions are dissolved in demineralized water. 20% glu=cose (sterilized), 10 mM Taxol in 100% DMSO, and 10x MTSB (sterilized) stock solutions can be aliquoted and stored in dark at 4 or -20 °C. All solution must be made fresh right before use and not freezable. Reduced microtubule stabilizing ability of EMTM and EMTC after 4 hours room temperature exposure was observed.		

Supplementary Table 3. Effects of 90 minutes 10 µM Taxol treatment on cortical microtubule dynamics in root epidermal cells

	Δ Average microtubule orientation (°)			Anisotropy			
	0-30 min	0-60 min	0-90 min	0 min	30 min	60 min	90 min
Mock (n= 31)	5.97± 5.54*	8.39± 9.56	8.76± 13.01	0.08± 0.03	0.07± 0.03	0.06± 0.03	0.06± 0.02
10 µM Taxol (n= 44)	7.74± 10.24	11.50± 13.02	14.02± 17.42	0.08± 0.04	0.08± 0.05	0.07± 0.04	0.06± 0.03
p-value*	3.38E-1	2.38E-1	1.39E-1	9.38E-1	3.98E-1	1.33E-1	4.90E-1
* Two-tail student t-test							

Supplementary Table 4. Central/peripheral fluorescence intensity ratio (I^c/I^p) of ACE-W01, ACE-W02, ACE-03, and ACE-W04 in early embryos.

			ACE-W01	ACE-W02	ACE-W03	ACE-W04
4-cell		Log(I^c/I^p)	-0.03± .19 (n=18)	0.112± 0.206 (n= 8)	0.54± 0.15 (n=12)	0.10± 0.20 (n=16)
		p-value*	-	1.07E-01	8.94E-10	6.38E-02
		p-value**	1.07E-01	-	8.39E-04	8.70E-01
8-cell	Upper tier	Log(I^c/I^p)	0.30± 0.14 (n=18)	0.330± 0.094 (n= 12)	0.75± 0.33 (n=30)	0.24± 0.06 (n=24)
		p-value	-	4.47E-01	3.66E-08	9.90E-02
		p-value	4.47E-01	-	1.75E-07	5.07E-03
	Lower tier	Log(I^c/I^p)	0.27± 0.17 (n=18)	0.285± 0.069 (n= 12)	0.68± 0.26 (n=30)	0.15± 0.19 (n=24)
		p-value	-	7.25E-01	4.70E-08	5.05E-02
		p-value	7.25E-01	-	2.89E-09	5.78E-03
16-cell	Upper tier	Log(I^c/I^p)	0.26± 0.16 (n=12)	0.257± 0.223 (n= 8)	1.15± 0.20 (n=24)	-0.01± 0.17 (n=24)
		p-value	-	9.84E-01	3.92E-16	4.93E-05
		p-value	9.84E-01	-	4.02E-11	4.42E-03
	Lower tier	Log(I^c/I^p)	0.08± 0.17 (n=12)	0.236± 0.217 (n= 8)	1.23± 0.36 (n=24)	-0.03± 0.16 (n=24)
		p-value	-	1.14E-01	1.09E-14	7.09E-02
		p-value	1.14E-01	-	2.06E-10	3.73E-03
* Two-tailed Student's t-test compared with ACE-W01 ** Two-tailed Student's t-test compared with ACE-W02						

Supplementary Table 5. Primers used in this study

Product (ACE-R/W##)	Amplified cassette	Forward primer	Reverse primer	Template (as described in material sources)
-	pWOX2	ATTAGGTACCCGAAGAATGCAGCAAATAGG	ATTAGGGCCCGGTTTGCATGTAGGTTATGG	-
01	AtPIP2A: GFP	TAGTTGGAATAG-GTTCAAGTTCATTTCATTTGGAGAG	AGTATGGAGTTGGGTTCCTTTATTGC-CAAATGTTTGAAC	CD3-1003 [22]
02	eYFP: NPSN12	TAGTTGGAATAGGTTCGAGCAAAAGCT-CATTTCTGAAGAG	AGTATGGAGTTGGGTTCCACAATTCTAGTC-GACGGCCCAT	U60291 [21]
03	BOR1: mCi-trine	TAGTTGGAATAGGTTCATGGAAGAGA-CTTTTGTGCC	AGTATGGAGTTGGGTTCTTACTTGTA-CAGCTCGTCCA	BOR1-Cit (N. Geldner, personal contact)
04	mCherry: NIP5;1	TAGTTGGAATAGGTTCATGGTGAG-CAAGGGCGAGGA	AGTATGGAGTTGGGTTCTTAACGAC-GAAAGCTCCTAA	mCherry-NIP5;1 (N. Geldner, personal contact)
05	eYFP: RabF2b	TAGTTGGAATAGGTTCGAGCAAAAGCT-CATTTCTGAAGAG	AGTATGGAGTTGGGTTCCACAATTCTAGTC-GACGGCCCAT	U09899 [21]
06	eYFP: RabC1	TAGTTGGAATAGGTTCGAGCAAAAGCT-CATTTCTGAAGAG	AGTATGGAGTTGGGTTCCACAATTCTAGTC-GACGGCCCAT	U09677 [21]
07	eYFP: VTI12	TAGTTGGAATAGGTTCGAGCAAAAGCT-CATTTCTGAAGAG	AGTATGGAGTTGGGTTCCACAATTCTAGTC-GACGGCCCAT	U60796 [21]
08	eYFP: SYP32	TAGTTGGAATAGGTTCGAGCAAAAGCT-CATTTCTGAAGAG	AGTATGGAGTTGGGTTCCACAATTCTAGTC-GACGGCCCAT	U20852 [21]
09	eYFP: GOT1p	TAGTTGGAATAGGTTCGAGCAAAAGCT-CATTTCTGAAGAG	AGTATGGAGTTGGGTTCCACAATTCTAGTC-GACGGCCCAT	U63080 [21]
10	eYFP: VAMP711	TAGTTGGAATAGGTTCGAGCAAAAGCT-CATTTCTGAAGAG	AGTATGGAGTTGGGTTCCACAATTCTAGTC-GACGGCCCAT	U14984 [21]
11	AtNUP54: GFP	TAGTTGGAATAGGTTCATGTCGGCACTC-CGTCTTC	AGTATGGAGTTGGGTTCTTACTTGTA-CAGCTCGTCCA	35S::NUP54-GFP [24]
12	AtNUP75: GFP	TAGTTGGAATAGGTTCATGCCGGGTAT-GTCTTCGGA	AGTATGGAGTTGGGTTCTTACTTGTA-CAGCTCGTCCA	35S::NUP75-GFP [24]
13	mCherry: AtPDCB1	TAGTTGGAATAGGTTCATGGCTGCTCTG-GTGCTTTC	AGTATGGAGTTGGGTTCTTAGAGCATCAG-GAAAGAGC	p35S::mCherry-PDCB1 [67]
-	Lifeact	TAGTTGGAATAGGTTCATGGGTGTCGCA-GATTTGATCAAGAAATTCGAAAGCATCT-CAAAGGAAGAAGGG	AGTATGAGTTGGGTTCCCTTCCTTTCCTTT-GAGATGCTTTCGAATTTCTTGATCAAATCT-GCGACACCCATG	Lifeact-Venus forward primer [25]
14	Lifeact: tdTomato	TAGTTGGAATAGGTTCATGGGTGTCGCA-GATTTGATCAAGAAATTCGAAAGCATCT-CAAAGGAAGAAGGG	AGTATGGAGTTGGGTTCTTACTTGTA-CAGCTCGTCCA	pGIIB/pRPS5A::LIC:tdTomato:tNOS (this work)
15	mGFP: At-TUA6	TAGTTGGAATAGGTTCATGACTAGTA-AGGGCGAGGA	AGTATGGAGTTGGGTTCTTAGTATTCCT-CATGATCAT	CaMV35S:GFP-TUA6 (T. Ketelaar, personal contact)
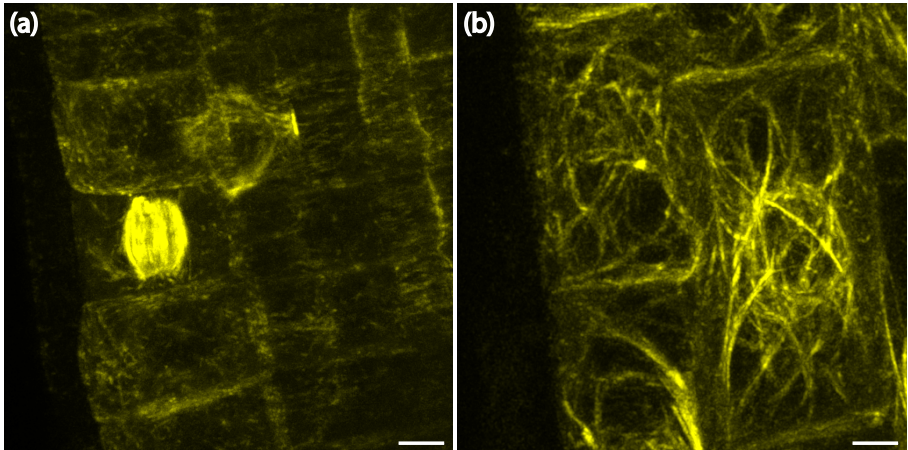
Supplementary Fig. 1. Microtubule and actin structures in root tip labeled by ACE-R15 and ACE-R14

Maximum projections. Scale bar: 5 µm
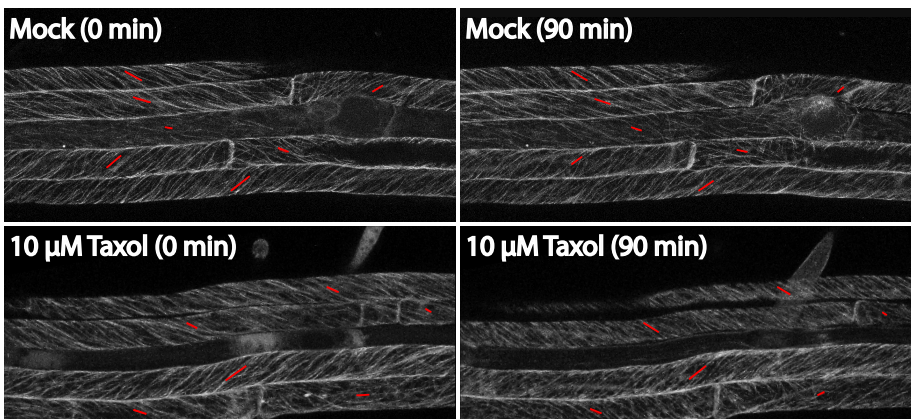
Supplementary Fig. 2. Effect of Taxol on microtubules in roots.

Effect of 90 minutes 10 µM Taxol treatment on cortical microtubule organization in root epidermal cells of 6 day-post-germination p35S:: GFP: TUA6 seedlings. Mock treatment represents solvent control in water. Maximum projections. Orientations and length of red lines represent the average microtubule orientation and anisotropy, respectively.
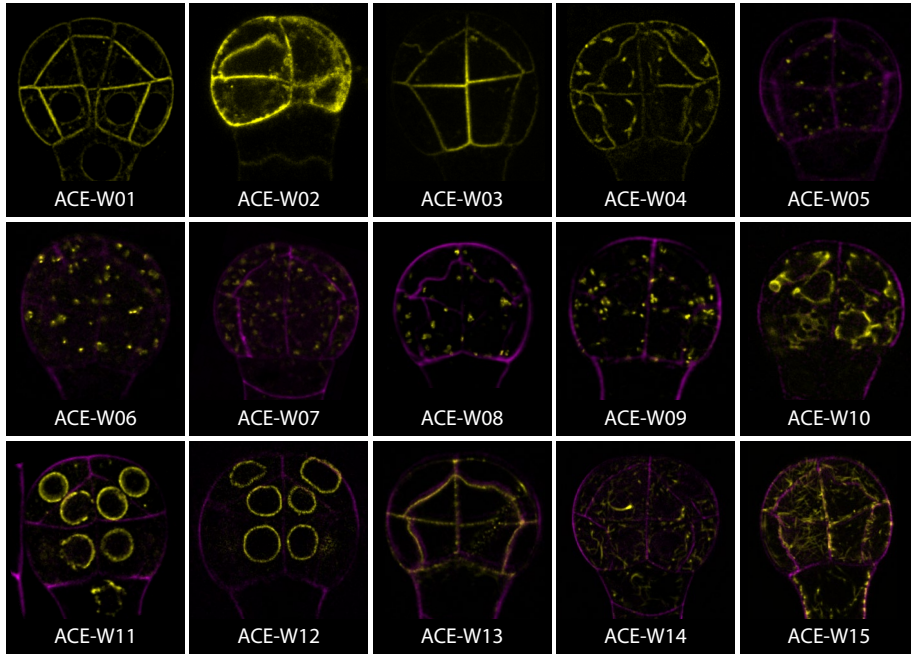
Supplementary Fig. 3. Overview of ACEs

Singe optical section showing cellular compartments labeled by corresponding markers in 16-cell embryos. Yellow: Fluorescent signal from the marker. Magenta: SR2200.

Step 1

Step 2

Step 3

Step 4

Step 5

Step 6

>8 mm

>8 mm

Step 7

Legend:

	75 x 26 microscope slide
	24 x 24 cover slip box
	EGM (general purpose) or EMTM (MT specific)
	EGC (general purpose) or EMTC (MT specific)
	50 x 24 cover slip
	200 µL pipette tip
	Contact/pressure point
	Do not press
	Arabidopsis seed
	Marked imaging area
	Stage clips
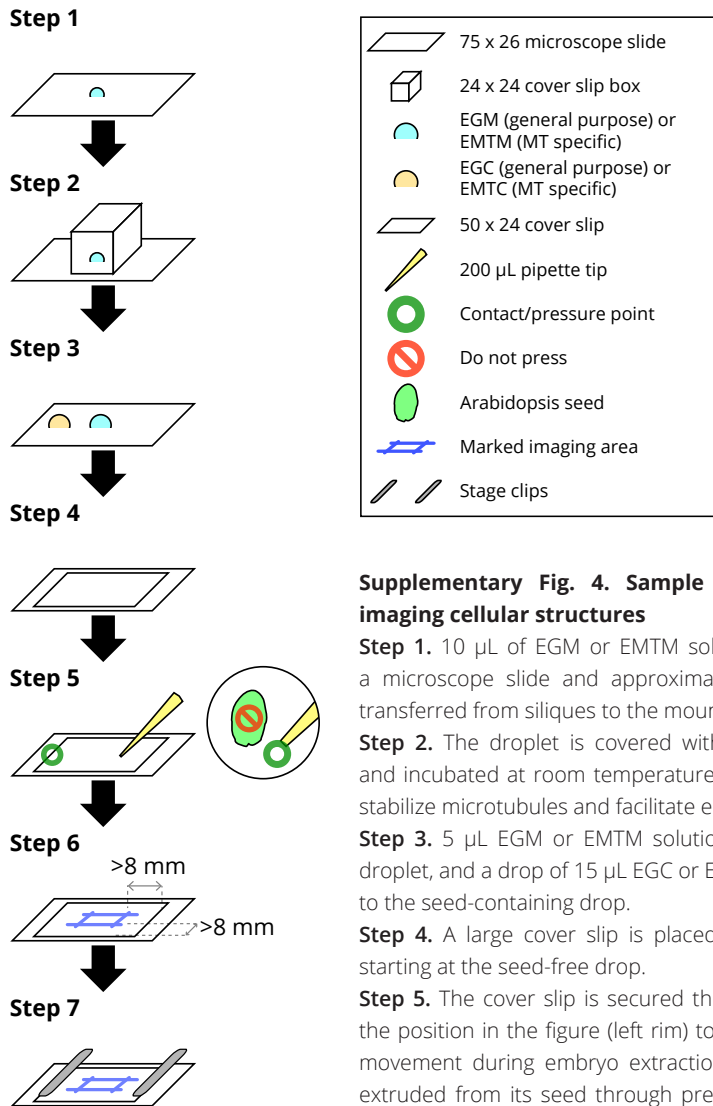
Supplementary Fig. 4. Sample preparation for imaging cellular structures

Step 1. 10 µL of EGM or EMTM solution is placed on a microscope slide and approximately 50 seeds are transferred from siliques to the mounting media.

Step 2. The droplet is covered with a cover slip box and incubated at room temperature for 15 minutes to stabilize microtubules and facilitate embryo extrusion.

Step 3. 5 µL EGM or EMTM solution is added to the droplet, and a drop of 15 µL EGC or EMTC is placed next to the seed-containing drop.

Step 4. A large cover slip is placed over both drops, starting at the seed-free drop.

Step 5. The cover slip is secured through holding it at the position in the figure (left rim) to prevent cover slip movement during embryo extraction. Each embryo is extruded from its seed through pressing around each seed with a 200 µL pipette tip under a stereo microscope as shown in the right panel. Do not directly press seeds to prevent seed and embryo damage.

Step 6. The imaging area is marked on the back-side of the slide to prevent the objective moving over the cover slip bringing water underneath the cover slip and changing the osmotic pressure of the mounting solution.

Step 7. The cover slip is secured with clips on the stage.

Step 1

10 mm

20 mm

Step 2

Step 3

>5 mm

Step 4

Step 5

Step 6

	75 x 26 microscope slide
	Single layer tissue
	Mock solution
	Arabidopsis seedling
	50 x 24 cover slip
	Stage clip
	200 µL pipette tip
	Double layer tissue
	Treatment solution
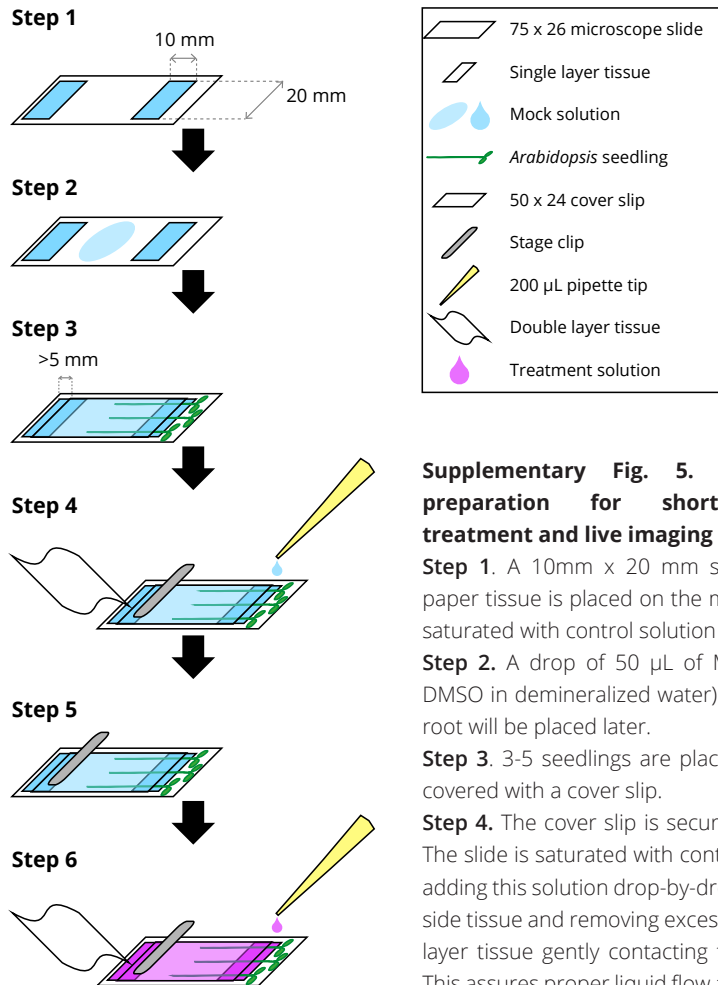
Supplementary Fig. 5. Seedling sample preparation for short-term chemical treatment and live imaging

Step 1. A 10mm x 20 mm single layer piece of paper tissue is placed on the microscope slide and saturated with control solution

Step 2. A drop of 50 µL of Mock solution (0.1% DMSO in demineralized water) is placed where the root will be placed later.

Step 3. 3-5 seedlings are placed as indicated and covered with a cover slip.

Step 4. The cover slip is secured with a stage clip. The slide is saturated with control solution through adding this solution drop-by-drop on the cotyledon-side tissue and removing excess liquid using double layer tissue gently contacting the root-side tissue. This assures proper liquid flow and prevents sample movement. Do not let solution overflow the slide.

Step 5. Imaging coordinates of all samples are set in the microscope software, and T=0 data is acquired.

Step 6. Set interval of time laps. Add >500 µL (or >10x the volume used in Step 2) treatment solution (Mock solution for negative controls or 10 µM Taxol solution from diluting 10 mM Taxol in 100% DMSO with demineralized water as Treatment solution for treatments) as described in Step 4. Replace double layer tissue frequently to assure proper liquid flow and replace all control solution with treatment solution within a minute. Mark the time as starting of T=1. Quickly go through all imaging coordinates and update the imaging coordinates if the sample is moved. When reaching T=1, start imaging. Keep the slide saturated through adding water drop-by drop on the single layer tissue if imaged over 30 minutes.

Chapter 5

AUXIN CONTROL OF CYTOSKELETON ORGANIZATION IN EARLY *ARABIDOPSIS* EMBRYOGENESIS

Che-Yang Liao, Thijs de Zeeuw, and Dolf Weijers

Laboratory of Biochemistry, Wageningen University, Wageningen, the Netherlands

Abstract

Pattern formation during early *Arabidopsis* embryogenesis is under tight control, ensuring invariant patterns of cell division in this species. Among the regulatory mechanisms, auxin response is prominent, controlling both division orientation and cell identity. At the 8-16 cell transition, auxin response triggers deviation in cell division orientation from a default that follows the shortest wall, thus defining an asymmetric division. A central question in plant biology is how genetic regulation instructs division orientation. Both microtubule (MT) and actin cytoskeleton are critical for plant cell division, but it is unclear if and how auxin response controls division orientation through these subcellular structures. Here we took the advantage of embryo-specific fluorescent markers for MT and actin cytoskeleton, as well as a conditional auxin response mutant with a consistently abnormal division pattern at the 8-cell stage. We find that impaired auxin response in the embryo affects both the MT and actin cytoskeleton at interphase. In contrast, mitotic and cytokinetic cytoskeletal structures are not regulated by auxin response. While mechanisms of cytoskeleton regulation are elusive, in part due to the difficulty in quantifying abnormalities in cytoskeletal structures in fixed embryos, this work defines a role for auxin in cytoskeleton control in the embryo, which should lead to the identification of molecular components in the future.

Introduction

During embryogenesis, the body plan of the seedling is first laid down, followed by further development. In the crucifer species *Arabidopsis thaliana*, the process of body pattern formation is accompanied by highly regular cell divisions that change little among individuals. Thus, control of cell division plane is likely an important aspect of development, and conversely, the *Arabidopsis* embryo is a good model to study the regulation of oriented cell division. Asymmetric cell division of the zygote results in the apical cell, which will then develop into the embryo proper, and the basal cell, which will then develop into the suspensor. Next, the apical cell conducts two sequential radial anticlinal cell divisions resulting in four equal embryo proper cells. In the following division of the 4-cell embryo, however, the division plane turns 90 degrees resulting in four upper and four lower tier embryo proper cells. The upper tier cells are the precursor of hypocotyl, cotyledons, and shoot apical meristem, while the lower tier cells will develop into the root. The division planes next turn 90 degrees again, and the resulting periclinal divisions in the upper and lower tier cells of the 8-cell embryo set apart the protoderm on the outside, and vascular/ground tissue precursor cells at the center of the newly formed 16-cell embryo [1].

The cell divisions from 4- to 16-cell embryos and onward are nearly synchronized in each embryo [2], and the orientation and position of each division plane is tightly controlled via various genetic pathways [3]. One of these regulatory mechanisms involves auxin response. This response centers on transcription factors - AUXIN RESPONSE FACTORS (ARFs)[4] - and the degradation of ARF inhibitors, INDOLE-3-ACETIC ACID, Aux/IAA proteins[5]. In the presence of the phytohormone auxin, Indole-3-Acetic Acid, Aux/IAA proteins are degraded[6, 7], thus releasing ARF's from inhibition [5]. A prime example of the antagonism of ARF and Aux/IAA proteins can be found in the loss of function mutation of ARF5, *monopteros* (*mp*)[8] and gain of function of Aux/IAA12, *bodenlos (bdl)*[9], which is not degraded with the presence of auxin [10]. Mutated embryos show an abnormal cellular pattern in 16-cell embryos and daughter cells of the lower tier cells and uppermost suspensor cell, the hypophysis, resulting in rootless embryos and seedlings [8, 9]. While the phenotype in 8-cell embryos were not with full penetrance in both mutants, similar phenotype could be achieved all embryos through the mis-expression of *bdl* driven by *Ribosomal Protein S5A* promoter (*pRPS5A*) through a conditional two-component gene expression system [11]. Instead of undergoing the periclinal division found in the wild type that requires the longest path for the division plane, the embryo proper cells in *pRPS5A>> bdl* 8-cell embryos divide radial anticlinally following a shortest-wall principle[12]. Auxin responses, therefore, allow to deviate cell division from the physics-driven shortest-wall principle to an exact orientation and position for proper pattern formation during early embryogenesis [12]. The machinery regulated by auxin responses to position the division plane in its designated orientation, however, remains unclear.

The important roles played by cortical microtubule (MT) arrays and actin architectures in cell shape and cell division have been well documented [13-15], and the underlying mechanisms of how these cytoskeletal organizations influence morphogenesis in epidermal tissues of various organs of *Arabidopsis* have begun to be revealed through quantitative analyses and computational simulation [16-20]. The organizations of MT array and actin network and the effect of auxin response on these cytoskeletal structures during embryogenesis however, have not yet been charted.

Here we applied embryo-specific MT and actin fluorescence markers [21] and utilized the *pRPS5A>>bdl* two-component system as a model for investigating the role of cytoskeletal organizations on pattern formation during early embryogenesis regulated by auxin responses. We found that while suppressed auxin responses had no effect on the establishment and orientation of preprophase bands and spindle, and the dynamic orientation of the MT array during interphase; the uniformity of MT orientation, stability of MT, and the formation of peri-nuclear actin arches were severely affected in *pRPS5A>> bdl* embryos during early embryogenesis. Our observations suggested that auxin responses influence the MT and actin cytoskeleton organization although the degree of such influence and the exact mechanism remain to be determined.

Results

Auxin response controls the interphase MT array

The crucial role of auxin in pattern formation during embryogenesis has been demonstrated through numerous mutants with defective auxin biosynthesis, transport, perception, and response [22]. However, the cell biology linking auxin responses to the precise position and orientation of cell division plane has remained unaddressed. To dissect the cellular machinery of auxin response-dependent pattern formation during embryogenesis, we combined a system in which consistently abnormal cell division can be induced by conditional suppression of auxin response, along with markers highlighting cellular structures[21]. We thus exploited the GAL4/*UAS* two-component gene expression system[23], in which abnormal but consistent changes in the cell division orientation of every cell in the embryo proper in every 8-cell embryos is induced by *bdl* expression through crossing *pRPS5A::GAL4:VP16* driver line with *UAS::bdl* operator line [11]. To highlight the MT, we introduced an established mGFP:AtTUA6 reporter, driven by the embryo-specific *pWOX2* promoter[21] into the *pRPS5A::GAL4:VP16* driver line.

Due to the requirement of crossing the *pRPS5A::GAL4:VP16* line with the *UAS::bdl* operator line, only one copy of the *pWOX2::mGFP:AtTUA6* transgene will be expressed in the F1 embryo. We first tested if marker heterozygosity impedes MT imaging. Indeed, we previously detected lower fluorescence intensity in a population of heterozygous mGFP:AtTUA6 embryos, compared to embryos from a homozygous line (unpublished). We next compared the mGFP:AtTUA6 fluorescence intensity and MT array between embryos derived from self-fertilized *pWOX2::mGFP:AtTUA6* homozygotes and F1 embryos derived from a cross with non-transgenic Col-0 wild type. While the fluorescence intensities in homozygous embryos seemed higher than heterozygous F1 embryos, no visible difference in MT organization were observed (Fig. 1a). The reduced mGFP:AtTUA6 expression in heterozygous embryos, therefore, was still sufficient to label the overall MT arrays using our previously established imaging protocol [21].

If auxin response controls the MT cytoskeleton, this could be manifested at various levels in *bdl*-expressing embryos: One mode could be that the interphase MT network is correctly patterned and leads to the correct pre-prophase band (PPB), but the mitotic spindle does not follow the PPB position. Another mode could be that defects occur earlier – in interphase – and the mitotic and cytokinetic machineries follow an incorrectly places PPB. Thirdly, it could be that all MT structures are deregulated, and finally, it is also possible that *bdl* expression alters cell division plane without affecting the MT cytoskeleton.

To distinguish between these modes, we first examined whether spindle and preprophase band (PPB) were present and if their orientations were consistent with the wild type division orientation, or with the expected division orientation in *pRPS5A>>bdl*
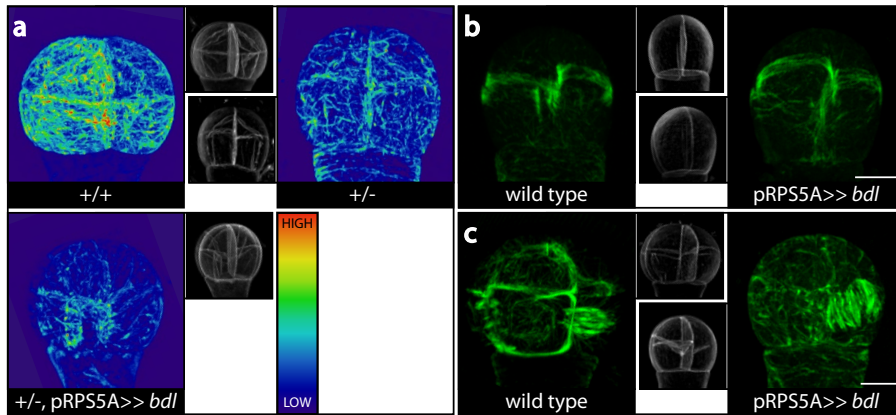
Fig. 1. *pWOX2::TUA6:mGFP* expression and mitotic microtubule structures in early embryos from wild type and *pRPS5A>>bdl* background.

(a) Maximum intensity projection of microtubule array in 16-cell embryos from *pWOX2::TUA6:mGFP* expression homozygote (+/+), heterozygote resulted from crossing with wild type (+/-) and heterozygote resulted from crossing with *UAS:: bdl* (+/-, *pRPS5A>>bdl*). LUT shows color values corresponding to fluorescence signal intensity in the maximum intensity projections. (b, c) Maximum intensity projection of 4-cell (b) and 8-cell (c) embryos with preprophase bands and spindles in wild type and pRPS5A>>*bdl* background. Insets show the cellular contours of corresponding embryos. All images were acquired with same acquisition settings. Scale bar: 5 µm.

embryos at 4- and 8-cell stage. Both spindle and PPB of MT aligned perfectly with the mutant cell division plane, and thus clearly deviated from the wild type orientation in 8-cell *pRPS5A>>bdl* embryos (Fig. 1b,c). This indicates that suppressed auxin response had no effect on the machinery executing mitosis and cytokinesis. Thus, either the effect of auxin response inhibition is independent of MT's, or else its effect must be prior to PPB formation, in interphase.

Since the PPB is derived from condensed cortical MT's during interphase, we next asked if MT organization during interphase was affected in *bdl*-expressing embryos. When observing MT patterns in interphase cells in 4-cell and 8-cell *bdl*-expressing embryos, no striking differences in the MT patterns were found between wild type and *bdl*-expressing embryos (Fig. 2a-c). However, the MT mesh is a complex network defined by the number, length and orientation of its constituent filaments, as well as by their dynamic properties. No dynamics can be studied in embryos cells with Taxol-stabilized MT array, but we analyzed topological properties using an unbiased approach. MT orientation and anisotropy were determined in each cell through analyzing maximum projections of embryos with their radial anticlinal cell walls perpendicular to the focal plane using the Fibriltool software [24]. In 4-cell embryos, where only transverse anticlinal division were expected in both wild type and *pRPS5A>>bdl* background [12], no significant difference in MT orientations or anisotropy were found between wild type and *pRPS5A>>bdl* embryos (Table 1). However, two categories of MT orientations were found in both wild type and pRPS5A>>*bdl* 4-cell embryos with the majority of MT orientations running parallel to the radial anticlinal cell wall, and in rare cases the MT orientation ran parallel to the transverse anticlinal wall (Fig. 2a,b). The cells whose MT orientation aligned with the transverse anticlinal wall were coupled to sister cells with a visible PPB or spindles (Fig. 2b). In 8-cell embryos where all embryo cells divide periclinally in wild type, but radial anticlinally in *pRPS5A>>bdl* background [12], similar MT orientations were found (Fig. 2c). MT orientation ran parallel to the transverse anticlinal cell wall during interphase, while MT orientation ran parallel to the radial anticlinal cell wall prior to the formation of a PPB, without significant differences in MT orientations between the two genetic backgrounds (Fig. 2d, e, Table 1). The MT anisotropy in *pRPS5A>>bdl* 8-cell embryos, however, was significantly lower than in wild type embryos (Table 1). In addition to the reduced uniformity of microtubule in *pRPS5A>>bdl* 8-cell embryo, a significantly higher frequency of microtubule depolymerization (Table 2) and higher level of background fluorescence signal in the cytosol (Table 3) was found. This suggests either reduced polymerization or increased depolymerization and reduced MT stability in *bdl*-expressing embryos.

We thus conclude that instead of regulating the mitotic and cytokinetic MT structures, auxin responses control interphase MT dynamics through yet unknown mechanisms.
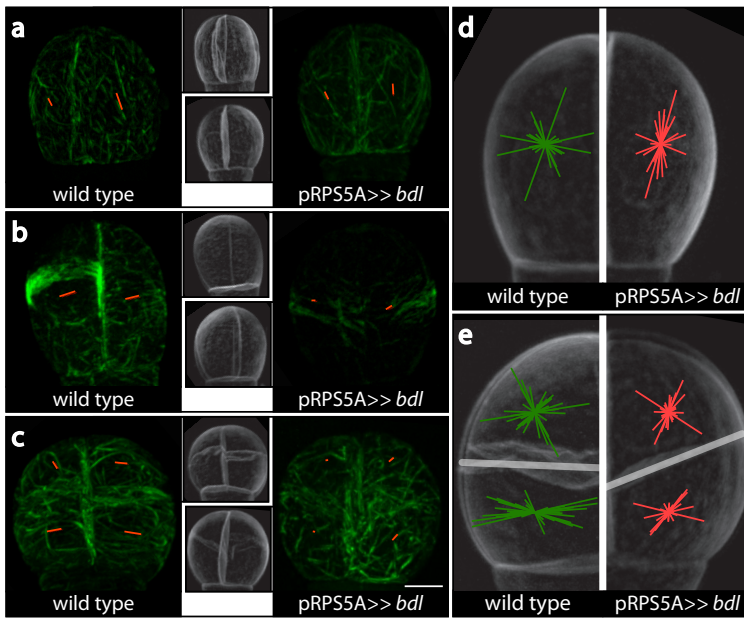
Fig. 2. Microtubule orientation and anisotropy in 4- and 8-cell embryos from wild type and *pRPS5A>>bdl* background.

(a, b) Maximum intensity projection of microtubule arrays with microtubule orientations and anisotropy in 4-cell embryos at interphase (a) and with at least one preprophase band (b). (c)Maximum intensity projection of microtubule arrays with microtubule orientations and anisotropy in 8-cell embryos at interphase. (d, e) Projection of all quantified microtubule orientation and anisotropy in 4- (d) and 8-cell (e) embryos. Microtubule orientation and anisotropy of preprophase band were excluded. Insets show the cellular contours of corresponding embryos, and direction and length of the red/green lines indicated microtubule orientation and anisotropy, respectively. All images were acquired with same acquisition settings. Scale bar: 5 μm.

Table 1. Microtubule orientation and anisotropy in each cell in 4- and 8-cell embryos

	Relative microtubule orientation (°)			Anisotropy		
	4-cell	8-cell, upper tier	8-cell, lower tier	4-cell	8-cell, upper tier	8-cell, lower tier
Wild type	111.43± 46.66 (n= 18)	86.57± 48.90 (n= 20)	101.84± 22.39 (n= 20)	0.05± 0.04 (n= 18)	0.05± 0.03 (n= 20)	0.07± 0.04 (n= 20)
pRPS5A>>*bdl*	101.28± 64.71 (n= 12)	108.09± 53.44 (n= 18)	115.41± 43.93 (n= 18)	0.06± 0.03 (n=12)	0.03± 0.02 (n= 18)	0.03± 0.02 (n= 18)
p-value*	6.43E-01	2.05E-01	2.46E-01	6.50E-01	3.88E-02	3.58E-04

* Two-tail student t-test

Table 2. Frequencies of microtubule array depolymerization observed in 8-cell embryos

	Intact	Depolyermized	Total
Wild type	41	18	59
pRPS5A>>*bdl*	32	58	90
Total	73	76	149
p-value*	5.06E-05		

* Pearson's chi-squared test

Table 3. Cytosolic mGFP: TUA6 signal in each cell of 8-cell embryos

	Signal intensity
Wild type	10.82± 4.42 (n= 148)
pRPS5A>>*bdl*	17.08± 6.70 (n=132)
p-value*	1.57E-17

* Two-tail student t-test

Auxin response contributes to peri-nuclear Actin localization

Cell division site selection involves interplay between the MT and actin cytoskeleton [25-28]. After establishing that auxin response inhibition has subtle but measurable effects on the interphase MT network, we asked if the actin cytoskeleton is subject to regulation by auxin response. We thus introduced the embryo-specific Actin reporter *pWOX2::Lifeact:tdTomato* [21] into the *pRPS5A::VP16:GAL4* driver line. Despite weaker fluorescence intensity in F1 embryos obtained after crossing the *pRPS5A::GAL4:VP16 pWOX2::Lifeact:tdTomato* line to wild type compared to homozygous controls, no distinguishable difference in the labelled actin network were identified (Fig. 3). The peri-nuclear arches, however, were absent in one third of the embryos from the driver line despite their higher fluorescence intensity and thicker appearance (Fig. 3, Table 4).
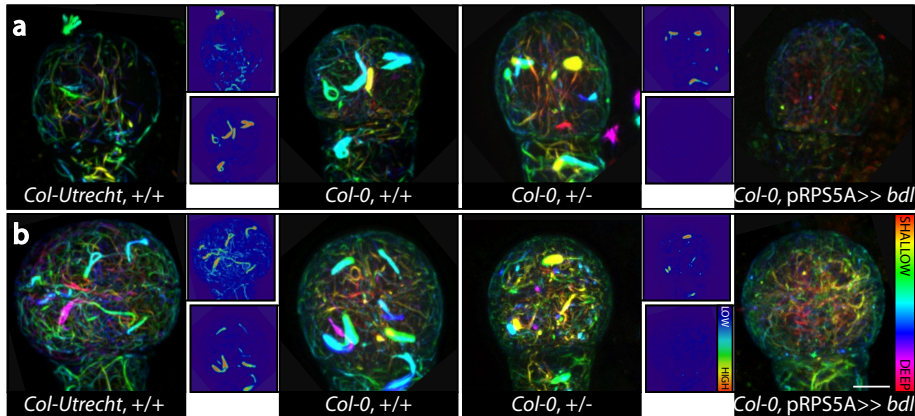
Fig. 3. Actin architectures in 4- and 8-cell embryos from embryos from wild type and pRPS5A>>*bdl* background

(a, b) Maximum intensity projection of actin meshwork and peri-nuclear arches in 4- (a) and 8-cell (b) embryos. Insets show the fluorescence intensity from the raw image of corresponding embryos. LUT in the insets and main panels show color values corresponding to depth of image in z-dimension and fluorescence signal intensity in the maximum intensity projections, respectively. All images were acquired with same acquisition settings. Scale bar: 5 μm.

Upon comparing the Actin architecture in wild type and *pRPS5A>>bdl* embryos, our first discovery was the lower overall fluorescence intensity of the actin meshwork and higher cytosolic signal in *pRPS5A>>bdl* embryos (Fig. 3). This suggests, like in the case of the MT cytoskeleton described above, a reduced stability of actin polymers or decreased polymerization. The other visible effect of suppressed auxin response was the complete loss of the peri-nuclear actin arches in *pRPS5A>>bdl* embryos (Fig. 3, Table 4). While the role of these structures remains unknown, their absence in embryos with suppressed auxin responses demonstrates an alteration in actin organization.

Table 4. Frequencies of peri-nucleus actin arches observed in 8-cell embryos

	Present	Absent	Total
Wild type	9	4	13
pRPS5A>>*bdl*	0	13	13
Total	9	17	26
p-value*	2.07E-04		
* Pearson's chi-squared test			

Discussion

In this chapter, we examined cytoskeletal structures in early embryos with and without abnormal cell patterning resulted from suppressed auxin responses. Our observations revealed that suppressed auxin responses had no effect on the formation of PPB or spindles, nor their orientations relative to the expected cell division orientation. However, auxin response inhibition did result in reduced interphase MT uniformity, increased MT depolymerization rate upon embryo extraction, and loss of peri-nuclear actin arches. The less organized and easily depolymerized MT arrays in embryos with suppressed auxin responses suggested impaired microtubule stability. Indeed, similar effects on MT had been reported in mutants hypersensitive to the tubulin-specific MT depolymerization drug Oryzalin, in various mutants in MT-associated proteins: some of these are directly involved in the establishment and position of cytokinetic machineries, like PPB and phragmoplast [29-33]. In others, there is only a moderate cell shape change in non-dividing cells [34-40]. Thus, decreased MT stability can affect both cell shape and cytokinesis. However, unlike loss of function mutants of MT-associated proteins that are usually coupled with failure in the establishment of PPB and spindles, or random cell division patterns, not only no abnormal cell shape and impaired nor mis-oriented mitotic and cytokinetic structures were found in embryos with suppressed auxin responses, but the alternative cell division pattern in 8-cell embryos with suppressed auxin responses was as consistent as the wild type cell division pattern. This suggested that if auxin responses regulate cell division pattern during early embryogenesis though regulating microtubule organization, it is likely through actively fine-tuning the MT or/and actin organization in interphase, via the expression levels of MT-associated proteins for example, to deploy markers defining the position of PPB and cortical division zone, or to moderate overall cytoskeleton organization and cell shape or dimension.

While our quantifications of MT orientation relative to the radial anticlinal wall during interphase showed no significant difference between embryos with and without suppressed auxin responses, three factors could lead to false negative results. Firstly, the various MT array orientations we observed were pooled for our analysis. If 8-cell embryo cells follow the 90 degrees shift of the MT array before the establishment of the PPB as observed in 4-cell embryos, cells will need to be categorized according to their developmental stages. The developmental stage can be identified via including cell cycle markers or live imaging. Secondly, our quantitative analyses of MT arrays were conducted through maximum projections of image stacks, which contain both radial and transverse faces of the embryo close to the right angle to the focal plane. This approach did not only limit the amount of viable image stacks for quantification analysis, but also made it impossible to separate the MT array on the peripheral cell face from that on the radial anticlinal cell face, and in addition the spatial information from the z-axis was lost. While the spatial information from the third dimension might be insignificant or even trivial in cell with flat or tubular shape, spatial information from

all three dimensions would be equally important in cells with polygonal shape in the early embryo. This issue can be circumvented via acquiring image stack of given sample from different angles to achieve isometric resolution in all three axes computationally adapt software to incorporate and analyze the information from the third axis. Thirdly, the lack of information from transverse anticlinal cell face. While it is plausible that the cortical MT arrays on both radial anticlinal cell faces are similar, the cortical MT array on the transverse anticlinal cell face may be different. In addition, with the MT array on peripheral and radial anticlinal cell faces in the longitudinal orientation before the formation of PPB of MT, whether the orientation of the cortical microtubule array on the transverse anticlinal cell face is parallel or vertical to the radius on the same cell face may reveal the difference in MT organization between embryos with or without suppressed auxin responses. To reliably acquire the organization of cortical MT array on the transverse anticlinal cell face, acquiring image stack of given sample from different angles to achieve isometric resolution in all three axes computationally will be necessary due to the low possibility of embryo in the favorable orientation with the transverse anticlinal cell face parallel to the focal plane.

Unlike the seemly minor effect of suppressed auxin responses on MT arrays, complete loss of the peri-nuclear actin arches was observed in embryos with suppressed auxin responses suggesting a link between auxin response and actin architectures during embryogenesis. With the unknown function of the peri-nuclear actin arches and their relation to cell division, however, whether and how auxin responses directly regulated pattern formation via affecting actin architectures remain to be determined. Nonetheless, the finding that a major actin structure is altered or missing in *bdl*-expressing embryos suggests that auxin response controls the expression of proteins that modulate actin polymerization or stability. There is a precedent for auxin to control the actin cytoskeleton through ROP/RIC signaling [41]. However, in this case the auxin is proposed to be perceived extracellularly through a different response system [42]. It will be interesting to see if and how such auxin-dependent Actin control mechanisms intersect.

So far, various approaches, from genetics, transcriptomics, cell geometry to the recently developed computational simulation have been implemented to dissect the underlying mechanism regulating pattern formation during early embryogenesis and have expanded our knowledge on this topic in various ways. On the other hand, the advance in cell biology through the advance of microscopy and computational analyses has provided profound foundation to understand and predict the dynamics of cellular structures and their effects on cell morphology and division. The effects on cytoskeletal organizations in genetically regulated cell division and our application of computational analysis on the MT arrays offered a starting point to integrate multidisciplinary to further understand how the upstream regulatory mechanisms influence downstream cellular structures implementing the signals to precise patterning.

Materials and Methods

Plant and embryo material

pGIIN/pWOX2::mGFP:TUA6:tNOS and *pGIIN/pWOX2::Lifeact:tdTomato:tNOS* [21] were introduced into homozygous pRPS5A::GAL4:VP16 driver line establish in *Arabidopsis thaliana* ecotype Col-0 [11] through floral dip [43]. T1 transgenic plants were selected with Norflurazon (Supelco)[44], and T3 homozygotes transgenic plants with representative expression level that uniformly labeling their corresponding cellular structures were selected for crossing in this study.

Evaluations of embryo development after pollinated by Col-0 wild type plant or homozygous UAS::*bdl* operator line established in Col-0 [11] were conducted as described [45]. 8-cell embryos were most predominant in 74 hours post-pollination in (pRPS5A::GAL4:VP16/ *pWOX2::mGFP:TUA6:tNOS*) x (Col-0), 80 hours post-pollination in (pRPS5A::GAL4:VP16/ *pWOX2::mGFP:TUA6)* x (UAS::*bdl*), 72 hours post-pollination in (pRPS5A::GAL4:VP16/ *pWOX2::Lifeact:tdTomato)* x (Col-0), and 80 hours post-pollination in (pRPS5A::GAL4:VP16/ *pWOX2::Lifeact:tdTomato)* x (UAS::*bdl*) and were used for imaging and analysis.

In each cross, 4 individuals from the driver/marker line were first crossed with Col-0. After data were collected from the consequential wild type embryos, the same 4 individuals were crossed with UAS::*bdl* operator line to generate *pRPS5A>>bdl* embryos for data collection. All data used in this study were collected from 3 batches of independent crosses.

Microscopy and image analysis

Embryos were mounted and imaged as described [21]. Images were acquired in 8-bit format using a Leica TCS SP5II confocal laser scanning microscope with 63× NA = 1.20 water-immersion objective with pinhole set to 1.0 Airy Unit. mGFP by Argon-ion laser, tdTomato, and SCRI Renaissance Stain 2200 (SR2200) (Renaissance Chemical) were excited using a diode laser, and their emissions were detected sequentially with Leica HyD in photon counting mode. Excitation and detection of fluorophores were configured as follows: mGFP was excited at 488 nm and detected at 498–528 nm; tdTomato was excited at 561 nm and detected at 571–630 nm; Renaissance 2200 was excited at 405 nm and detected at 430–470 nm. 0.25 µm interval between each optical section were used in image stacks. To prevent photo bleaching, 488 and 561 lasers were set to minimal that fluorescence intensities in PPB, spindle, and peri-nuclear actin arches were lower than 200, and 405 laser was set to 1%. To accelerate image acquisition, scan frequency was set to 700 Hz, only line accumulation was applied and was set to 4, 4, and 2 for mGFP, tdTomato, and SR2200, respectively. Neither frame accumulation nor average were applied.

For qualitative descriptions of microtubule and actin architectures, maximum projection of given image stack was generated to determine the average background fluorescence signal intensity outside of the embryo for subtraction from the image stacks. After the removal of background fluorescence from the image stack, the fluorescence signals of the whole image stack were globally multiplied by 2 or 4 times, depended on the presence of PPB, spindle, or peri-nuclear actin arches, for visualization.

For quantitative analysis of microtubule orientation and anisotropy, raw image stacks containing embryo with radial and transvers anticlinal cell faces close to vertical to the focal plane were used and analyzed via Fibriltool with default setting [24]. The relative microtubule orientations were defined as the angle between radial anticlinal cell face and the microtubule orientation determined by Fibriltool. The differences in average relative microtubule orientations and anisotropy were tested via two-tailed student t-test with MS Excel™.

For comparison of the frequencies of microtubule depolymerization and loss of perinuclear actin arches, the frequencies of given observation were determined by the number of given observation divided by the number of overall extracted embryos which showed no morphological disturbance from the extraction process. The differences in frequencies were tested via Pearson's chi-square test with MS Excel™.

For measurement of cytosolic mGFP: TUA6 signal in individual cells, the optical section containing the great circle of the nucleus was visually defined, a maximum projection containing 5 optical sections, 2 above, 2 beneath the optical section with the great circle, and the optical section containing the great circle, was then generated from the raw image stack. A 0.2 to 0.4 μm^2 region of interest (ROI) in the cell of interest was given at where no distinguishable microtubule structure was found. The average mGFP fluorescence signal intensity in this ROI was documented and defined as the cytosolic mGFP: TUA6 signal of the cell of interest. The difference in average cytosolic mGFP: TUA6 signals were tested via two-tailed student t-test with MS Excel™.

All image processes and measurements were conducted via Fiji[46].

References

1. Wendrich, J.R. & Weijers, D. *New Phytol.* **199**, 14-25 (2013).
2. Mansfield, S.G. & Briarty, L.G. *Canadian Journal of Botany* **69**, 461-476 (1991).
3. Ten Hove, C.A., Lu, K.J. & Weijers, D. *Development (Cambridge)* **142**, 420-430 (2015).
4. Ulmasov, T., Hagen, G. & Guilfoyle, T.J. *Proc Natl Acad Sci U S A* **96**, 5844-5849 (1999).
5. Tiwari, S.B., Wang, X.J., Hagen, G. & Guilfoyle, T.J. *Plant Cell* **13**, 2809-2822 (2001).
6. Gray, W.M., Kepinski, S., Rouse, D., Leyser, O. & Estelle, M. *Nature* **414**, 271-276 (2001).
7. Zenser, N., Ellsmore, A., Leasure, C. & Callis, J. *Proc Natl Acad Sci U S A* **98**, 11795-11800 (2001).
8. Berleth, T. & Jurgens, G. *Development* **118**, 575-587 (1993).
9. Hamann, T., Mayer, U. & Jurgens, G. *Development* **126**, 1387-1395 (1999).
10. Dharmasiri, N. et al. *Dev. Cell* **9**, 109-119 (2005).
11. Rademacher, E.H. et al. *Dev. Cell* **22**, 211-222 (2012).
12. Yoshida, S. et al. *Dev. Cell* **29**, 75-87 (2014).
13. Rasmussen, C.G., Wright, A.J. & Muller, S. *Plant J.* **75**, 258-269 (2013).
14. Li, S., Sun, T. & Ren, H. *Front Plant Sci* **6**, 282 (2015).
15. Ivakov, A. & Persson, S. *Front Plant Sci* **4**, 439 (2013).
16. Louveaux, M., Julien, J.D., Mirabet, V., Boudaoud, A. & Hamant, O. *Proc Natl Acad Sci U S A* **113**, E4294-4303 (2016).
17. Louveaux, M., Rochette, S., Beauzamy, L., Boudaoud, A. & Hamant, O. *Plant J.* **88**, 328-342 (2016).
18. Yanagisawa, M. et al. *Nature Plants* **1** (2015).
19. Shi, X.Q. & Ma, Y.Q. *Proc Natl Acad Sci U S A* **107**, 11709-11714 (2010).
20. Elliott, A. & Shaw, S.L. *Plant Physiol.* **176**, 307-325 (2018).
21. Liao, C.Y. & Weijers, D. *Plant J.* **93**, 963-976 (2018).
22. Smit, M.E. & Weijers, D. *Curr. Opin. Plant Biol.* **28**, 99-105 (2015).
23. Moore, I., Gälweiler, L., Grosskopf, D., Schell, J. & Palme, K. *Proceedings of the National Academy of Sciences of the United States of America* **95**, 376-381 (1998).
24. Boudaoud, A. et al. *Nat Protoc* **9**, 457-463 (2014).
25. Wu, S.Z. & Bezanilla, M. *eLife* **3** (2014).
26. Kimata, Y. et al. *Proc Natl Acad Sci U S A* **113**, 14157-14162 (2016).
27. Lloyd, C.W. & Traas, J.A. *Development* **102**, 211-221 (1988).
28. Kojo, K.H. et al. *Plant Cell Physiol.* **54**, 1491-1503 (2013).
29. Müller, S. et al. *Curr. Biol.* **14**, 412-417 (2004).
30. Smertenko, A.P. et al. *Plant Cell* **16**, 2035-2047 (2004).
31. Azimzadeh, J. et al. *Plant Cell* **20**, 2146-2159 (2008).
32. Spinner, L. et al. *Nature Communications* **4** (2013).
33. Kirik, A., Ehrhardt, D.W. & Kirik, V. *Plant Cell* **24**, 1158-1170 (2012).
34. Rosero, A. et al. *Plant Cell Physiol.* **57**, 488-504 (2016).
35. Bhaskara, G.B., Wen, T.N., Nguyen, T.T. & Verslues, P.E. *Plant Cell* **29**, 169-191 (2017).

36. Walia, A., Lee, J.S., Wasteneys, G. & Ellis, B. *Plant J.* **59**, 565-575 (2009).
37. Naoi, K. & Hashimoto, T. *Plant Cell* **16**, 1841-1853 (2004).
38. Mir, R., Morris, V.H., Buschmann, H. & Rasmussen, C.G. *Plant Physiol.* **176**, 418-431 (2018).
39. Mei, Y., Gao, H.-B., Yuan, M. & Xue, H.-W. *The Plant Cell Online* (2012).
40. Sambade, A., Findlay, K., Schäffner, A.R., Lloyd, C.W. & Buschmann, H. *Plant Cell* **26**, 1629-1644 (2014).
41. Wu, H.M., Hazak, O., Cheung, A.Y. & Yalovsky, S. *Plant Cell* **23**, 1208-1218 (2011).
42. Xu, T. et al. *Science* **343**, 1025-1028 (2014).
43. Davis, A.M., Hall, A., Millar, A.J., Darrah, C. & Davis, S.J. *Plant Methods* **5** (2009).
44. Misawa, N. et al. *Plant J.* **4**, 833-840 (1993).
45. Palovaara, J. et al. *Nat Plants* **3**, 894-904 (2017).
46. Schindelin, J. et al. *Nat. Methods* **9**, 676-682 (2012).

Chapter 6

GENERAL DISCUSSION

General Discussion

A unique feature of pattern formation in plant development is the lack of cell mobility due to encapsulation in the cell wall. Thus, the pre-mitotic orientation and position of the cell division plane directly determine cell pattern and 3-dimensional organ and tissue morphology. Hence, precise control over the exact orientation and placement of cell division is crucial for plant development to achieve morphologies required for proper tissue function. The cellular patterns observed in plant tissues have long captivated scientists, and have been the inspiration for developing theories and models for the underlying physical/biochemical basis of cell division orientation. Various works since the 19th century have explored the underlying principles to explain how cell division plane orientation and position are determined, and have invoked cell geometry, wall surface area, angles relative to pre-existing walls, among other parameters[1-4]. Through elaborating Errera's analogy between plant cell division and soap bubbles, Besson and Dumais formulated that the determination of cell division plane is a stochastic process with competing alternative cell division planes – each with local minimal surface area. It was shown that this principle can be applied to a wide range of plant systems[5]. This universal rule for division plane determination, however, appears to be violated at early embryogenesis in *Arabidopsis thaliana*. The first three symmetric cell divisions in the embryo proper follow Besson-Dumais' rule of division plane determination. This results in an isodiametric embryo proper consisting of eight cells. However, the following cell division orientation consistently deviated from Besson-Dumais' rule[6], generated an asymmetric division and established inner and outer cell layers. This deviation from Besson-Dumais' rule requires intact auxin response, as embryos with suppressed auxin responses revert back to the symmetric cell division following Besson-Dumais' rule[6]. However, the mechanism underlying this auxin-regulated oriented cell division remained elusive. This question was the starting point for the work described in this thesis. The work focused on the challenges and hurdles that precluded understanding the auxin-dependent control of cell division orientation in the embryo. Firstly, tools to visualize auxin activity in the embryo were lacking and secondly, no tools were available to visualize cellular structures and organelles in the embryo.

New tools for visualizing auxin action

To understand the regulation of cellular processes, such as cell division orientation, by the phytohormone auxin, it is critical to observe where and when the hormone accumulates and triggers gene expression responses. Reporters had previously been developed for both these purposes, but each suffered from shortcomings. For auxin-dependent gene expression, the most common reporter was *DR5*, based on a repeat of the *TGTCTC* ARF binding site[7]. In structural biochemical analysis of ARF-DNA binding, our team discovered that the *TGTCTC* element is in fact not a high-affinity binding site,

and the preferred site is *TGTCGG* instead[8]. It was thus likely that *DR5* reporters were only revealing the sites with auxin maxima.

For inferring auxin accumulation, the standard reporter was DII-Venus, a fragment of an Aux/IAA protein that is degraded in the presence of auxin[9]. While very useful, it is very difficult to use this reporter for comparisons between cells or individuals, as there is no control for the fluorescence intensity in the absence of auxin-dependent degradation. In addition, the available DII-Venus lines[9] used the *35S* promoter, which is not active in the early *Arabidopsis* embryo.

Given these limitations in visualizing auxin activity in the *Arabidopsis* embryo, in **Chapter 2**, I describe the development and evaluation of two prototypes of novel auxin reporters. The *DR5v2* reporter is a redesign of the *DR5* promoter, using the high-affinity ARF binding site *TGTCGG*. This indeed offered higher sensitivity and responsiveness for gene activating auxin response.

The R2D2 reporter was an upgrade of the DII-VENUS system[10] in which the DII probe and the auxin-insensitive mDII control were combined in the same locus to enable ratiometric, semi-quantitative measurement of auxin perception. In addition, both were expressed from the embryo-active *RPS5A* promoter[11]. *DR5v2* showed higher sensitivity that were able to response to lower auxin concentration with additional higher responsiveness that gives higher transcriptional output at the same auxin concentration compared to *DR5*. These advantages led to *DR5v2*'s ability to visualize auxin output maxima that were thus far only predicted via computational simulations based on auxin transport patterns. While reporter like *DR5* and *DR5v2* rely on the activation of the reporter genes such as fluorescent protein, they can only report the transcriptional activation resulting from auxin signaling. R2D2 circumvented this disadvantage as it reflects auxin perception based on protein degradation independent of transcriptional regulation. Thus, R2D2 revealed auxin perception maxima in tissues with suppressed auxin responses but with high auxin input. Such cases had been predicted through computational simulations based on auxin transport and our observations supported the existence of an auxin gradient in the root apical meristem. Recently, these prototypes were applied in various studies and revealed differential amplitudes in auxin signaling in tissues within the early embryo[12], roles of auxin production of endosperm in seed development[13, 14], developmental boundary defined by auxin minimum in root apical meristem[15], and auxin distribution on cell polarity in shoot apical meristem[16]. These applications did not only demonstrate the capability of these new auxin reporters, but also broaden the spectrum of question in auxin biology that can be enquired in vivo.

While the *DR5v2* and R2D2 prototypes described in **Chapter 2** were strong improvements relative to existing tools, and enabled new questions to be addressed, we noted their limitations and aimed to resolve in further developments described in **Chapter 3**.

In the original R2D2 version (Chapter 2), the two DII reporters were expressed from the RPS5A promoter, active in the early embryo and dividing cells, but not in more mature and differentiated tissues[10]. Therefore, R2D2 components were expressed from the ubiquitous UBI10 promoter to extend its application from dividing cells to almost all tissues and differential state of cells. In addition, we combined R2D2 with *DR5v2* driving a third fluorescent protein, thus leading to the first comprehensive auxin reporter, C3PO, which allows simultaneous observation of both auxin perception and response in the same cells. Unfortunately, strong expression of the *UBI10*-driven R2D2 (R2D2-U) caused dwarfism - likely due to saturating the auxin perception machinery. However, despite this limitation, the C3PO reporter allowed to make the surprising discovery that there is profoundly different capacity of auxin signaling among tissues and differentiation states. While some cells show high levels of auxin input, they hardly activate *DR5v2*, other cells show the opposite: high *DR5v2* activity despite little detectable auxin input. Likely, such differences are caused by differential expression of the core auxin signaling components (TIR1/AFBs; Aux/IAAs; ARFs). Indeed, members of the ARF family are strongly differentially expressed[17, 18], and the same is likely true for the Aux/IAA and perhaps the TIR1/AFB family. While this finding reveals interesting discrepancies, it also highlights a potential issue with the use of biosensors that utilize the internal cellular machinery. If sensors are to be used to define differences in hormone levels or response, such would always depend on the biological context of each cell, and the difference in response capacity between cells will need to be considered when interpreting the readout of the biosensors. Therefore, the next steps in the advancement of auxin reporters will be to develop auxin reporters that could also highlight negative (repressive) auxin responses, but also explore the possibility of auxin reporters that could directly reveal auxin molecules without relying on endogenous cellular machinery.

Auxin response in the arf5/mp mutant

A motivation for developing improved tools for auxin response visualization was to define the spatial-temporal changes in auxin response in mutants in the auxin pathway that affect cell division. In Chapter 3, we used the improved *DR5v2* reporter to map auxin response output in the *arf5/mp* mutant embryos. The ARF5/MP protein is critical for embryonic root formation[19, 20], but the pattern of auxin response in the mutant embryos had not yet been reported in high resolution, due to the limitations of the previously existing *DR5* reporter. The inability to form an embryonic root in the

mp mutant is correlated with altered division orientation in the hypophysis. It was previously showed that hypophysis division requires subsequent auxin responses in the proembryo cells adjacent to the hypophysis and in the presumptive hypophysis[21]. Because MP promotes expression of the auxin transport protein PIN1, as well as the mobile TMO7 transcription factor[22], both proembryo and hypophysis auxin responses are expected to be reduced in the *mp* mutant, but this had not yet been shown.

Using the increased sensitivity of *DR5v2*, we could now demonstrate that auxin response output was indeed clearly reduced in proembryo cells as well as the presumptive hypophysis prior to changes in cell division. MP is one of the five Class-A ARFs in *Arabidopsis*, that are thought to activate target genes[23] and plays a crucial role in root establishment in early embryogenesis[20]. Interestingly, while the *mp* allele used here is believed to be a null, some *DR5v2* activity remained in the *mp* mutant, which reveals contributions of other ARFs to auxin response at early embryo stages. In addition, *DR5v2* activity was strongly increased in the abnormal heart stage *mp* mutant embryos, possibly reflecting the inability to activate PIN transporters and to drain auxin from sites of production. Nonetheless, also this shows that other gene-activating ARFs must act in the embryo. Hence, the initial use of the novel *DR5v2* reporter unequivocally demonstrated reduced auxin response output in both proembryo and hypophysis cells in the *mp* mutant. Interestingly, both proembryo and hypophysis cells in the *mp* mutant also show alterations in cell division orientation, and thus this analysis fortifies the link between auxin response and cell division orientation.

New tools for observing cellular reorganization in the early embryo

With the evidence that auxin response is causally linked to cell division orientation, a key question is what cellular mechanisms underlie such control. This question was however difficult to address because virtually no tools were available to visualize the subcellular structures that contribute to division orientation during early embryogenesis. Therefore, in **Chapter 4**, we describe the development of a comprehensive set of fluorescent probes, expressed from the embryo-specific *WOX2* promoter. These ACE lines are perfectly suited to mark a range of structures in the early *Arabidopsis* embryo at high spatial resolution.

One of the most surprising discoveries made using these ACE tools was the early establishment of cell polarity. Albeit not endogenously expressed during early embryogenesis, within the first or second division of the apical cell, the central-plasma membrane-localized BOR1 and the peripheral plasma membrane-localized NIP5;1 proteins were localized in their corresponding face of the cell as observed in root endodermis, where BOR1 and NIP5:1 are endogenously expressed[24, 25]. This finding

suggested that the central/peripheral cell polarity, at least the machinery used by BOR1 and NIP5;1, is established as early as after the apical cell divides and physically separates outer from inner membranes. This raises a question about how such polarity is established with so little geometric information. The apical cell is nearly isodiametric and lacks physical contact with their surrounding except for the suspensor cell and the embryo surrounding region (ESA) of the endosperm. The only cell autonomous reference that could be uses as reference to distinguish center and periphery would be the original plasmamembrane derived from the apical cell. It is possible that this membrane is decorated by certain protein or lipid whose expression is restricted to the egg cell, zygote, or apical cell. Conversely, it could be that only the "new" plasma membrane is decorated by a factor expressed in the apical cell or its daughters. A scenario involving membrane "age" would suffice to distinguish inner from outer membrane in the 2-cell embryo, but would fail at later stages of embryogenesis when not all cell divisions are parallel to the outside-inside axis. Thus, additional mechanisms are likely necessary to specify or propagate polarity information. Strikingly, in addition to the observed early establishment of inside-outside cell polarity in the embryo, it was previously discovered that the first division of the apical cell is preferentially oriented relative to the seed axis[6]. The preferential division orientation of the apical cell indicates that the embryo can perceive its spatial information relative to the seed, suggesting communication between the embryo and the rest of the seed, likely the ESA. Therefore, another possible mechanism for central/peripheral polarity establishment in the early embryo could involve interactions between the endosperm and the embryo, with a signal from the endosperm serving as spatial reference for the embryo. This could instruct both embryo-seed relative position and center-periphery identification. In addition, the external signal can be blocked from the embryo proper as the embryo proper becomes symplastically and apoplastically isolated from the rest of seeds following the buildup of cuticle in the epidermal cells at early globular stage[26, 27]. At this developmental stage, at least epidermis and vascular/ground precursor cells are already established and communication between such cells can serve as reference for pattern and polarity in the embryo proper. Such interactions, for example involving movement of the SHR and TMO7 protein and the miR166 RNA have been reported[22, 28, 29], and a mutation that blocks plasmodesmatal transport induces defects in tissue patterning at the globular stage[30]. This scenario would ensure that the embryo proper reaches sufficient complexity to sustain its own spatial reference for cell polarity before shutting off external regulation. Communication between endosperm and embryo proper cells has been shown to play a crucial role in epidermis formation and regulates the expression of epidermis-specific genes in early embryos[31, 32]. In addition, while cell proliferation of the embryo is not affected by toxin-mediated ablation of the endosperm, abnormal cell division patterns in the embryo were reported[33]. It will be

interesting to further investigate the actual mechanism of polarity establishment and interpretation in embryos and its role in pattern formation during early embryogenesis, and the ACE tools developed here now enable such questions to be addressed.

Besides the early establishment of polarity, we also observed peculiarities of nuclear and vacuolar morphology in early embryos. These observations led to our assumption that the nuclei remain stationary during the cell cycle and the asymmetric cell divisions are achieved through precisely positioning the cell division plane independently of nuclear position. In several cell types, asymmetric cell divisions are preceded by nuclear migration towards the future cell division plane[34-36]. In other cases, mitosis and cytokinesis are restricted to an area followed by the asymmetric movement of the phragmoplast to achieve volume subdivision and orientation of cell division. In these cases, positioning of nuclei is more likely the result of prior cell division plane determination[37]. We found that in early embryos, where division orientation is actively controlled by an auxin-dependent mechanism[6], nuclei are themselves large, filling up most of the cell volume. In addition, potential nuclear movement is further restricted by their surrounding vacuoles. It is therefore unclear if and how the position of the nucleus may help select a variant orientation following Besson-Dumais' rule. These are proposed to rely on tense cytoplasmic strands radiated from the nuclei to the cell surface. However, when it comes to cytoskeleton organizations in early embryo, both microtubule and actin in embryo proper cells seemed unorganized compared to dividing cells in other tissues and even in protoplast and developed embryos[34, 38-49]. In the 8-cell stage, the isodiametric embryo makes each embryonic cell almost isometric in all three axes making it impossible to conduct quantitative analysis of network topology. This demonstrates the dire need for advanced microscopies, for example, lattice light-sheet microscopy[50], with isometric resolution in all axes and multiple angles for image acquisition to allow precise 3D reconstruction. The precise spatial information for microtubule and actin cytoskeletons is not only necessary to digitally segment cells and separate cortical microtubule array from microtubules and actin in cytoplasmic strands, but also necessary for quantitative analysis of the length, orientation, and anisotropy or each cytoskeletal structures in the future with new software.

Despise the lack of means for quantitative analysis of cytoskeletal organization in early embryos, in **Chapter 5**, we tested the contribution of cytoskeleton organization to auxin-controlled division orientation. We found that the structure of mitotic and cytokinetic microtubule assemblies seemed unaffected in embryos with suppressed auxin responses. However, significant differences were found in the anisotropy of global microtubule architecture, in the frequency of microtubule depolymerization upon embryo extraction, and in the presence of peri-nuclear actin arches. Rather than

using the *mp* mutant as a system for suppressed auxin response, a two-component system was used to suppress auxin responses in embryos through misexpressing auxin-insensitive Aux/IAA12, BODENLOS, driven by the *RPS5A* promoter[51]. The first fully penetrant morphological phenotype in *mp* mutant embryos is the altered cell division in hypophysis at early globular stage. Here, two types of division orientation can occur: radial and transverse anticlinal. In contrast, in *pRPS5A>>bdl* embryos, the first clear morphological phenotype is the cell division between 8- and 16-cell stage that is consistently shifted from the asymmetric periclinal division found in wild type embryos to symmetric radial anticlinal division[6]. Interestingly, the "abnormal" cell division pattern found in *pRPS5A>>bdl* embryos aligned precisely with the cell division pattern of isodiametric cell clusters follow solely Besson-Dumais' rule, and thus auxin responses would be the only necessary input in the early embryos to defy Besson-Dumais' rule[5]. Given the intact mitotic and cytokinetic microtubule machinery in the *pRPS5A>>bdl* embryos and combined with the stationary nuclei and how nuclei and vacuoles are tightly restrained in the embryo cells, auxin responses are likely regulating the oriented cell division via pre-mitotically determining the position of the cell division plane rather than acting on specific component of the mitotic and cytokinetic machineries. The altered microtubule and actin architectures found in *pRPS5A>>bdl* embryos then suggest that auxin responses might regulate the cell division orientation through altering the cytoskeleton. This could be affected by regulating stability, by connecting cytoskeleton elements to specific faces of the embryo cell, by favoring the number of cytoplasmic microtubules in the cytoplasmic strands connecting the nuclei to particular cell faces, or by controlling the density of cortical microtubules on particular faces. Interestingly, a recent study that compared transcriptomes of embryos at globular stage between wild type and *bdl* misexpression in lower vascular and ground tissue cells[12, 52] showed significant down-regulation of microtubule associated protein, IQDs[53], and a regulator of actin dynamic regulator, ROP-GEF[54, 55]. This suggests a plausible regulatory mechanism of cytoskeletal dynamics by auxin responses. In addition, preliminary work based on the same transcriptome study had identified several polar localized proteins in the embryo suggesting auxin responses may also be involved in polarity establishment or its connection to the cytoskeleton (Yoshida et al., submitted). Through deploying other embryo specific markers of cellular components of interest - for example polar localized proteins - described in **Chapter 4**, into the *pRPS5A>>bdl* background, one should be able to address remaining questions about the machineries and cellular processes regulated by auxin responses to determine cell division pattern.

Outlook

In this thesis, we described novel fluorescent protein-based reporters for auxin signaling and cellular structures, along with the demonstration of the potential of these toolkits to dissect developmental processes through the scope of cell biology. However, the exact mechanism of auxin responses underlying regulated oriented cell division remains elusive. With the toolkits and observation described in this thesis, a comprehensive survey of cellular organizations from apical cell to early globular embryo with various genetic background is now feasible and would provide a solid foundation to specify the specific machinery regulated by auxin responses at given developmental stages. In addition, another related and crucial question would be the mechanism of how auxin responses position the division plane to determine the volume ratio between the two daughter cells. Answering these two fundamental questions will further broaden our understanding about how the body is set and executed during embryogenesis.

References

1.   Errera, L. *Bot. Centralbl.* **34**, 395-398 (1888).
2.   Sachs, J. Über die Anordnung der Zellen in jüngsten Pflanzentheilen ! (Stahel'schen, 1877).
3.   Thompson, D.W. On growth and form. (Cambridge Univ. Press, 1942).
4.   Berthold, G. Studien über protoplasmamechanik. (A. Felix, 1886).
5.   Besson, S. & Dumais, J. *Proc Natl Acad Sci U S A* **108**, 6294-6299 (2011).
6.   Yoshida, S. et al. *Dev. Cell* **29**, 75-87 (2014).
7.   Ulmasov, T., Liu, Z.-B., Hagen, G. & Guilfoyle, T.J. *Plant Cell* **7**, 1611-1623 (1995).
8.   Boer, D.R. et al. *Cell* **156**, 577-589 (2014).
9.   Brunoud, G. et al. *Nature* **482**, 103-U132 (2012).
10.   Liao, C.Y. et al. *Nat. Methods* **12**, 207-210, 202 p following 210 (2015).
11.   Weijers, D. et al. *Development* **128**, 4289-4299 (2001).
12.   Moller, B.K. et al. *Proc Natl Acad Sci U S A* **114**, E2533-E2539 (2017).
13.   Figueiredo, D.D., Batista, R.A., Roszak, P.J., Hennig, L. & Kohler, C. *Elife* **5** (2016).
14.   Figueiredo, D.D., Batista, R.A., Roszak, P.J. & Kohler, C. *Nat Plants* **1**, 15184 (2015).
15.   Di Mambro, R. et al. *Proc Natl Acad Sci U S A* **114**, E7641-E7649 (2017).
16.   Bhatia, N. et al. *Curr. Biol.* **26**, 3202-3208 (2016).
17.   Rademacher, E.H. et al. *Plant J.* **68**, 597-606 (2011).
18.   Brady, S.M. et al. *Science* **318**, 801-806 (2007).
19.   Berleth, T. & Jurgens, G. *Development* **118**, 575-587 (1993).
20.   Hardtke, C.S. & Berleth, T. *EMBO J.* **17**, 1405-1411 (1998).
21.   Weijers, D. et al. *Dev. Cell* **10**, 265-270 (2006).
22.   Schlereth, A. et al. *Nature* **464**, 913-916 (2010).
23.   Guilfoyle, T.J. & Hagen, G. *Curr. Opin. Plant Biol.* **10**, 453-460 (2007).
24.   Takano, J. et al. *Nature* **420**, 337-340 (2002).
25.   Takano, J. et al. *Plant Cell* **18**, 1498-1509 (2006).
26.   Stadler, R., Lauterbach, C. & Sauer, N. *Plant Physiol.* **139**, 701-712 (2005).
27.   Szczuka, E. & Szczuka, A. in Acta Biologica Cracoviensia Series Botanica 63-67 (2003).
28.   Cui, H. et al. *Science* **316**, 421-425 (2007).
29.   Carlsbecker, A. et al. *Nature* **465**, 316-321 (2010).
30.   Möller, B.K. (2012).
31.   Tanaka, H. et al. *Development* **134**, 1643-1652 (2007).
32.   Tanaka, H. et al. *Development* **128**, 4681-4689 (2001).
33.   Weijers, D., Van Hamburg, J.P., Van Rijn, E., Hooykaas, P.J. & Offringa, R. *Plant Physiol.* **133**, 1882-1892 (2003).
34.   Kimata, Y. et al. *Proc Natl Acad Sci U S A* **113**, 14157-14162 (2016).
35.   Chytilova, E. et al. *Molecular Biology of the Cell* **11**, 2733-2741 (2000).
36.   Panteris, E., Apostolakos, P. & Galatis, B. *Cell Motility* **63**, 696-709 (2006).
37.   Cutler, S.R. & Ehrhardt, D.W. *Proc Natl Acad Sci U S A* **99**, 2812-2817 (2002).

38. Wang, Q. & Huang, S. *Mol Plant* **7**, 1397-1401 (2014).
39. Ueda, K., Matsuyama, T. & Hashimoto, T. *Protoplasma* **206**, 201-206 (1998).
40. Lucas, J.R., Nadeau, J.A. & Sack, F.D. *J. Exp. Bot.* **57**, 71-79 (2006).
41. Lucas, J.R. & Shaw, S.L. *Plant J.* **71**, 454-463 (2012).
42. Louveaux, M., Julien, J.D., Mirabet, V., Boudaoud, A. & Hamant, O. *Proc Natl Acad Sci U S A* **113**, E4294-4303 (2016).
43. Dyachok, J., Sparks, J.A., Liao, F., Wang, Y.S. & Blancaflor, E.B. *Cytoskeleton (Hoboken)* **71**, 311-327 (2014).
44. Collings, D.A. & Wasteneys, G.O. *Canadian Journal of Botany-Revue Canadienne De Botanique* **83**, 579-590 (2005).
45. Era, A. et al. *Plant Cell Physiol.* **50**, 1041-1048 (2009).
46. Sheahan, M.B., Staiger, C.J., Rose, R.J. & McCurdy, D.W. *Plant Physiol.* **136**, 3968-3978 (2004).
47. Voigt, B. et al. *Eur. J. Cell Biol.* **84**, 595-608 (2005).
48. Wang, Y.S., Motes, C.M., Mohamalawari, D.R. & Blancaflor, E.B. *Cell Motil. Cytoskeleton* **59**, 79-93 (2004).
49. Shi, L. et al. *Biochem. Biophys. Res. Commun.* **405**, 632-637 (2011).
50. Chen, B.C. et al. *Science* **346**, 1257998 (2014).
51. Rademacher, E.H. et al. *Dev. Cell* **22**, 211-222 (2012).
52. Palovaara, J. et al. *Nat Plants* **3**, 894-904 (2017).
53. Bürstenbinder, K. et al. *Plant Physiol.* **173**, 1692-1708 (2017).
54. Berken, A., Thomas, C. & Wittinghofer, A. *Nature* **436**, 1176 (2005).
55. Craddock, C., Lavagi, I. & Yang, Z. *Trends Cell Biol.* **22**, 492-501 (2012).

Summary

A fundamental question in developmental biology is how the complex cellular pattern in multicellular organisms arises from a single cell. In land plants, the biosynthesis, transport, and signaling of phytohormone auxin is essential for pattern formation in embryogenesis. In Chapter 1, a brief introduction on plant embryogenesis, the roles of auxin signaling in pattern formation in early embryo, cellular basis on oriented cell division, and auxin-regulated oriented cell division during early embryogenesis are described as the foundation of this thesis aimed to answer the domain and cellular structures regulated by auxin that lead precise pattern formation during early embryo development of *Arabidopsis thaliana*.

In Chapter 2, two novel fluorescent protein-based reporters for auxin perception and response, respectively, were developed to overcome technical bottlenecks for dissecting auxin signaling in embryos. The novel reporters offer higher sensitivity and responsiveness compared to existing tools. Our reporters revealed the gradients and maxima of auxin perception and response that had been hypothesized, but not yet detected. In addition, these new tools now offer a wider scope of application beyond the embryo and are generic tools for the auxin biology research community.

In Chapter 3, the auxin reporters described in the previous chapter were improved to overcome their limitations, and the first comprehensive auxin reporter that was able to simultaneously visualize both auxin perception and response was characterized. With this new auxin reporter, the differential auxin signaling capacity between different cell types and differentiation states was demonstrated. In addition, the reporter for auxin response described in the previous chapter was applied in mutant embryos with a local auxin response defect, revealing its broad impact on auxin output.

In Chapter 4, a toolkit of fluorescent protein-based markers labeling specific cellular structures was established. The structures included the plasma membrane, cytoskeletons, organelles, and the nucleus, structures excepted to participate in the oriented cell divisions that shape the early embryo. Expression of the protein markers was optimized for early Arabidopsis embryos, and topologies of subcellular structures were mapped during cellular reorganization in early embryogenesis. In addition, a specialized imaging technique was developed to allow high-resolution 3-dimensional imaging within the special embryo geometry. Combining the embryo-specific cellular structure marker set and the optimized imaging approach, 3-dimentional imaging of cellular structures in early embryos was achieved, and the dynamic organizations of organelles and cytoskeletons along with the unexpected discovery of early establishment of central/peripheral polarity in early embryos are described in this chapter.

In Chapter 5, part of the toolkit established in the previous chapter was applied to embryos with inducible suppression on auxin response. Previously, it was shown that suppression of auxin response leads to divisions that follow only the cellular geometry, while auxin response allows cells to divide asymmetrically by deviating from this mode. It was unclear if and how the cytoskeleton mediates this auxin output, which was tested by visualizing the effect of auxin response on cytoskeleton organization. Distinct effects on both actin and microtubule properties were identified, and this provides an indication for further investigation into the biochemical and biomechanical mechanisms of pattern formation.

In Chapter 6, the discoveries described in this thesis are placed in a broader context and discussed along with the latest technological and scientific advances related to the topic to offer future perspective in understanding the mechanisms underlying pattern formation.

Acknowledgements

Six-year of PhD research is quite an experience, a combination of anxiety, fun, agony, joy, boredom, excitement, failure, and success. While I did spend considerable amount of time alone in the rather dark basement during the project, I was not alone in my journey of my PhD years and had received a great deal of support from my supervisor and colleagues. Hereby, I would like to express my grateful thank to them.

Prof. D. Weijers. This thesis and my scientific career could only exist with Dolf's support. The opportunity to conduct my minor master thesis project in his group in 2009 brought me to the field of plant development and auxin biology. After hearing my ill-fated first attempt at conducting a PhD research in Germany, he offered me a second chance leading to the work described in this thesis. Throughout my six-year PhD research, he has supported me with all the freedom, encouragement, and tolerance toward my (hopefully only occasional) tardiness and stubbornness I can ever ask for. More importantly, he has showed me an exemplar of being a respectable scientist and a leader of a research group.

Prof. S. de Vries. As a developing scientist myself who knew little about embryogenesis and signal transduction in other species/systems, Sacco introduced me somatic embryogenesis and the roles of plasmamembrane/extracellular proteins along with all his "pre-Internet/digital era" knowledge. The inspirations he gave me put my thought into different perspectives when addressing the questions asked in this thesis that helped me tremendously to conceptualize my findings.

Dr. C. Albrecht, Dr. JW. Borst, Dr. B. De Rybel, Dr. T. Radoeva and Mr. W. van den Berg. While the ability to attack questions through multiple angles and conceptualization are important for any scientist, technical competence is as essential for an experimental scientist. Cathy and Willy are my wet-lab go-to people who have kindly shared their broad knowledge and experience with me whenever I got a problem and taught me a great deal of laboratory techniques. When it came to experiment design and data analysis, I always went to Bert and Tanya who patiently discussed the experiment details with me and helped me a lot to avoid common pitfalls. Jan Willem with his in-depth knowledge in confocal microscopy helped me immensely to improve the methodology for imaging and signal quantification used in this thesis.

Ms. L. van Egmond. While conducting a PhD research is a mind-challenging activity, it would have been a mind-exhausting one without Laura's help in the administration, from my resident permits to the notorious time-sheets.

My fellow colleagues in the laboratory of Biochemistry, especially Maritza, Thijs, Wouter, Diaa, Jos, Joseline, Mieke, Gudrun, and Tom. It is a good fortunate to have the opportunity to work and be friends with them. It is the great time we shared together that made my six-year PhD research not only a journey of scientific exploration, but also a fond memory I will always cherish.

About the Author

Che-Yang Liao, born in Taipei, Taiwan, on April 11th, 1982. He completed his secondary education in Affiliated Senior High School of National Taiwan Normal University in 1999 and entered National Taiwan University majoring Horticultural Science. In 2005 after graduating from the university with a degree of Bachelor of Science, instead of accepting an offer of a master program, he entered the Army for his military service serving as a Private in the armored cavalry battalion deployed in Penghu Island. In 2007, after fulfilling his duty, he went to the Netherlands to pursue a Master degree in Wageningen University and Research. He received a degree of Master of Science in Plant Biotechnology in 2010 and relocated to Freiburg im Breisgau, Germany, working as a scientific employee for Prof. Thomas Laux in the Laboratory of Developmental Biology and Biotechnology of Plants for the next two and a half years. In September 2012, he returned to Wageningen and began his PhD research under the supervision of Prof. Dolf Weijers in the Laboratory of Biochemistry. The results obtained over the following six years are presented in this thesis.

Publications

Technical advance

- **Liao, C.Y.**, and Weijers, D. (2018). *Analyzing sub-cellular reorganization during early Arabidopsis embryogenesis using fluorescent markers.* (in Press)
- **Liao, C.Y.**, and Weijers, D. (2018). *A toolkit for studying cellular reorganization during early embryogenesis in Arabidopsis thaliana.* Plant J 93, 963-976. (Selected as cover and research highlight of given issue)
- **Liao, C.Y.**, Smet, W., Brunoud, G., Yoshida, S., Vernoux, T., and Weijers, D. (2015). *Reporters for sensitive and quantitative measurement of auxin response.* Nat Methods 12, 207-210, 202 p following 210.
- Wendrich, J.R., **Liao, C.Y.**, Van Den Berg, W.A.M., De Rybel, B., and Weijers, D. (2015). *Ligation-independent cloning for plant research.* In Methods in Molecular Biology (Humana Press Inc.), pp. 421-431.
- De Rybel, B., van den Berg, W., Lokerse, A., **Liao, C.Y.**, van Mourik, H., Moller, B., Peris, C.L., and Weijers, D. (2011). *A versatile set of ligation-independent cloning vectors for functional studies in plants.* Plant Physiol 156, 1292-1299.

Review

- van Dop, M., **Liao, C.Y.**, and Weijers, D. (2015). *Control of oriented cell division in the Arabidopsis embryo.* Curr Opin Plant Biol 23, 25-30.

Collaboration

- Chakrabortty, B., Willemsen, V., de Zeeuw, T., **Liao, C.Y.**, Weijers, D., Mulder, B., and Scheres, B. (2018). *A Plausible Microtubule-Based Mechanism for Cell Division Orientation in Plant Embryogenesis.* Curr Biol 28, 3031-3043 e3032.
- Roychoudhry, S., Kieffer, M., Del Bianco, M., **Liao, C.Y.**, Weijers, D., and Kepinski, S. (2017). *The developmental and environmental regulation of gravitropic setpoint angle in Arabidopsis and bean.* Sci Rep 7, 42664.

Education Statement of the Graduate School

Experimental Plant Sciences

Issued to: Che-Yang Liao

Date: 17 December 2018

Group: Laboratory of Biochemistry

University: Wageningen University & Research

The Graduate School
EXPERIMENTAL PLANT SCIENCES

1) Start-Up Phase	*date*	*cp*
► **First presentation of your project**		
Cellular basis of pattern formation	18 Apr 2013	1.5
► **Writing or rewriting a project proposal**		
► **Writing a review or book chapter**		
Analyzing sub-cellular reorganization during early Arabidopsis embryogenesis using fluorescent markers', accepted for publication in book series Methods in Molecular Biology, edition Plant Embryogenesis	Nov 2018	6.0
► **MSc courses**		
► **Laboratory use of isotopes**		
Subtotal Start-Up Phase		7.5

2) Scientific Exposure	*date*	*cp*
► **EPS PhD student days**		
EPS PhD student day, University of Amsterdam, the Netherlands	30 Nov 2012	0.3
EPS PhD student day, Leiden University, the Netherlands	29 Nov 2013	0.3
EPS PhD student days, Get2Gether, Soest, the Netherlands	28-29 Jan 2016	0.6
► **EPS theme symposia**		
EPS theme 1 'Developmental Biology of Plants', Leiden University, the Netherlands	17 Jan 2013	0.3
EPS theme 1 'Developmental Biology of Plants', Leiden University, the Netherlands	08 Jan 2015	0.3
EPS theme 1 'Developmental Biology of Plants', Wageningen University, the Netherlands	21 Jan 2016	0.3
► **National meetings (e.g. Lunteren days) and other National Platforms**		
Annual Meeting 'Experimental Plant Sciences', Lunteren, the Netherlands	22-23 Apr 2013	0.6
Annual Meeting 'Experimental Plant Sciences', Lunteren, the Netherlands	14-15 Apr 2014	0.6
Annual Meeting 'Experimental Plant Sciences', Lunteren, the Netherlands	13-14 Apr 2015	0.6
Annual Meeting 'Experimental Plant Sciences', Lunteren, the Netherlands	11-12 Apr 2016	0.6
► **Seminars (series), workshops and symposia**		
Thursday Seminars Biochemistry: Prof. David Robinson (Heidelberg University, Germany)	27 Sep 2012	0.1
Thursday Seminars Biochemistry: Dr M.G. Smits (Hospital Gelderse Valley, Ede, The Netherlands)	28 Mar 2013	0.1
Thursday Seminars Biochemistry: Dr. Marcus Grebe (Umeá Plant Science Center, Sweden)	29 May 2013	0.1
Thursday Seminars Biochemistry: Dr. Pierre Hilson (IJPB Versailles, France)	13 Nov 2013	0.1
Thursday Seminars Biochemistry: Dr. Marcus Heisler (EMBL, Heidelberg, Germany)	28 Nov 2013	0.1
Thursday Seminars Biochemistry: Dr. Daniël Van Damme (VIB, Ghent, Belgium)	30 Jan 2014	0.1
Thursday Seminars Biochemistry: Dr. Ivonne Stahl (Heinrich Heine University, Düsseldorf, Germany)	11 Mar 2014	0.1
Thursday Seminars Biochemistry: Dr. Goerge Bassel (University of Birmingham, United Kingdom)	24 Apr 2014	0.1
Thursday Seminars Biochemistry: Prof. Cyril Zipfel (Sainsbury Laboratory, United Kingdom)	04 Jun 2014	0.1
Thursday Seminars Biochemistry: Dr. Saijaliisa Kangasjärvi (University of Turku, Finland)	28 May 2015	0.1
Thursday Seminars Biochemistry: Dr. Martin Jinek (University of Zürich, Switzerland)	06 Jun 2015	0.1
Thursday Seminars Biochemistry: Dr. François Parcy (IRTSV, Grenoble, France)	15 Oct 2015	0.1
Thursday Seminars Biochemistry: Dr. Julia Santiago (University of Geneva, Switzerland)	12 Nov 2015	0.1
Joint Meeting groups prof. Dolf Weijers and prof. Ben Scheres, Wageningen, the Netherlands	22 Jan 2015	0.3
Joint Meeting groups prof. Dolf Weijers and prof. Ben Scheres, Wageningen, the Netherlands	25 Sep 2015	0.3

► **Seminar plus**		
► **International symposia and congresses**		
Embryo meeting 2013, Haigerloch, Germany	06-08 May 2013	0.9
Embryo meeting 2016, Haigerloch, Germany	09-11 May 2016	0.9
EMBO conference Series- Interdisciplinary plant development, Cambridge, UK	21-24 Sep 2014	0.9
Auxin: Get together, Brno, Czech Republic	11-12 Nov 2016	0.6
► **Presentations**		
Poster: EMBO conference Series- Interdisciplinary plant development, Cambridge, UK	21-24 Sep 2014	1.0
Oral presentation: Embryo meeting 2016, Haigerloch, Germany	09-11 May 2016	1.0
Oral presentation: EPS theme 1 'Developmental Biology of Plants', Leiden University	08 Jan 2015	1.0
Oral presentation: Auxin: Get together, Brno, Czech Republic	21-24 Sep 2016	1.0
► **IAB interview**		
► **Excursions**		
Excursion to Enza Zaden	12 Jun 2015	0.2
Scientific PhD Excursion group prof. Sacco de Vries, United Kingdom	21-28 Sep 2013	1.5
Subtotal Scientific Exposure		15.4

3) In-Depth Studies	*date*	*cp*
► **EPS courses or other PhD courses**		
International PhD school Plant Development, Zellingen-Retzbach, Germany	25-27 Sep 2013	0.9
International PhD school Plant Development, Zellingen-Retzbach, Germany	07-09 Oct 2015	0.9
EPS PhD course: Transcription Factors and Transcription Regulation	12-14 Dec 2016	1.0
► **Journal club**		
Participation in weekly journal club (Dolf Weijers Group)	Sep 2012-Sep 2016	3.0
► **Individual research training**		
Subtotal In-Depth Studies		5.8

4) Personal Development	*date*	*cp*
► **Skill training courses**		
Competence Assessment	Mar-May 2014	0.3
Techniques for Writing and Presenting a Scientific Paper	07-11 Apr 2014	1.2
Career assessment	22 Apr 2016	0.3
Social Dutch for employees, level A0 to A1	Oct 2013 - Jan 2014	3.0
► **Organisation of PhD students day, course or conference**		
► **Membership of Board, Committee or PhD council**		
Subtotal Personal Development		4.8

TOTAL NUMBER OF CREDIT POINTS*	**33.5**
Herewith the Graduate School declares that the PhD candidate has complied with the educational requirements set by the Educational Committee of EPS which comprises of a minimum total of 30 ECTS credits. ** A credit represents a normative study load of 28 hours of study.*	

PROPOSITIONS

1. Discrepancies in auxin perception and response patterns, as revealed by combinatorial imaging tools, highlight intrinsic differences in response capacity between cells, which need to be considered when visualizing auxin activity.

    (this thesis)

2. Radial organismal polarity is established at the earliest possible moment during *Arabidopsis thaliana* embryogenesis.

    (this thesis)

3. With rapid advances in microscopy, computer vision becomes the next limiting step in cellular life sciences.

4. Considering the complexity of living organisms, biologists need to be a polymath rather than a specialist.

5. In scientific research, communication skills are more important than laboratory techniques.

6. Inspiration, creativity and challenge are key drivers of advances in human civilization and require more emphasis in teaching and training curricula.

Propositions belonging to the thesis, entitled
"Cellular reorganization in auxin-dependent pattern formation during early embryogenesis in *Arabidopsis thaliana*"

Che-Yang Liao
Wageningen, 17 December 2018